Spring 2022

Analyzing Compton Telescope (COMPTEL) Measurements of the Atmospheric Albedo Neutron Flux Using Neutron Capture

Zain Abbas
University of New Hampshire, Durham

Analyzing Compton Telescope (COMPTEL) Measurements of the Atmospheric Albedo Neutron Flux using Neutron Capture

BY

Zain Abbas

MS, University of New Hampshire, 2021

THESIS

Submitted to the University of New Hampshire

in Partial Fulfillment of

the Requirements for the Degree of

Master of Science*

in

Physics

December, 2021

This thesis/dissertation has been examined and approved in partial fulfillment of the requirements for the degree of Master in Science in Physics by:

Thesis Director, Mark McConnell, Professor (Space Science)

Mark McConnell, Professor (Space Science)

James Ryan, Professor (Space Science)

Harald Kucharek, Professor (Space Science)

On September 2021

Original approval signatures are on file with the University of New Hampshire Graduate School.

DEDICATION

I dedicate my thesis to my beloved parents (Abbas Raza, Syeda Farhana Abbas) and family who supported me throughout this process. They encouraged me to pursue higher education in physics and explore new ways to learn a topic of interest. They advised me to develop a sense of perseverance in accomplishing my goals. Without their support, it would be a very challenging journey to endeavor. Also, I dedicate this thesis to my late grandparents (Suraya Begum, Anwar Hussain Trmizi, and Muhammad Hussain Rizvi) who always encouraged me to seek knowledge in a truthful manner and never take a shortcut path to success.

ACKNOWLEDGEMENTS

I am very grateful to my research advisor Prof. Mark McConnell for allowing me to research one of the interesting space science topics called atmospheric albedo neutrons. Investing the time and effort in this great scientific project expanded my knowledge of the albedo neutrons and the inner Van Allen radiation belts. In addition, it expanded my abilities in scientific programming and data analysis skills. Prof. Mark assisted me throughout the project specifically in writing the thesis. He made sure that I understand each aspect of this thesis and encouraged me to explore different methods in conducting the research. I am also grateful to committee members (Prof. James Ryan, Prof. Harald Kucharek) as well who approved my thesis.

PREFACE

With a passionate interest in space science, I always wanted to conduct research on high-energy astrophysics. This leads me to research one of the NASA missions called COMPTEL that uses a gamma-ray imaging telescope to survey the sky in gamma-ray energy. One of the goals of this mission was to analyze atmospheric albedo neutron flux as a function of geomagnetic rigidity and various geophysical parameters. These albedo neutrons undergo the CRAND process and contribute to the Van Allen radiation belts. These radiation belts pose a great threat to astronauts and spacecraft in space. As a graduate research assistant, I was primarily responsible to analyze the entire mission data and make reasonable analyses on the albedo neutron flux. Our results confirm the previous balloon experiments and theoretical models. Using the COMPTEL data we enhanced our understanding of the sources of the inner proton radiation belts confirmed previous models.

TABLE OF CONTENTS

LIST OF TABLES

LIST OF FIGURES

LIST OF SYMBOLS

q — Electric Charge (C)

B — Magnetic Field (T)

θ — Measured zenith angle (°)

$\overline{\phi}$ — phi bar angle (°)

M — Magnetic Dipole Moment (T)

Rc — Cutoff rigidity (GV)

r — Radial distance (m)

n — Number density per energy (n)

γ — Lorentz factor

tn — Neutron decay lifetime (s)

σ — Standard deviation

μ — Mean

En — Neutron energy (MeV)

η — Neutron flux ($MeV/cm^2/s$)

ABSTRACT

Analyzing Compton Telescope (COMPTEL) Measurements of the Atmospheric Albedo Neutron Flux using Neutron Capture.

by

Zain Abbas

University of New Hampshire, September, 2021

All orbiting spacecraft are susceptible to space radiation that can cause permanent damage to spacecraft electronics. The atmospheric neutron flux is one of the potential candidates that give rise to space radiation. To extend the atmospheric neutron study as a function of various geophysical and observational parameters (like magnetic rigidity, altitude, and phase of the solar cycle), the NASA COMPTEL (Compton Telescope) instrument on-board the CGRO (Compton Gamma Ray Observatory) spacecraft had been used to measure the spatial and temporal variation of neutrons. We used gamma-ray telescopic mode to measure the instrumental 2.2 MeV line that arose from the thermal neutron being captured by a proton in the D1 module. Hence, the 2.2 MeV line served as a surrogate for the albedo neutron flux. To support the CRAND (Cosmic Ray Albedo Neutron Decay) theory, systematic measurements of the 2.2 MeV line rate were done as a function of various parameters primarily geomagnetic rigidity ranging from 4-18 GV, geocentric elevation 0^o-180^o, and spacecraft altitude ranging from 325-525 km. Using the Morris et al. neutron fit function, the estimated line rate was calibrated to obtain measured neutron flux. To evaluate our findings,

the measured neutron flux data was compared with Claret et al. simulated neutron data at solar minimum and solar maximum and also. Our neutron measurements follow the same trend as the simulated data.

CHAPTER 1

Introduction

The GCR (Galactic Cosmic Rays) are highly energetic particles that originate from various astrophysical events like supernova. They are primarily composed of hydrogen nuclei (approx. 89%) that, upon entering the Solar system, are modulated by the Sun's activity. When these ionized particles enter within the Earth's vicinity they are influenced by the Earth's magnetic field. Some of these particles interact with atmospheric constituents (like oxygen and nitrogen atoms) and produce large showers of secondary particles. Among all particle species, albedo neutrons have a great importance in space weather studies as they impact the inner Van Allen radiation belts and space instruments. Albedo neutrons that undergo CRAND (Cosmic Ray Albedo Neutron Decay) process populates the Van Allen radiation belts primarily inner proton radiation belt. The radiation belts create a hazardous space environment for astronauts and spacecrafts. Due to their penetrating nature, neutrons can easily penetrate and disrupt spacecraft electronics that could cause SEE (Single Event Effects) like bit error and latch up. To understand these dynamic properties of neutrons, scientists have launched various balloon experiments to measure albedo neutrons as a function of geophysical parameters. Over the years scientists' have postulated that CRAND is a key process that is responsible for populating high energy protons in the inner radiation belt. To test the CRAND model, Kanbach et al. (1974) presented the results of two balloon experiments that measured the energy and angular distribution of albedo neutrons between 70 and 250 MeV. The measured energy spectrum aligned with the Monte Carlo simulations on atmospheric neutrons, conforming the CRAND theory as the source of inner proton radi-

ation belt. Later, Preszler et al. (1976) launched a similar balloon experiment that measured albedo neutrons ranging from 10-100 MeV. However, the experiment provided limited neutron flux data at only one geomagnetic latitude value 41oand altitude. To better understand the albedo neutron flux, measurements covering wide range of rigidities and locations are needed. The COMPTEL instrument on-board CGRO spacecraft gives us an opportunity to measure the albedo neutron flux over a wide range of magnetic rigidity (4-18 GV) and altitude (350-525 km). The focus of this thesis is to study the variations in the albedo neutron flux using the COMPTEL gamma-ray data. The instrumental 2.2 MeV line arising from thermal neutron capture on hydrogen was used as a surrogate to measure the neutron flux as a function of geophysical and observational parameters primarily altitude, geomagnetic rigidity, and time. To evaluate our findings, we compare our neutron flux data with published models. We find out that albedo neutron flux exponentially decreases as a function of rigidity. In addition, we obtained a higher neutron flux at solar minimum and low neutron flux at solar maximum. All these findings conform previous balloon experiment results (see Kanbach, and Preszler) and Claret et al. (2014) simulation of atmospheric neutrons as a function of solar modulation.

CHAPTER 2

Science Overview

2.1 Magnetospheric and Atmospheric Physics

The Earth's magnetosphere is a volume of space formed by the Earth's magnetic field in response to the flow of plasma from the solar wind. When charged particles get trapped by the Earth's magnetic field, they create inner, and outer radiation belts around the Earth called Van Allen radiation belts (See figure 3.1). These belts were first discovered by the Explorer I spacecraft in January 1958. The Explorer I data showed that inner radiation belt was mainly saturated by protons, whereas the outer radiation was mainly populated by electrons. These observations gave rise to theoretical models of the radiation belts, explaining the charged particle source and loss mechanism. From early experiments, CRAND was considered the primary source of protons for inner radiation belt, radial diffusion for outer radiation belts and pitch angle scattering as a loss mechanism. To fully understand the dynamics of these radiation belts, NASA launched two Van Allen probes on August 2012 that successfully measured the variation in the intensity of both radiation belts. The probes were set at an orbital altitude of approximately 600 to 33,000 km with an inclination of 10^0. The two probes together provided in-situ measurements of the charged particles (eV-GeV) during maximum and minimum phase of the solar cycle. The major objectives of the mission were to determine the processes that accelerate and transport the charged particles in the radiation belts, and to understand the radiation belts in context of geomagnetic storms. [14]

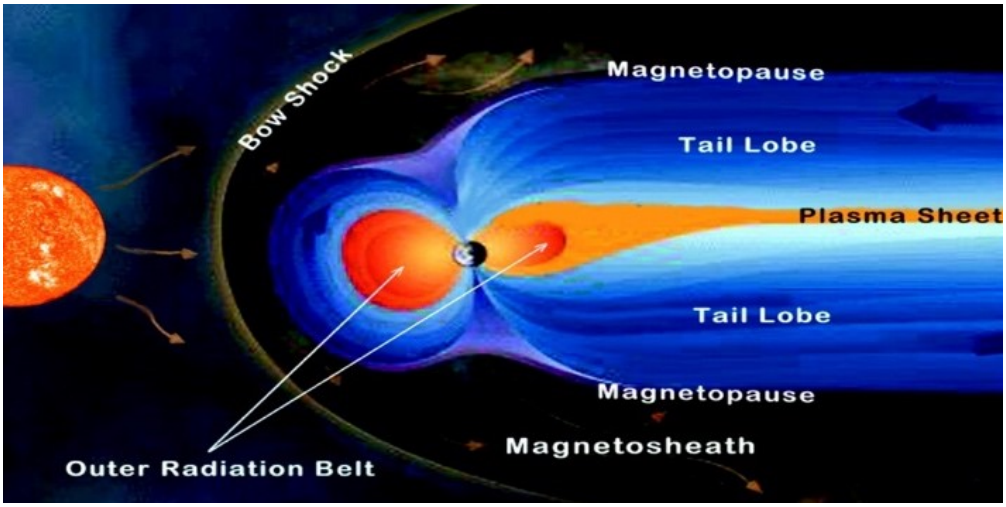

Figure 2.1: The above figure shows the Earths magnetosphere in response to solar plasma. The magnetosheath is a region between bow shock and magnetopause. The magnetotail is a region where the Earth's magnetic field combines to form a tail. This magnetic re-connection allows charged particle to travel to Earth's ionosphere and ionize the Earth's atmospheric particles [2]

In a research paper, Li et al. (2019) discussed recent advances in understanding the physical processes of the Van Allen radiation belts primarily: particle acceleration, transport and loss mechanisms of charged particles in the Earth's Van Allen radiation belts. These findings could enhance our existing knowledge of radiation belts and provide us insights into understanding particle dynamics on other planets.

2.1.1 Radial transport

During solar storms the trapped electron in the outer radiation belt show an increase intensity. The electrons are radially transported to outer radiation belts. Radial transport is mainly induced by the collision of electron drift motion with the electric and magnetic field fluctuations in ULF (Ultra Low Frequency). In addition, the fluctuating nature of electric and magnetic fields can generate plasma waves that during solar maximum could accelerate particles to relativistic speeds. This concept is known as "local heating". Together the radial transport diffusion and local heating could produce MeV electrons in the outer radiation belts with dependence of solar wind conditions.

2.1.2 EMIC waves

The EMIC (Electromagnetic Ion Cyclotron) waves is a type of plasma waves observed in the Earths magnetosphere. These waves primarily composed of H^+ and He^+ ions that generate in the equatorial region and propagate along the magnetic field lines near the ionosphere. These waves play an essential role in the loss process of outer radiation belt electrons. The probes data also showed that one of the plasma waves known as "hiss" waves was responsible to the loss of electrons from the radiation belts. Figure 2.2 shows various types of plasma waves in the Earth's magnetosphere.

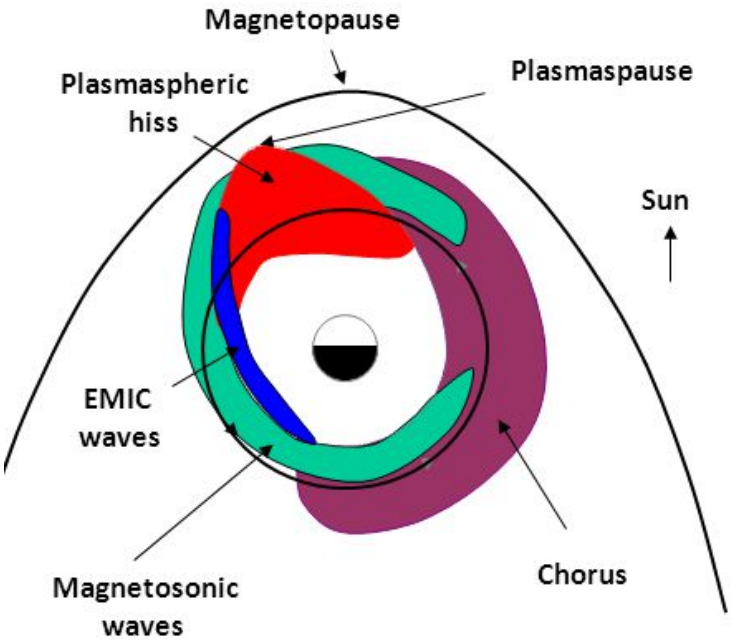

Figure 2.2: The above figure shows various types of plasma waves.The plasma waves are responsible for acceleration and loss of electrons to the upper atmosphere. [3]

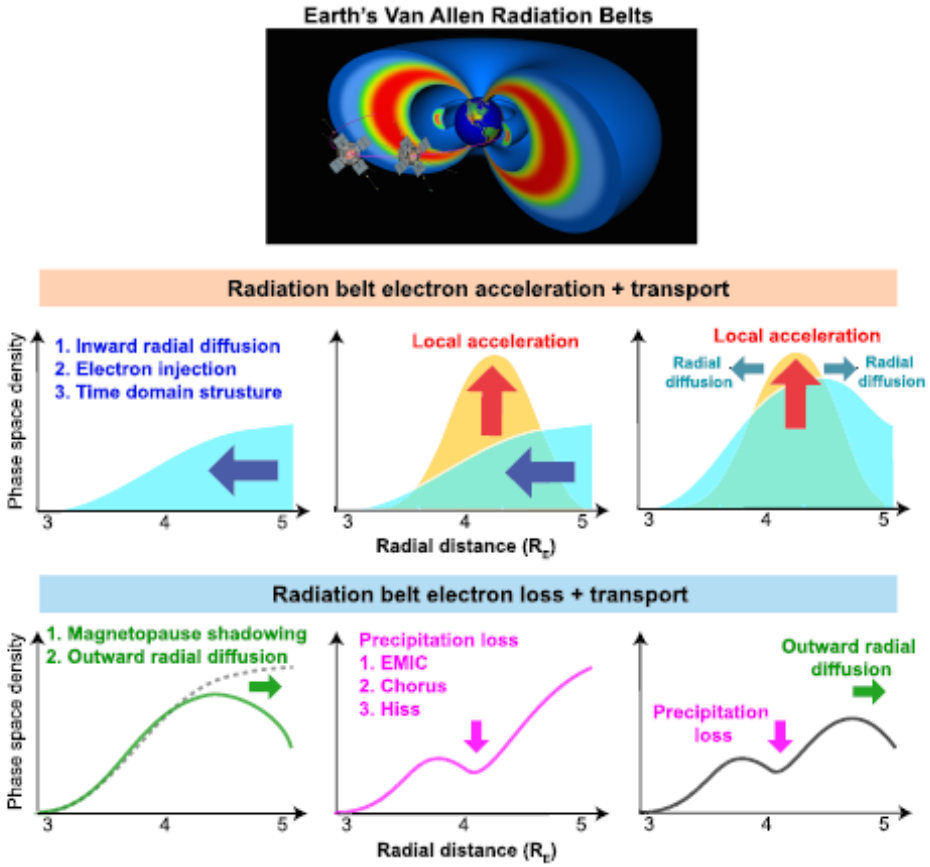

Figure 2.3: The above schematic summarizes the physical processes of outer radiation belt electrons. The middle figure shows the physical processes leading to radiation belt electron acceleration and transport. The bottom figure shows mechanisms that drive radiation belt electron loss and transport. [3]

The above figure summarizes physical processes responsible for controlling the Earth's outer electron radiation belts. The first three plots in the middle show electron acceleration and transport mechanisms in outer radiation belt. The upper left diagram shows that electron injections, inward radial diffusion, and time domain structures all three mechanisms play an essential role in providing seed electron populations (100 keV). The electron population could be accelerated through local acceleration. The second plot shows a gaussian peak due to local acceleration. Observations showed that the most efficient local heating is whistler mode chorus waves that mainly leads to gaussian radial peaks in electron phase space density. Lastly, radial diffusion due to ULF (Ultra-Low Frequency) waves play an essential role in redistributing electrons and accelerating them radially inward.

In addition, the physical mechanisms responsible for electron loss are outward radial diffusion, and precipitation loss. During solar maximum, an increase in solar wind pressure compresses the magnetopause closer to the Earth. As a result, the trapped outer belt electrons are lost to the magnetopause creating a negative electron phase space density. The outward diffusion by ULF further reduces the radiation belt electrons by transporting them from lower to higher radial distance. As mentioned earlier, the local precipitation loss due to various magnetospheric waves (EMIC waves, chorus waves, hiss etc) play an important role in transporting trapped radiation belts electron into the upper atmosphere. Together, the outward diffusion and precipitation loss can attenuate the trapped electrons in the outer radiation belt and create multiple peaks in electron phase space density. These observations from Van Allen probes increased our understanding of the physical processes (e.g radial transport, plasma waves, local heating etc) that play a vital role in fluctuating the charged particle fluxes in magnetosphere.

2.1.3 Observation of the inner radiation belt: CRAND and trapper solar protons

Studies have also shown that one of the dominant sources of charged particles in the inner radiation belts is the decay of atmospheric neutrons. These albedo neutrons are formed in response to the interaction of Galactic Cosmic Rays (GCR) with the Earth's atmosphere. The flux of GCRs reaching the atmosphere is influenced both by the (time-dependent) solar modulation and the Earth's magnetic field. Cosmic ray particles with high enough energy interact the Earth's atmosphere and generate large shower of secondary particles (like neutrons, muons, and pions), some of which eventually scatter into space. The upward moving albedo neutrons undergo beta decay with a mean lifetime of 881s, emitting protons and electrons that can become trapped in the inner radiation belt and create a hazardous environment for spacecraft in orbit [7] (See figure 2.4).

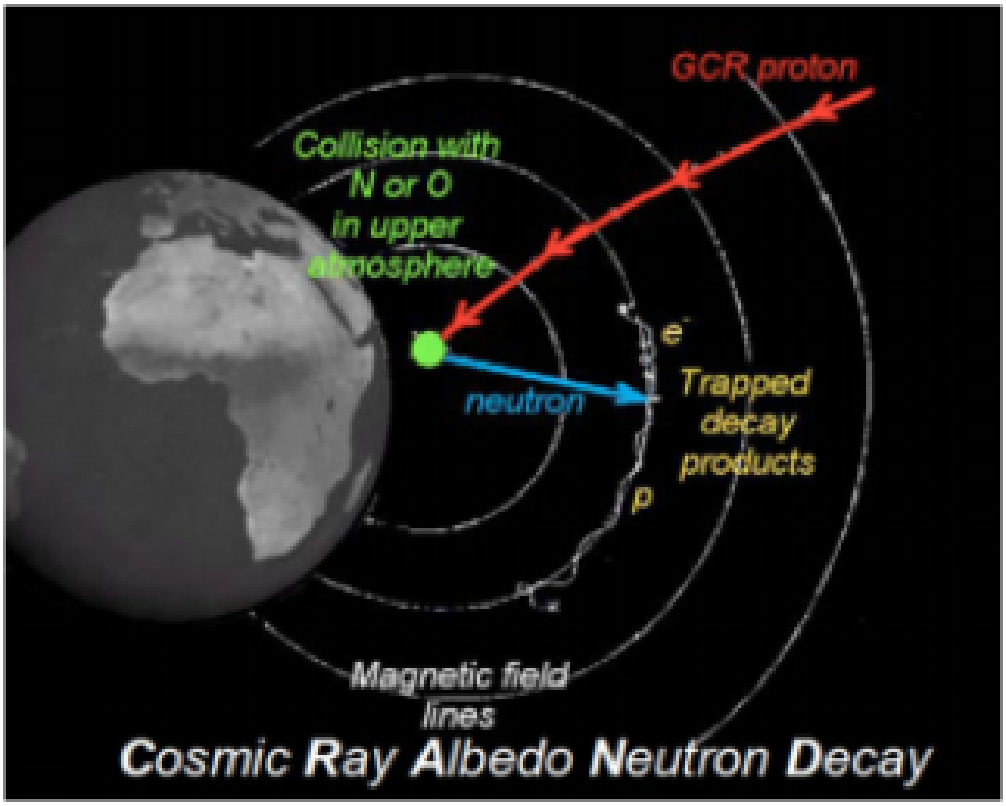

Figure 2.4: The GCR interacting with the Earth's atmosphere and giving rise to albedo neutrons. Furthermore, the neutrons decay into protons and electrons and get trapped by the Earth's magnetic field. [4]

In a scientific paper, Selesnick et al. (2014) presented the flux of inner proton radiation belt using the Van Allen probes REPT (Relativistic-Electron-Proton Telescope). The probes measured the protons as a function of kinetic energy (24 to 76 MeV), equatorial pitch angle, and magnetic L shell from October 2013 – March 2014. The data showed that at higher geomagnetic rigidity there is a decrease in charged particle flux. The figure 2.5 shows measured proton flux as a function of L shells and energy. The particle has the maximum proton intensity at lower energy (26 MeV). The red plot shows double-peaked structure with the main peak near L = 1.6 and the secondary peak at 2. The low-energy main peak was primarily formed by the inward diffusion of injected solar protons over many years. Secondary peaks were due to recent solar injections that have not yet diffused radially inward. The gap between the peaks was due to solar minimum condition during there were no significant solar proton events. At higher energies (46 MeV, 66 MeV), the probes measured less proton

intensity with a significant gap between the two peaks or bumps [5].

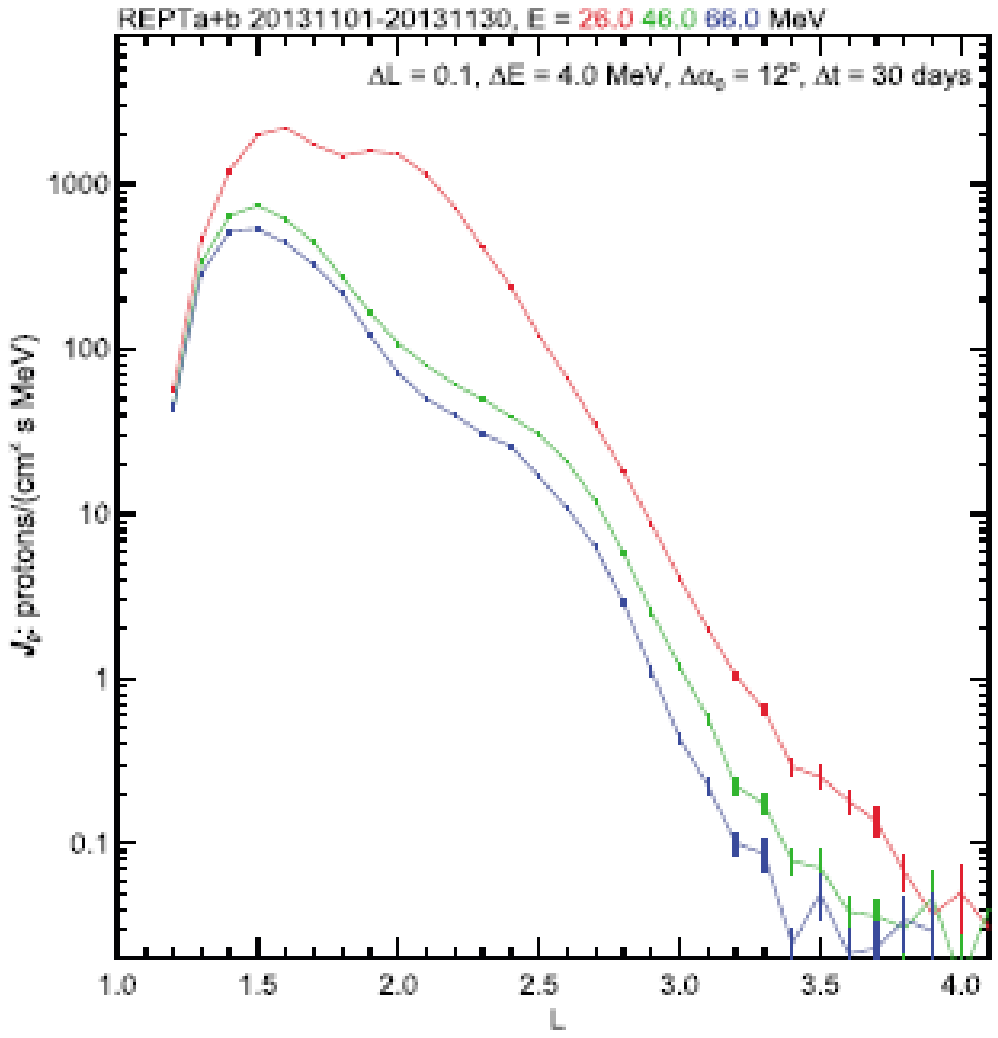

Figure 2.5: The above figure shows measured average equatorial differential omnidirectional proton intensity as a function of geomagnetic shells L. Three proton energies are represented in red (26 MeV), green (46 MeV) and blue (66 MeV). [5]

Figure 2.6 shows trapped proton equatorial pitch angle distributions at $\alpha_o = 90^o$. These peaks are narrow at low L values, because of the presence of the wide atmospheric loss cones. However, at L $>$ 2.2 the distributions began to narrow again. This narrowing is caused by trapping limits, which is the maximum energy of trapped protons as a function of L and α_o. These limits are lower at higher L values, and at low and high pitch angles α_o. Studies also showed that above the trapping limits losses are mainly caused by magnetic field line

curvature.

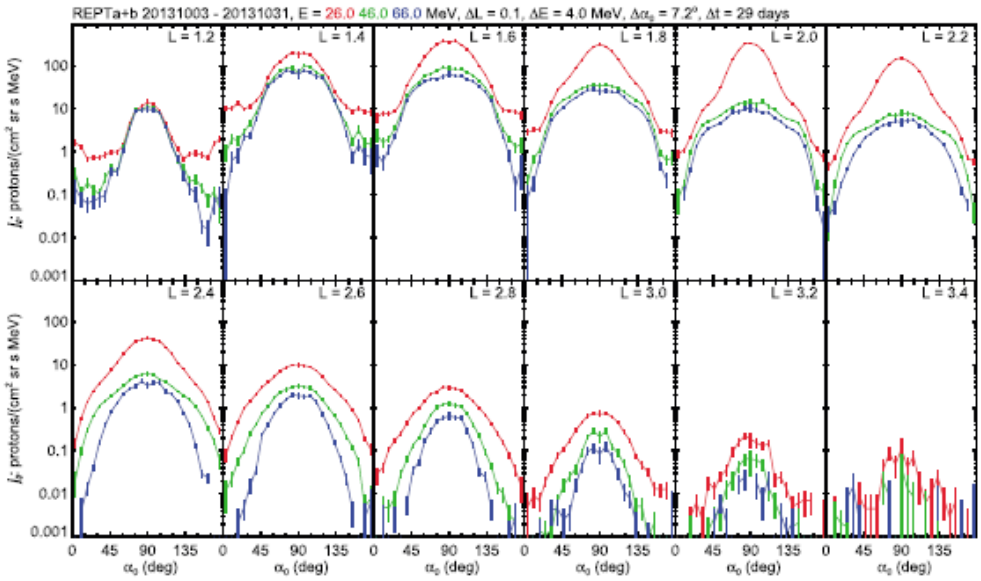

Figure 2.6: Van Allen probes REPT measurements of the equatorial distribution of protons as a function of geomagnetic L shell. The neutron flux is plotted for three different proton energies (E = 26MeV, 46 MeV, 66 MeV) shown in red, green, and blue color. [5]

The probes equatorial angle distribution are compared with the model. Figure 2.7 shows equatorial pitch angle model that includes CRAND, and solar protons as the key sources populating the inner belts. The narrow pitch angles at 90^o of the trapped solar protons depict that its intensity at low altitudes ($<$ 1000 km) must decrease significantly. Also, the measurements of proton from low-altitude satellites show that CRAND is the key source populating inner part of the radiation belt (Selesnick et al. 2010). The figure 2.7 show little variability caused by solar protons at higher altitudes.

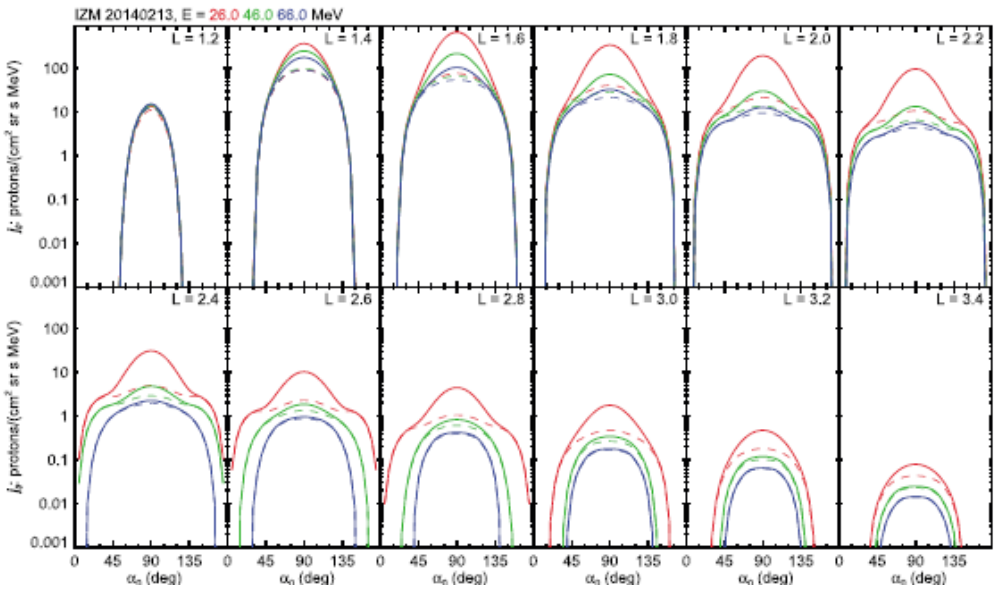

Figure 2.7: Equatorial pitch angle distribution model averaged over REPT FOV. The proton energies are identified by color. Solid lines include CRAND and solar proton sources, whereas dashed lines only include CRAND source. (See Selesnick et al. 2007, 2013) [5]

Overall, the probes data assisted us in understanding the Sun's influence on the Earth and near-Earth space by studying radiation belts as a function of space and time. Since high energy protons ($\geq$100 MeV) dominates the inner radiation belt and are relatively stable than electron (100 keV), it is essential to understand the dominant source of the inner proton radiation belt and develop a theoretical model that would be of practical value for low and mid-altitude satellite's orbits.

2.2 Origin of Albedo Neutrons (GCR)

2.2.1 GCR (Galactic Cosmic Ray)

Galactic Cosmic Rays (GCR) are charged particles accelerated to very high energy in processes outside of our solar system. The positively charged particles are comprised of 83% hydrogen (protons), 13% alphas, 1% element with Z $\geq$ 2. These cosmic rays are isotropic outside our heliosphere, with energy range from few MeV to 10^{20} eV. As these particles propagate through the heliosphere, they are influenced by the Sun's magnetic field. The

solar wind modulates a fraction of lower energy GCR, reducing the flux of energetic particles reaching the Earth during solar maximum and vice-versa during solar minimum ([15]). These cosmic particles (mostly protons) eventually interact with the Earth's atmospheric constituents (primarily oxygen and nitrogen) and give rise to albedo neutrons and other secondary particles.

2.2.2 Flux of Albedo Neutrons

Earth's dipole magnetic field act as a momentum analyzer to cosmic ray flux. When a cosmic ray reaches the Earth's magnetosphere, it experiences a Lorentz force which gyrates the particle along the Earth's magnetic field lines. High energy particles will have high resistance to the deflection of the geomagnetic field (See figure 4). Thus, it is important to understand and quantitatively measure the shielding provided by geomagnetic field to the incoming particles. This concept is known as the geomagnetic cutoff rigidity. More precisely, geomagnetic cutoff rigidity allows us to predict the charged particles transmission through the magnetosphere to a specific location as a function of direction (see equation vii). Using the Lorentz equation, we can specify the relationship between a charged particle momentum and Earth's magnetic field. The equation (i) below describes the Lorentz force on a charged particle and equation (vi) illustrates the rigidity of a charged particle.

$$F = q(E + v \times B) \tag{2.1}$$

where E = 0

$$F = qv \times B \tag{2.2}$$

Rigidity (R) of a particle would be:

$$F = qvB \tag{2.3}$$

$$mv^2/r = qvB \tag{2.4}$$

$$r = mv/qB \tag{2.5}$$

$$Br = R = p/q \tag{2.6}$$

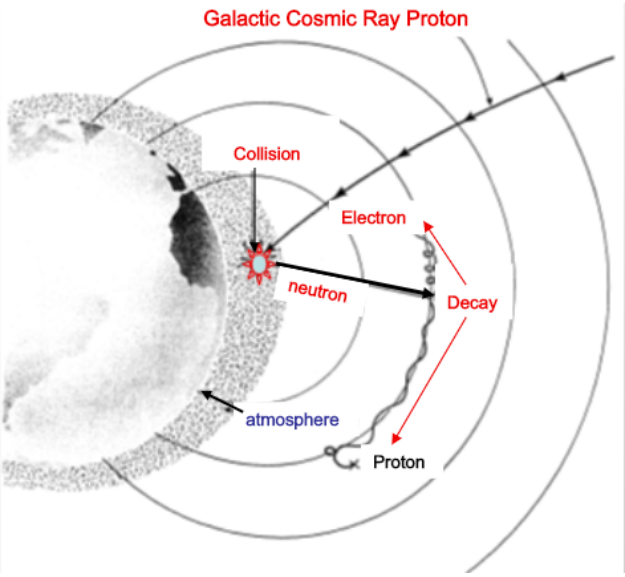

Figure 2.8: Galactic Cosmic Rays (GCRs) with higher energy (higher rigidity) interact with the Earth's atmosphere at LEO and may produce albedo neutrons. Furthermore, free neutrons decay into protons and electrons eventually feeding the Van Allen belts[W.N Hess 1968]

Particles carrying high momentum per charge (rigidity) exceeding the geomagnetic cutoff rigidity are able to penetrate the field lines and undergo nuclear interactions with the Earth's atmosphere. The interactions produce secondary particles that may include albedo neutrons. If the charged particle rigidity is less than geomagnetic cutoff rigidity, it will not be able to penetrate the field lines. This demonstrates how the local neutron intensity can be a function of local cutoff rigidity. Using the Störmer cutoff rigidity formula, we can define the geomagnetic cutoff rigidity as a function of magnetic latitude, radial distance from the Earth, and the arrival direction of the particle in terms of the local zenith angle. This can be mathematically written as:

$$R_c = \frac{qMcos^4\theta}{[r^2(1+\sqrt{1+cos^3\theta sin\phi})]^2} \tag{2.7}$$

R_c = cutoff rigidity in GV

M = magnetic dipole moment of the Earth

θ = Magnetic latitude

r = radial distance of the point from the origin of the magnetic coordinate system

ϕ = local zenith angle

Within the vicinity of the Earth, the phase of the solar cycle indirectly modulates the upward moving neutron flux by modulating the local cosmic ray flux. In a nutshell, the growing solar wind particles exert a solar wind pressure on the GCR, modifying its flux into the magnetosphere. At solar maximum (max sunspots), the wind pressure is much higher, diminishing the GCR flux, and the reverse happens at solar minimum. To understand the relationship between GCR and heliosphere, we need to appreciate the Parker transport equation. For a steady state, the Parker transport equation represents three physical processes: (a) diffusion, (b) convection, and (d) adiabatic deceleration that together control the propagation of such cosmic rays inside the heliosphere. All four processes could be summed in the Parker transport equation [16]:

$$\frac{\partial f}{\partial t} = \frac{\partial}{\partial x}[k(x,p)\frac{\partial f}{\partial x}] - U\frac{\partial f}{\partial x} + \frac{1}{p^2}\frac{\partial}{\partial p}(p^2 D_{pp}\frac{\partial f}{\partial p}) + \frac{p}{3}\frac{\partial U}{\partial x}\frac{\partial f}{\partial p} + Q \tag{2.8}$$

where f = f(x,p,t) represents the distribution function of energetic particles with momentum p at position x and time t. The position of the particle is perpendicular to shock.

U: It is the plasma (fluid) velocity in the x direction. k(x,p): Spatial diffusion coefficient

D_{pp}: The diffusion coefficient in momentum space Q: Source term

In the above equation, the first term on the right-hand signifies diffusion of cosmic ray flux. The cosmic rays traversing through solar wind encounter a radially outward flux of solar wind particles that causes fluctuations in the Interplanetary Magnetic Field (IMF).

The disturbance in the magnetic field causes scattering of the cosmic rays. The associated diffusion is larger along the magnetic field than normal to it. The outward flow also results in the convection (second term) of the cosmic rays that could eliminate the particles depending on the solar wind speed. The third term represents the diffusion coefficient in momentum space and the fourth term illustrates the adiabatic deceleration of cosmic rays. The last term states that as the solar wind expands, the trapped cosmic particles in IMF start to cool down like a gas-cooled by adiabatic expansion against a piston. This strange nature of particles is best observed at lower energies of cosmic rays. [17]

2.2.3 A model of the albedo neutron flux in Low Earth Orbit (LEO)

Many different types of detectors and electronics operated in Low Earth Orbit (LEO) are susceptible to albedo neutrons. On orbit, instruments experience a higher flux of charged particles in regions of lower rigidity (such as near polar regions) or in the vicinity of the radiation belts (such as the South Atlantic Anomaly, SAA). This consequently increase the instruments background noise level. This requires shutting down the electronics to prevent catastrophic damage from the charged particles. Recent observations showed that albedo neutrons are primarily responsible for populating charged particles near LEO. Claret et al. (2014) modeled the distribution of albedo neutrons encountered in space and compared it with previous measurements. The model included the spectrum, composition, and trajectory of cosmic rays passing through the geomagnetic field.

Using FLUKA code, Claret et al. (2014) modelled Monte-Carlo simulations to compute atmospheric neutron flux as a function of solar modulation and the Earths geomagnetic field. The model was primarily designed to determine the distribution of albedo neutrons encountered in LEO. The model could also be used to predict temporal variation of the neutron flux along the Earth orbit and reduce background noise in space instruments near LEO (Low Earth Orbit). The model includes spectrum, composition, and trajectory of cosmic rays passing through the geomagnetic field and Earth's atmosphere.

Cosmic Rays

Claret et al. derived the GCR (Galactic Cosmic Ray) spectra from Badwhar and O' Neill (BO) model, which essentially covered the elements from Z = 1 to Z = 28. During the computation of the spectra, the older version of BO model (1996) was slightly modified and then compared to the latest model (2010) (See T.K. Gaisser text). The model also included solar modulation ϕ to modulate the GCR. In figure 2.9, both red and blue spectra are coincident at solar minimum (450), but at solar maximum (465) the red spectrum is slightly above the blue spectrum.

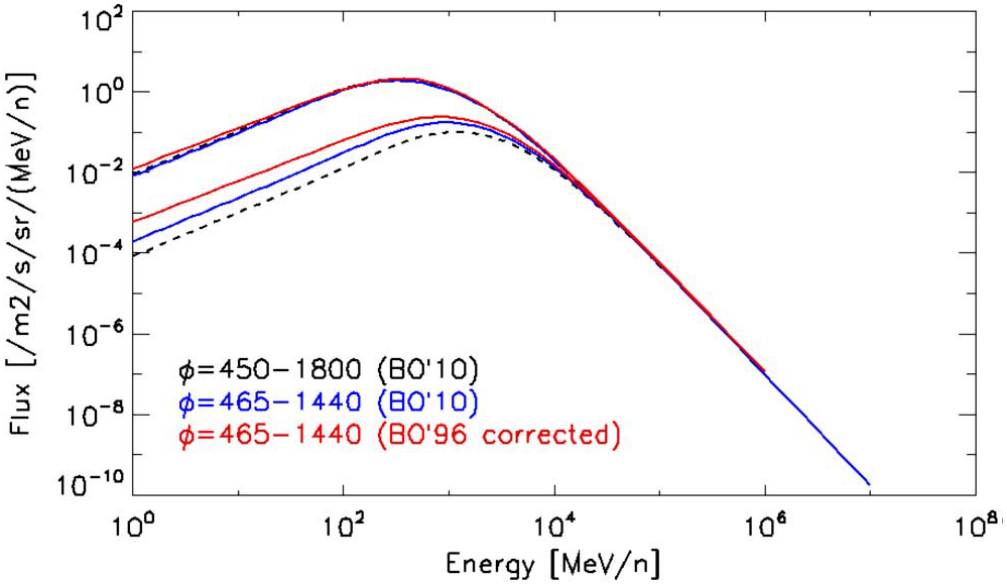

Figure 2.9: The above plot illustrates cosmic protons for various solar modulation. The black dotted spectrum corresponds to maximum value of solar activity and blue ones to more typical values derived from latest BO model (2010). The red spectra were derived from old BO model (1996) and plotted for comparison purposes [6].

Particle Transport

In the model, Claret et al. divided the GCR transport to Earth into two steps. The first step included cosmic ray particles before interaction with the Earth's atmosphere, and second step described the GCR products after the collision with the atmosphere constituents. In addition, Claret et al. used the Stoermer equation to model the incident GCR as a function

of various geomagnetic rigidity cutoff values, particles energy and direction at an altitude 10000 km from the center of terrestrial spheroid.

Earth's Atmosphere

In the model, the Earth's atmosphere was modelled as a superposition of concentric spheres with a density of 0.092 g/cm^2 at maximum altitude of 70 km and 10344.4 g/cm^2 at ground level. The atmospheric layers were primarily composed of 78% N_2, 21% O_2 and 1% Ar. The surface of the Earth was modelled as a perfect absorbing material that could absorb albedo neutrons generated from the ground and could be neglected in our model.

Particle Interactions

To accurately simulate the production of secondary particles induced by GCR interaction with the Earth's atmosphere, Claret et al. used FLUKA hadronic models. The model included PEANUT (Pre-Equilibrium Approach to Nuclear Thermalization), covering wide energy range from 5 GeV-20MeV and DPM (Dual Proton Model) that covered few ten of TeV. The albedo neutron flux was computed above New York in a dry atmosphere at solar minimum condition (465). The figure 2.10 below shows the neutron flux for various energy. The FLUKA model was integrated in the energy band 1-10 MeV (dark solid line) and compared with the WN (Wilson and Nearly) model for various Cr values (dark dashed lines). The WN model provided integrated neutron flux as a function of geomagnetic rigidity 2.08 GV (New York), atmospheric depth, and the neutron monitor rate Cr. The model showed good agreement at Cr = 83, that was also parallel with the Claret et al. hypothesis at solar maximum. Using the figure 2.10, we can observe neutron flux at various altitude ranges.

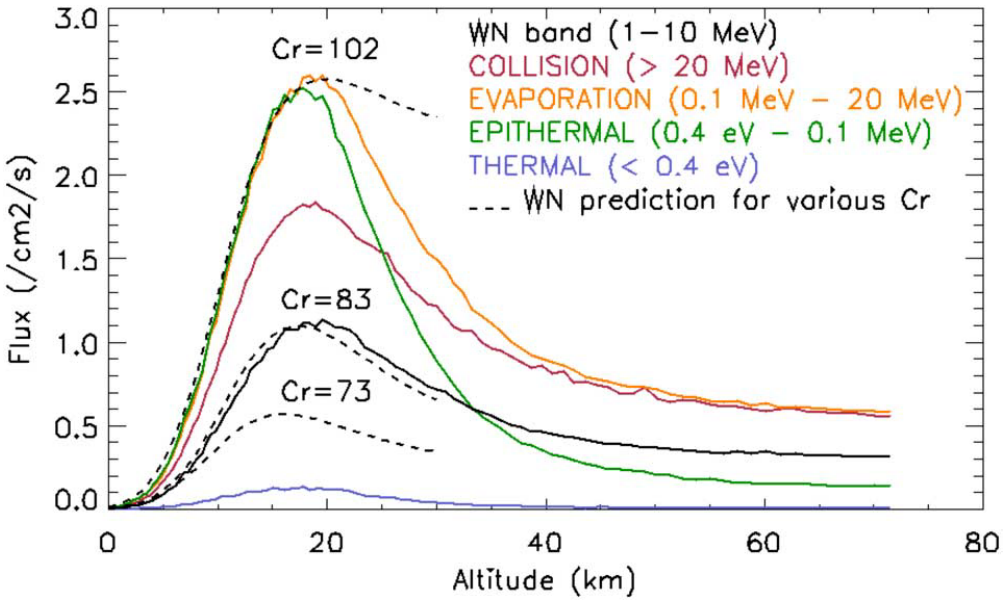

Figure 2.10: The above plot simulated albedo neutron flux in a dry atmosphere as a function of altitude. The neutron flux was integrated at various energy bands. Claret et al. model covered the energy range 1-10 MeV (dark solid line) and compared it with WN model for various CR values [6].

Spectral and Spatial Distribution

The distribution of albedo neutrons encountered at 400 km near the Earth's atmosphere was computed as a function of energy and angle of the incident particle. Furthermore, the albedo neutron flux was maximized by incorporating the solar minimum condition. For comparison purposes, a single data point (green) from Dsorgher et al. had been used to represent albedo neutrons above 1 MeV at solar maximum. The Figure 2.11 represents spectral distribution of neutron flux averaged over all directions of arrival (Claret et al.).

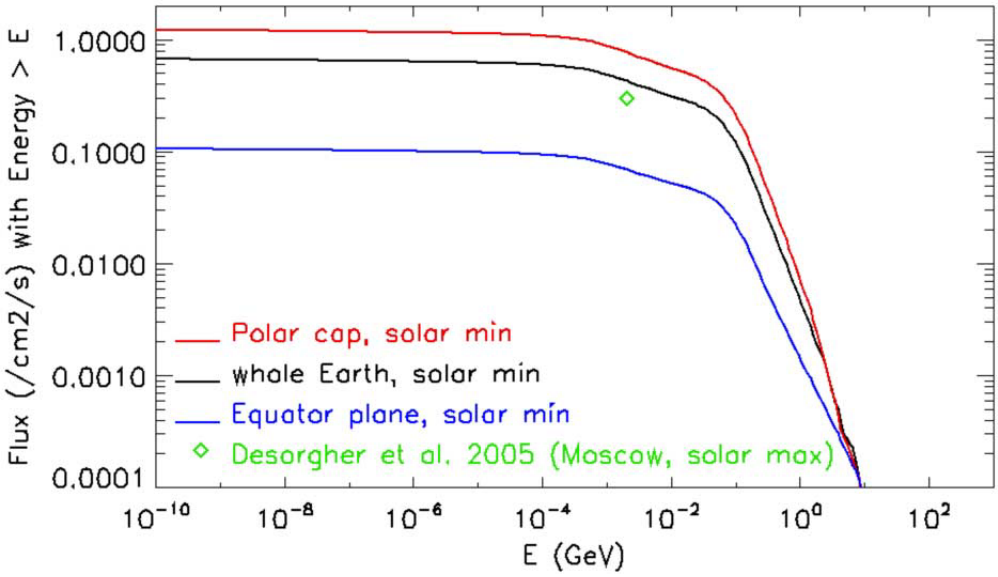

Figure 2.11: The plot showed spectral distribution of albedo neutrons accumulated over all directions at solar min condition. The neutron flux (red) was maximum at polar cap with an average over 72^o - 90^o latitude and minimum near the equatorial region (blue), at 18^o latitude. The neutron flux was also averaged over the whole Earth (black) [6].

Figure 2.12 shows the spatial distribution of albedo neutron flux. The neutron intensity is maximum near the poles and minimum near the equator (high cutoff rigidity GV). This shows that geomagnetic rigidity plays an essential role in attenuating the cosmic ray particles within the vicinity of the Earth.

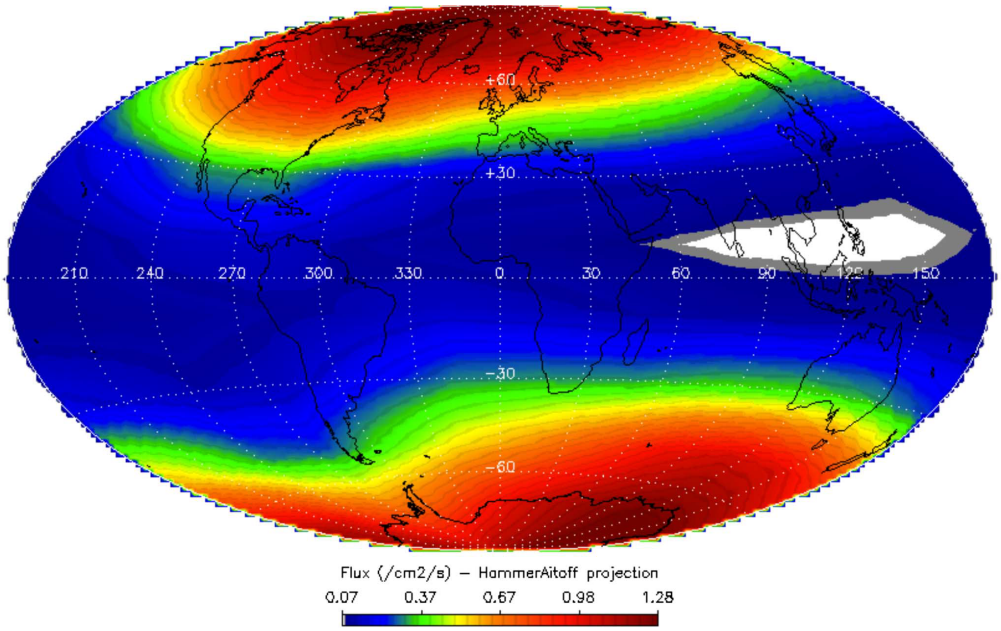

Figure 2.12: The model shows spatial distribution of upward neutron flux generated for energies less than 1 TeV. The neutron flux is maximum near the poles and minimum at equatorial region (high geomagnetic rigidity) [6].

In addition, Claret et al. compared the FLUKA model with the COMPTEL measurements of 1991 (Claret et al. 2014). The instrument provided two neutron measurements, each corresponding to a unique cutoff rigidity value. Claret et al. integrated the two neutron measurements to compute the flux in the wide energy range of 20-100 MeV and for rigidity cutoff values of 4.5 and 8.5 GV. Figure 2.13 shows the simulated data and the two COMPTEL measurements taken at 450 km above the Earth (Claret et al. 2014) [6].

Comparing Claret Model Calculation with COMPTEL Measurements.

The period of 1991 corresponds to the solar maximum during which the COMPTEL encountered relatively low albedo neutron flux. However, the figure 2.13 shows the COMPTEL neutron data to be more aligned with the solar minimum simulation. One of the possible reasons could be that COMPTEL also measured an extra contribution of neutrons from the Sun during some solar event. The simulations do not include any contributions from Solar Energetic Particle (SEP) events. Also, the instrumental background generated in the

CGRO instruments may have led to an overestimate of the measured neutron flux, which could account for this discrepancy. Claret et al. (2014) concluded that solar activity at the time of the COMPTEL measurements may account for this discrepancy.

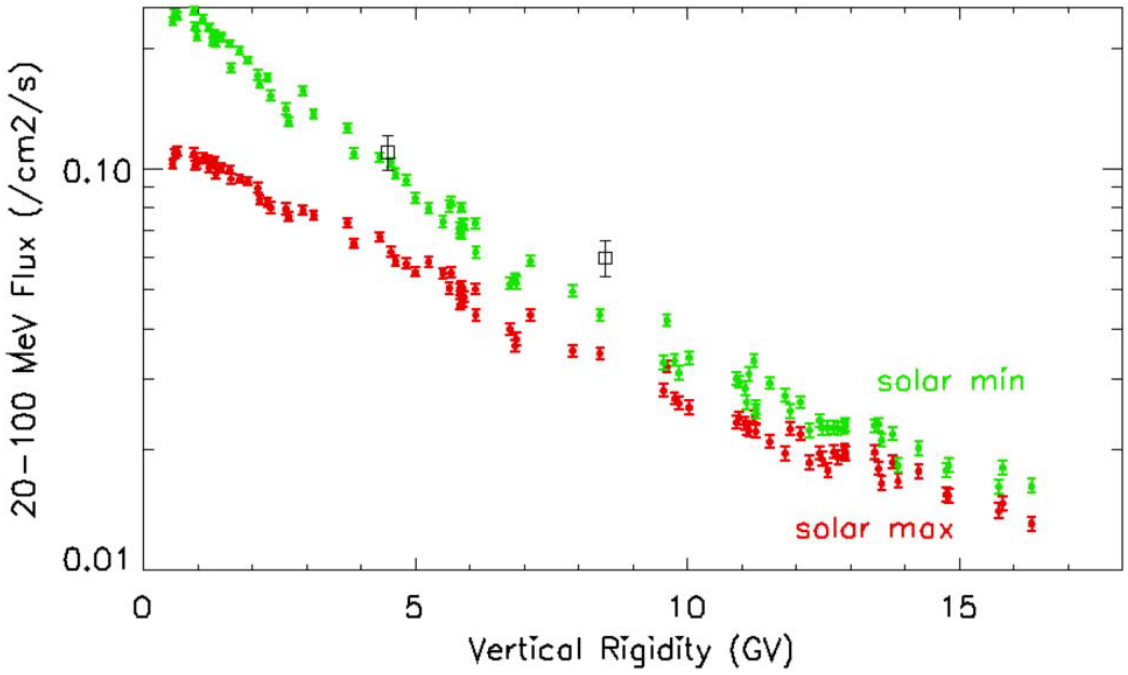

Figure 2.13: The plot compares the FLUKA albedo neutron model with two COMPTEL neutron measurements at different magnetic rigidities [6]

2.2.4 CRAND (Cosmic Ray Albedo Neutron Decay)

Theoretical model of the inner proton radiation belt

To study the dynamics of inner radiation belt, an accurate numerical model is needed that would let scientists investigate the sources populating the inner radiation belt. The model would play an integral role for low and mid altitude satellite orbits where radiation poses a great threat to astronauts and space electronics. Selesnick et al. (2007) created a theoretical model of the inner proton radiation belt that served as a basis to understand the inner belt variation as a function of time, sources and three adiabatic invariants (M, L, and K) in the kinetic energy range from 10 MeV to 4 GeV. The three adiabatic invariants are magnetic moment (M), bounce motion (K) and drift motion (L). The belt was primarily composed

of trapped protons that resulted from the Cosmic Ray Albedo Neutron Decay (CRAND), SEP's (Solar Energetic Particles), and radial diffusion occurring near Earth's atmosphere. Thus, the total proton source rate (CRAND, SEP, radial diffusion) becomes:

$$S = S_n + S_p + S_D \tag{2.9}$$

where S is measured in counts/sec.

CRAND

In the model, CRAND was chosen as a predominant source of inner belt proton. It's relatively a steady source, with variations only on the solar cycle. The proton source rate was typically determined by computing the neutron β-decay in a trapped proton shell, which mainly depended on the flux of albedo neutrons j_n, its decay lifetime t_n 8817s, neutron speed v, and the relativistic time dilation factor for a neutron energy γ:

$$S_n = \frac{< j_n >}{v * \gamma * t_n} \tag{2.10}$$

In the above equation, the j_n was calculated at the specific physical location where the trapped proton trajectory intersected the atmosphere at an altitude of about 100 km. However, if there was no intersection at a given site, then $j_n = 0$. Also, the average flux of albedo neutrons ¡j_n¿ was evaluated by averaging j_n over the complete path of a trapped proton and in the direction of the velocity, which gave the "drift average" of the proton intensity j_n:

$$< j_n >= \frac{1}{(s_2 - s_1)} \int_{s_1}^{s_2} j_n ds \tag{2.11}$$

In the above equation "s" represents the path length of the proton trajectory. To obtain reliable results, several drift averages were required for each geomagnetic field model [7].

Simulating GCR (Galactic Cosmic Rays) and Albedo Neutron

Using the Monte Carlo simulation, Selesnick et al. (2007) incorporated the incident GCR flux (H and He) for modeling the albedo neutron flux. The simulation sampled an isotropic distribution of GCR with kinetic energies ranging from 20 MeV to 100 GeV for H and from 20 MeV/nucleon to 7 GeV/nucleon for He. To accurately determine the interaction of incident GCR on an atmosphere, a simulated atmosphere was generated that included different layers with a thickness of 1 km extending up to 400 km altitude. The properties of each atmospheric layer were kept constant. The results for the albedo neutron flux spectra are shown in Figure 2.14, which includes spectra for various geomagnetic cutoff values (0.0, 4.83, 12.90) and different values for the solar radio flux. These model spectra are compared with published measurements in Figure 2.10.

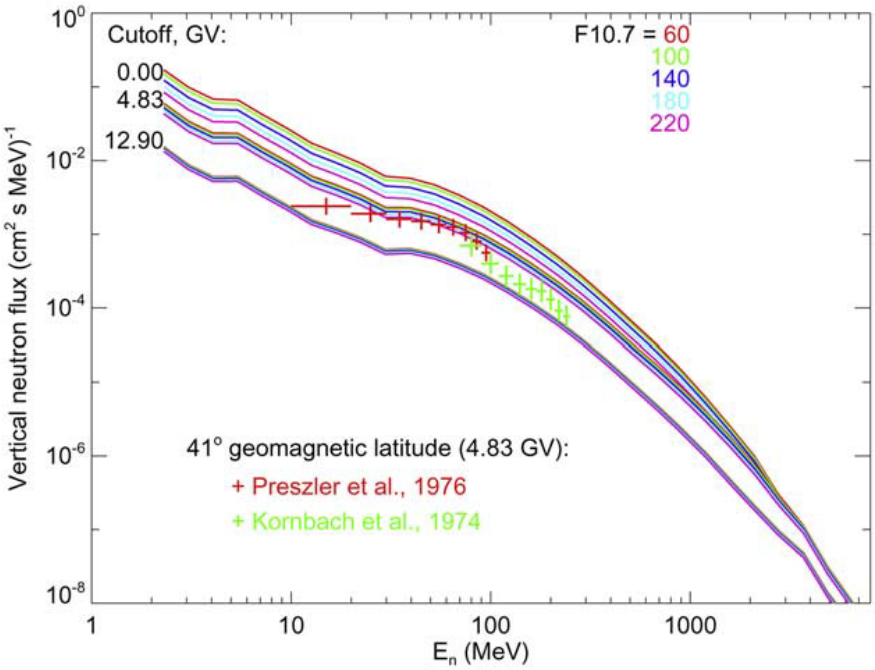

Figure 2.14: The plot represents albedo neutron flux as a function of kinetic energy, geomagnetic rigidity, and solar radio flux F10.7. Vertical neutron flux at 4.83 GV is shown for comparison with measurements obtained at a fixed geomagnetic latitude [7].

Figure 2.15 shows the vertical neutron flux as a function of neutron energy. At each cutoff rigidity (0.00 GV), spectra were obtained for all solar radio flux (F10.7) values. At

high rigidity values the neutron flux was resistant to solar modulation and solar radio flux F10.7. Although the neutron flux is relatively low at high cutoff rigidity values, it is still the predominant CRAND source for the inner proton radiation belt. Figure 2.15 below shows the GCR spectra as a function of sunspot numbers for H and He ions. It is quite evident that solar cycle modulated the GCR flux and consequently the production of albedo neutrons and its decay products.

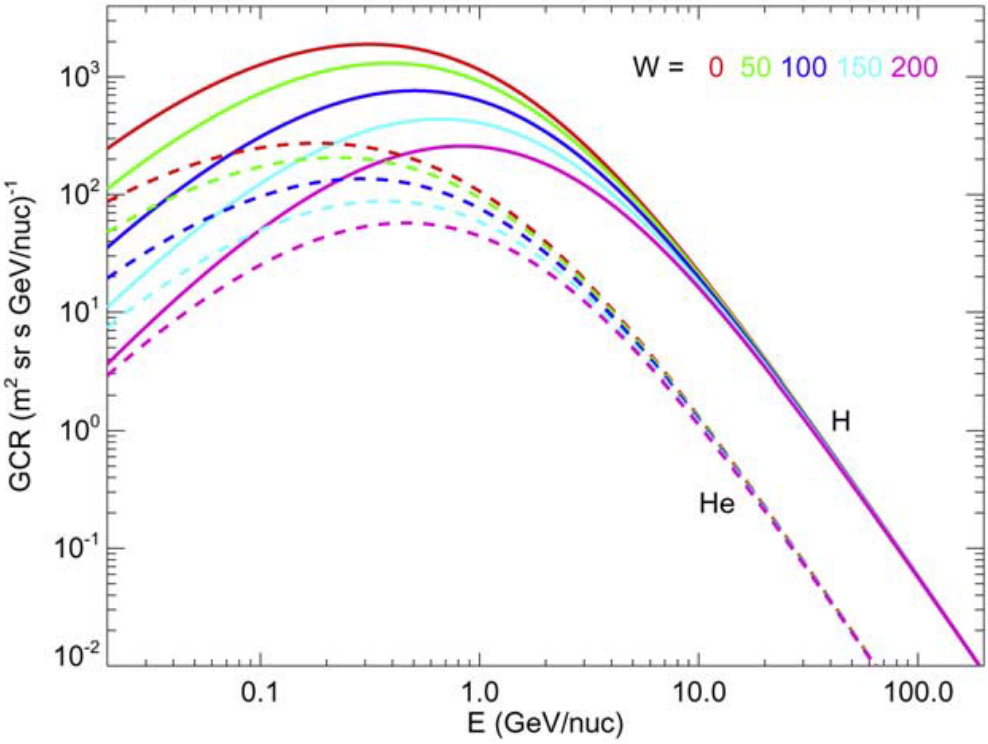

Figure 2.15: The above plot represents the GCR spectra of H and He as a function of sunspot numbers W. [7]

Analyzing measurements of the CRAND proton from the HEO-3 (High Elliptical Orbit) satellite.

After postulating the decaying neutrons as a source of charged particles in the radiation belts, scientists began to study the albedo neutrons in the upper atmosphere. In 1958, Singer et al. proposed this idea, and later in the 1960s, CRAND was introduced as an essential theory of populating the inner belt protons. When an albedo neutron decays into a proton and

an electron, most of its kinetic energy is transferred to the proton, while the electron gains kinetic energy from the binding energy of neutron, which was approximately 0.7 MeV [7].

$$n_a \rightarrow p^+ + e^- + v_e \tag{2.12}$$

If a neutron decayed inside the inner radiation belt, the resultant products became trapped in the inner radiation belt. Due to non-linear interaction between EMIC (Electromagnetic Ion Cyclotron) waves and radiation belt electrons, most of the electrons are lost to the upper atmosphere, depleting inner zone electron radiation belt. As a result, high energetic protons dominate in the inner radiation belt. One notable observation of CRAND protons took place during the storm of 20 November 2003, which swiped away trapped protons, consequently emptying the inner region. It was an opportunity to directly measure the proton source rate of the inner radiation belt. In late 2003, HEO-3 (Highly Elliptical Orbit) satellite measured protons of energy range 27-45 MeV within the inne radiation belt. The measurements showed that the trapped protons intensity increased with time in the region $2.1 \leq \mathrm{L} \leq 3.2$, at a rate consistent with CRAND being the predominant source of protons [9].

To better understand the source of inner belt protons, Selesnick created two different radiation models (CRAND model and inner zone model) and compared them to HEO-3 data. Figure 2.16 (left) compares the trapped proton source intensity to an expected CRAND proton intensity as a function of L and time. Three data subsets were enclosed in white dashed lines (1,2,3) that were mainly used for closer comparison to the CRAND model results. To extend the existing model, Selesnick et al. (2013) generated an inner zone model that included several proton sources (CRAND source, solar proton trapping, radial diffusion, and losses) and used it for comparison purposes (Figure 2.16 right).

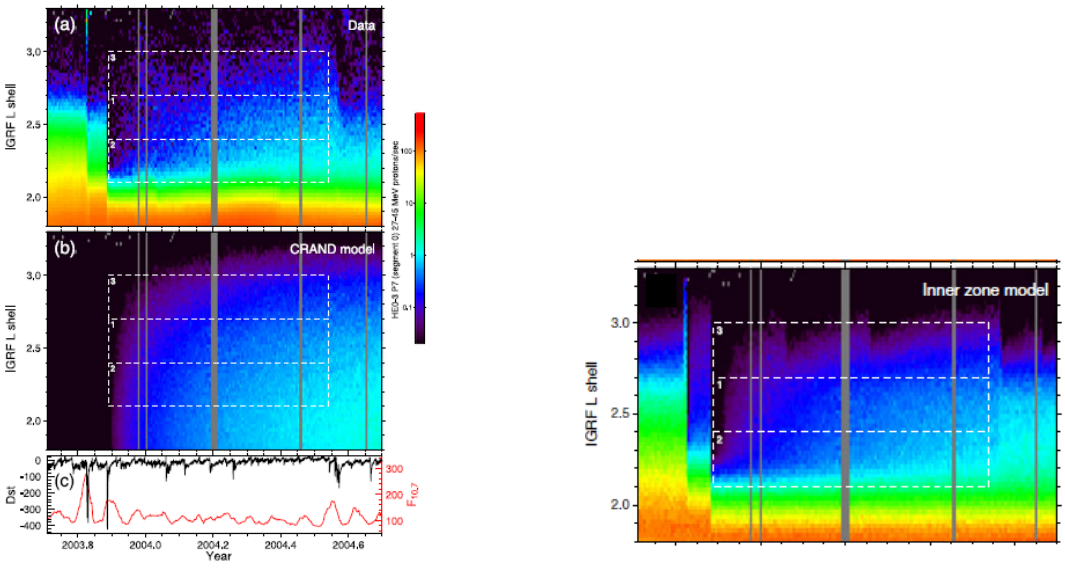

Figure 2.16: The above plots represent the HEO-3 satellite data and corresponding CRAND model. The plot (a) on left shows the trapped proton intensity at an energy range of 27 – 45 MeV at a region 2.1≤L≤3.2. Plot (b) shows the CRAND model, whereas plot (c) depicts the geomagnetic disturbance (black) and solar radio flux F10.7 (red) for the corresponding year. The data enclosed in white dashed lines 1,2,3 are subsets of data used for comparison purposes. The plot on right represents the inner zone model. [8]

For each data subset, an averaged over L shells was computed and plotted as a function of time. Figure 2.17 below shows the average value plots for a given subset. The subset 1 corresponds to region $2.4 \leq L \leq 2.7$. It shows a linear increase with time and correlates with both models. For subsets 2 and 3, the data and model do not correlate with each other. For subset 2, both models underpredict the proton intensity, whereas, for subset 3 the CRAND model only overpredicts the proton intensity. The most likely reason for a variation in the model and data is the significant contribution from a physical process called radial diffusion. The radial transport could simply transport protons from their existing limits and reduce both the CRAND source model and inner zone model. Incorporating the radial diffusion in our models could possibly improve our existing models and confirm the presumed CRAND source for inner proton radiation belt. [9].

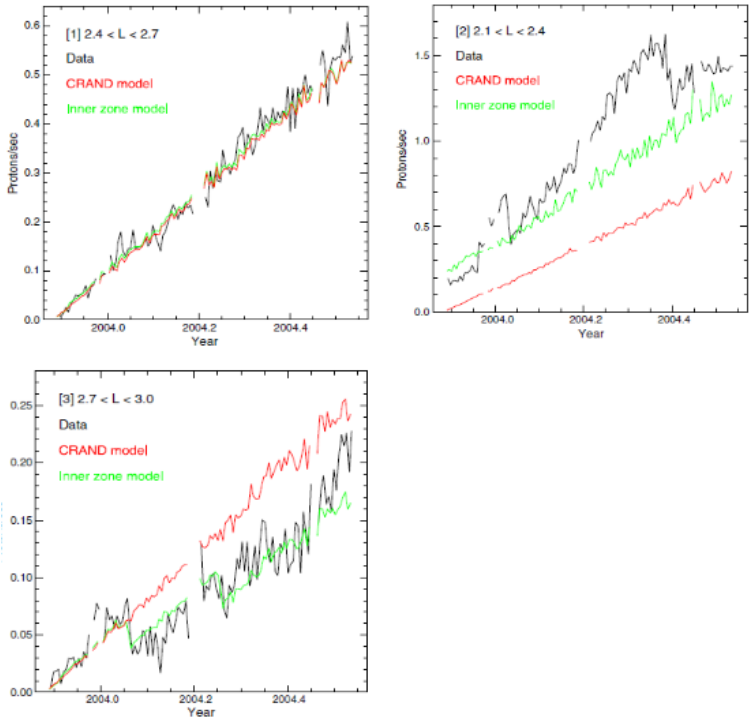

Figure 2.17: The above plots represent average results from HEO-3 satellite and two simulations. The upper left plot corresponds to subset 1 data, showing a linear increase with time and correlating with the models. Similarly, the other two plots correspond to subset 2 and 3 showing a similar pattern. [9]

2.2.5 Previous studies and measurements

COMPTEL measurements of the omnidirectional high energy neutron flux in near Earth orbit

In a research paper, Morris et al. performed a detailed analysis of the COMPTEL omnidirectional D1 measurements obtained on four different occasions: twice in 1991 and twice in 199. The measurements included high energy neutron flux ($\geq$12.8 MeV) near an altitude of 450 km. Morris observed that when spacecraft pointed at 0^o zenith angle (pointing towards nadir) , the albedo neutron flux measurements were consistent with previous models. However, when the spacecraft was pointed at 180^o zenith angle (looking in outer space) , the flux was reduced by a factor of 0.54. This was due to spacecraft mass acting as a shield to albedo neutrons. The COMPTEL D1 module was normally operated at 70 keV, however,

Day	Time (UT)	Mt.Washington Rate	Rigidity Range (GV)	Zenith Angle Range
8 July 1991	1200-1230	1659	4.8-13.6	$59^o - 74^o$
12 December 1991	1752-1925	2010	7.7-15.5	$3^o - 177^o$
26 August 1994	1224-1405	2340	7.7-15.5	$8^o - 172^o$
14 September 1994	0854-0931	2330	4.7-13.6	$49^o - 83^o$

Table 2.1: COMPTEL albedo neutron flux measurements and Mt.Washington neutron monitor rates. [1]

during the neutron measurements it was operated at 12.8 MeV threshold, which reduced the event rate and consequently removed dead time corrections. The table 1 summarizes the measurements of the COMPTEL at four different times. It also gives the simultaneous measurements of Mt. Washington neutron monitor rates. The first two measurements were made near solar maximum (1991). The rates are relatively low than measurements taken in 1994, which is near to solar minimum.

2.2.6 The Local Neutron Flux at Low Earth Orbiting Altitudes

Most of the high energy X-ray and gamma-ray experiments in LEO (Low Earth Orbit) are inevitably affected by local neutrons that contribute to instrumental background. These local neutrons consist of atmospheric neutrons and the production of secondary neutrons inside the spacecraft. Weidenspointner et al. (1996) discussed the COMPTEL measurements of the local neutron flux as a function of vertical cutoff rigidity, spacecraft pointing zenith, and spacecraft pointing azimuth angle. The absorption of a low energy neutron ($\leq$ 5 MeV) by a proton (hydrogen atom) atom in the D1 detector produced a 2.2 MeV gamma ray, which underwent double scatter in the same manner as cosmic photons. The resultant gamma ray produces a 2.2 MeV instrumental background line in the COMPTEL energy spectrum. Weidesnpointer et al. (1996) used the 2.2 MeV line intensity to study local neutron flux. He found out that mass shielding played an essential role in attenuating the albedo neutron flux. Also, the 2.2 MeV line intensity increases with decreasing rigidity and geocentric zenith angle, with rigidity having a stronger impact (see Figure 2.18). They also compared the variation of albedo neutron flux as a function of rigidity with the OGO 6

(Orbiting Geophysical Observatory 6) measurements. Their relative measurements were in good agreement with each other and consistent with earlier measurements. [10]

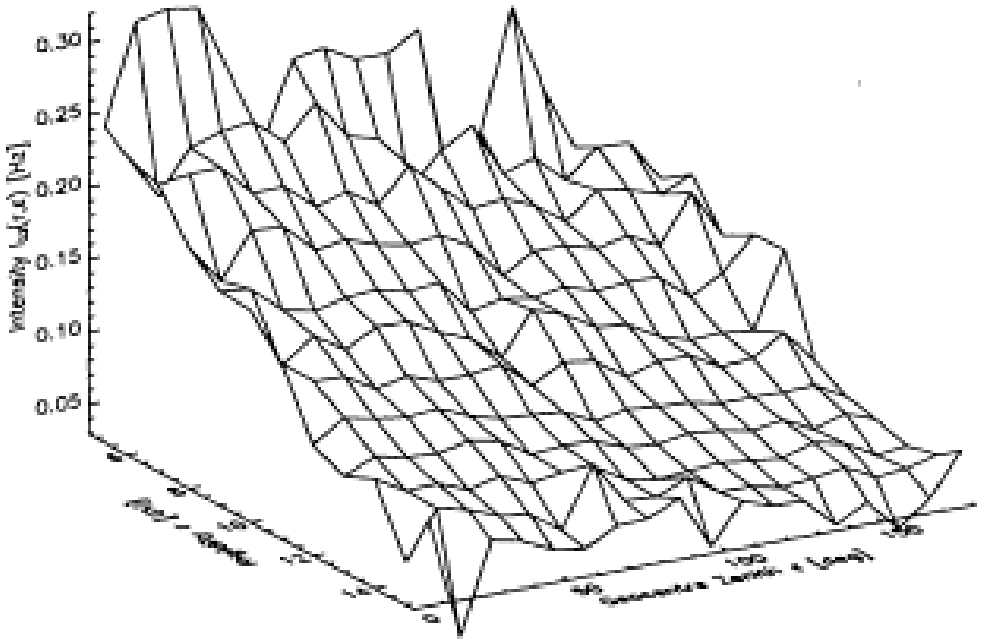

Figure 2.18: The above plot shows a 3D distribution of the 2.2 MeV line intensity as a function of rigidity, geocentric zenith angle [10]

2.2.7 Support for CRAND theory from measurements of Earth albedo neutrons between 70 and 250 MeV

Due to limited albedo neutron data above 100 MeV, two balloon flights on May 1 and 25, 1971 from Palestine, TX took neutron measurements in the energy range of 70 MeV to 250 MeV [Kannbach et al.1974]. The two detectors were set at float altitudes of 107 km and 120 km, which had corresponding atmospheric depth of 8.6 g/cm^2 and 4.7 g/cm^2. Each balloon flight carried an instrument that employed a double elastic scattering of neutron on protons. In the first interaction, the incident neutron elastically scattered off a proton in the D1 detector. The length of the recoil proton tracks gave the proton energies. Similarly, the second interaction was evaluated under the assumption of it being an inelastic scattering

event (Figure 2.19). After the completion of the balloon experiment , the measured neutron energy spectrum was compared with previous balloon experiments and Monte Carlo simulation of atmospheric neutrons. The results were compared to Preszler et al. balloon experiment of 1974. Figure 2.20 represents a comparison of the neutron flux as a function of zenith angle with Preszler measurement. [11]

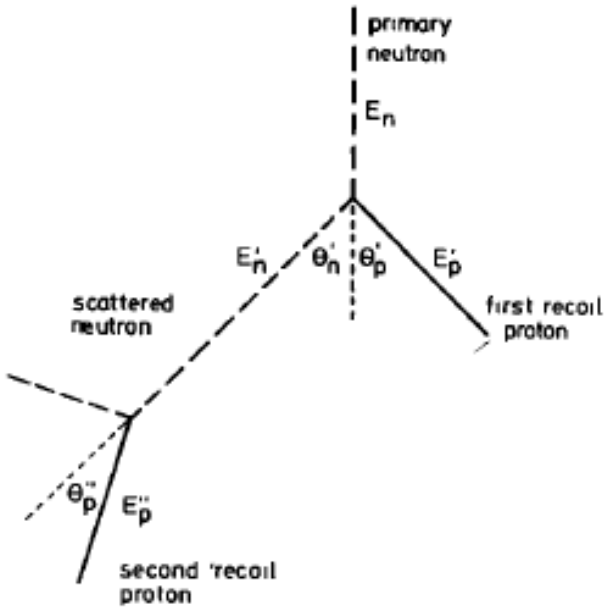

Figure 2.19: The instrument uses double elastic scattering technique to measure the neutron flux [11]

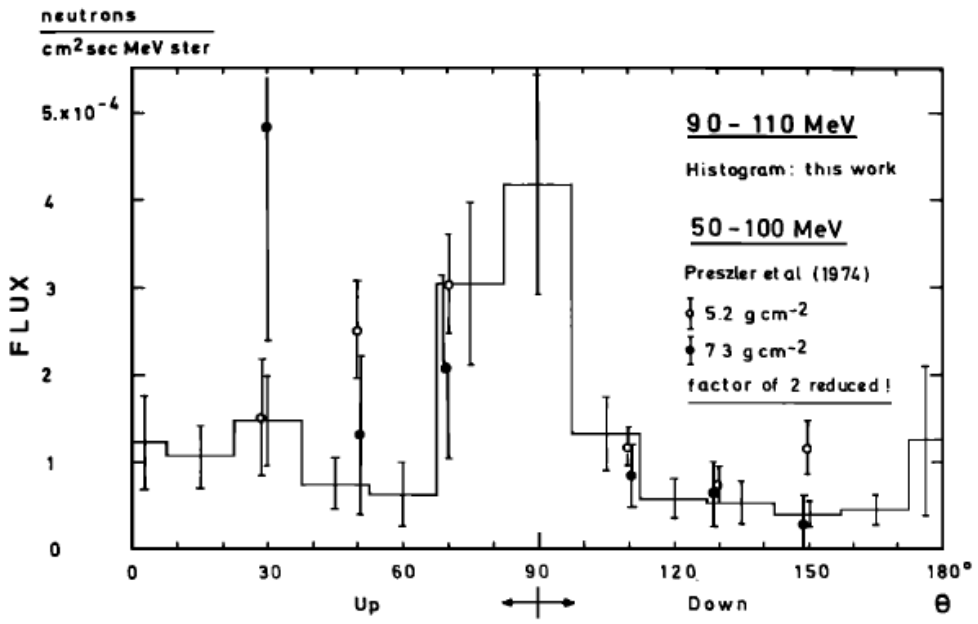

Figure 2.20: The above histogram represents angular distribution of atmospheric neutrons measured at an altitude of 107 km along with Preszler balloon experiment. The histogram shows a higher neutron flux at 90^0 zenith angle. [11]

The histogram has a pronounced peak at 90^o angle. This strong neutron intensity was due to cosmic ray alpha particles striking the Earth's atmosphere tangentially producing an optimal number of neutrons. We find good correspondence between the two experiments. In addition, the directional neutron fluxes provided means to compute the differential neutron leakage flux (neutrons/cm^2 s-MeV). The flux was compared with White et al (1972) and Eyles et al (1971) measurements (see figure 2.21, left). A least square fit was plotted to best fit the data for the energy interval 70-250 MeV. Assuming, both measurements constitute experimental errors there is a fair agreement in the energy interval 70-100 MeV, except a leakage flux identified at approximately 80 MeV. To evaluate the balloon experiment measurements with the CRAND theory, Kanbach et al. (1974) compared the least square fit curve with the Monte Carlo simulation derived by Light et al (1973), Merker et al (1972), and Armstrong et al (1973). He also compared the measurements with the Freden and White and Haerendel CRAND model. Figure 2.21 (right) shows the Kanbach et al (1974) data along with the theoretical predictions. There is a good agreement between the balloon

measurement and the Armstrong et al (1973) Monte Carlo simulation. In addition, Freden and White (1962), and Haerendel (1984) CRAND model predictions were also in agreement with the measured data. This shows that the balloon flight data supported the CRAND theory and confirmed the theoretical predictions for the production and transportation of albedo neutrons in the Earth's atmosphere.

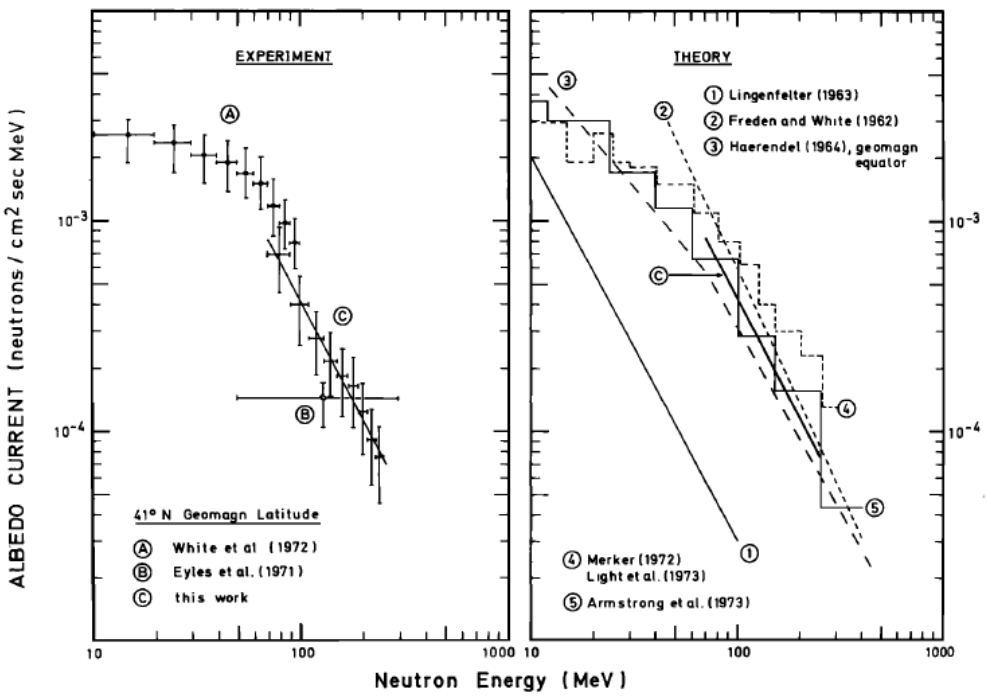

Figure 2.21: The above plots compare theoretical and experimental neutron flux with albedo neutron flux at 41^o geomagnetic latitude measured on May 1 and 25 1971. [11]

2.2.8 Preszler balloon experiment

In the 1970s, Preszler et al. launched a balloon payload carrying a neutron telescope that covered roughly a neutron energy of 10-100 MeV and zenith angles of 20^o – 70^o and 110^o – 160^o. The neutron telescope utilized two liquid scintillators to determine the direction and energy of an incident neutron (See figure 2.22). The energy of the incident neutron was derived from the sum of the recoil proton energy, in the first tank and the scattered neutron energy, determined from the time of flight to the second tank. Figure 2.22 shows the incident neutron interaction between S1 and S2 tanks. The incident neutron elastically

scattered of a proton (p1) at an energy En in the bottom S2 tank at a zenith angle (theta) and azimuthal angle (phi). The scattered neutron (n1) continued to the second cell and deposited its remaining energy to the second proton (p2) in the top S1 detector. [12].

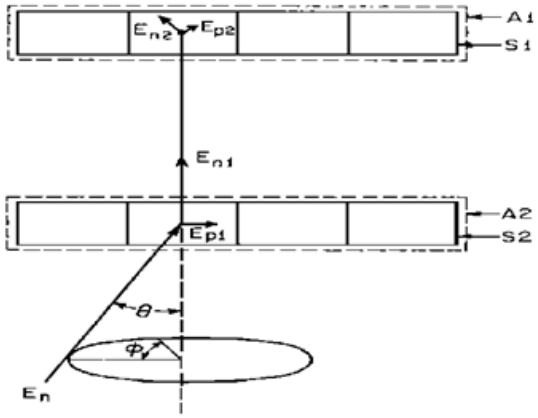

Figure 2.22: Incident neutron initially scatters at S2 from a proton p1 and deposit its remaining energy at S1 [12]

The incident neutron energy becomes $E_n = E_{n1} + E_{p1}$. Due to limitations of the telescope, the azimuthal angle was not obtained. The zenith angle was measured as

$$\theta = tan^{-1}(\frac{E_{p1}}{E_{n1}})^{1/2} \tag{2.13}$$

Preszler et al. compared the neutron telescope measurements with neutron monitor at 20, 40, and 55 MeV. The results were in good agreement with only 15% uncertainties. Theoretical albedo neutrons angular distributions (See Merker et al. 1975) were also in good agreement with the experimental values (See Preszler et al. 1976). Overall, the experimental results confirm the previous experiments performed by Kanback et al (1974) and successfully test the evidence that albedo neutrons are the prime source of protons in the inner radiation belt. [12].

2.3 Importance of Neutron Studies

The CRAND process in LEO (Lower Earth Orbit) plays a significant role in impacting the space weather and degrading the performance of space instruments. When an energetic neutron interacts with the space electronics it releases charge that creates ionizing radiation. The ionizing radiation can induce Single Event Effects (SEE) on electronics that poses a great threat to space instrument health. Thus, it is important to examine the interaction of neutrons and spacecraft to minimize the catastrophic damage to electronics and space missions. In addition, the albedo neutron studies would enhance our understanding of the albedo neutrons impacting the Van Allen radiation belt primarily inner proton radiation belt. Using the experimental data, we can test our previous CRAND models that could assist us in further understanding the albedo neutrons.

2.3.1 Single Event Effects (SEE)

The neutron effects on space borne missions causes radiation induce degradation in micro-electronics. When a high energy neutron enters the semiconductor lattice it may undergo elastic and inelastic collision with the target nucleus. These reactions can break target nucleus and generate secondary particles that can deposit energy along their paths. The secondary particles are heavier than the incident neutron and deposit charge densities that consequently causes SEE effects (for example memory fluctuation that produces false information). This type of error is usually a soft error and is called Single Event Upsets (SEU). The error is corrected by reprogramming the device or power reset.

2.3.2 Induced Background in Gamma Ray Detectors.

Neutrons interacting with the spacecraft structure (primarily Al) undergo nuclear interaction with the atomic nuclei of its material and form radioactive isotopes. This process is called neutron activation. It occurs when free neutrons are captured by atomic nuclei and trans-

formed into another nuclide. The resultant radionuclide decays by emitting a gamma ray photon. Most gamma-ray detectors are vulnerable to neutron activation that consequently populates the background energy spectrum. Thus, it is essential to study albedo neutrons as a function of various parameters to minimize the neutron induced gamma rays in most detectors.

CHAPTER 3

The Compton Imaging Telescope

3.1 CGRO (Compton Gamma Ray Observatory) Mission:

To perform the complete survey of the -ray sky, NASA launched four instruments onboard the CGRO (Compton Gamma Ray Observatory) mission on April 5, 1991. The Atlantis space shuttle placed CGRO into an Earth orbit of 450 km altitude and 28.5^o inclination. The CGRO mission carried four instruments (EGRET, COMPTEL, OSSE, BATSE), which together could detect γ -ray ranging from 20 keV to 30 GeV (Figure 3.1). The Energetic Gamma-Ray Experiment (EGRET) measured albedo gamma-rays between 50 MeV and 10 GeV. These albedo gamma rays were primarily caused by the interaction of cosmic rays with the Earth's atmosphere [18]. The Burst and Transient Source Experiment (BATSE) was primarily used to detect gamma-ray burst that seem to come from the cosmos. In addition to that, the Oriented Scintillator Spectroscopy Experiment (OSSE) consisted of collimated array to cover the energy range from 50 keV to 10 MeV. It was primarily used to cover the solar gamma-rays and neutrons and observe high energy emissions from pulsars [19]. Lastly, the Compton Telescope (COMPTEL), covering the energy range from 1 MeV to 30 MeV was mainly used to conduct comprehensive survey of the sky at MeV-energies. The data from CGRO was organized into viewing periods, with each viewing period defined by a fixed pointing direction on the sky. The nominal observation time of each viewing period was about 2 weeks [8].

Compton spent nine years in Earths orbit. After one of the CGRO's gyroscopes experienced a failure in April of 1999, NASA decided to destroy the CGRO instrument by bringing

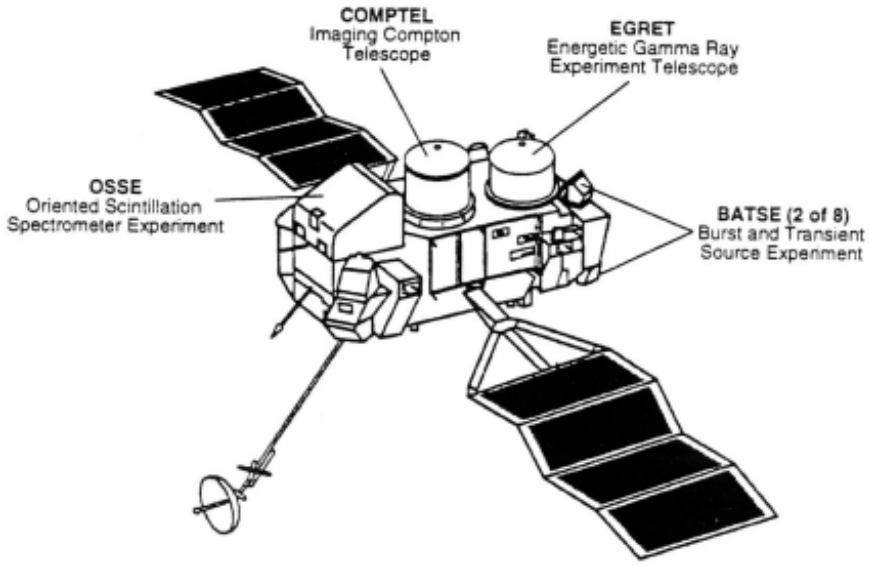

Figure 3.1: CGRO spacecraft equipped with four instruments (EGRET, BATSE, OSSE, COMPTEL) aboard [8].

it back to the Earth through a controlled re-entry. On June 4, 2000 CGRO re-entered the Earth's atmosphere over the Pacific Ocean.

3.1.1 Description of the COMPTEL instrument

COMPTEL was one of the four CGRO instruments that detected both γ-rays (1-30 MeV) and neutrons (10-200 MeV). It was a double scatter instrument that carried two layers of scintillator detectors known as D1 and D2, placed 1.5m apart. The first detector layer (D1) consisted of seven cells each of which was 28 cm in diameter and 8.5 cm deep containing low-Z liquid (NE213A) scintillator. Each liquid scintillator cell was viewed by 8 photomultiplier tubes that provided total light output (as a measure of energy). Each D1 cell was mapped with a gamma-ray signal from ^{60}Co source to determine the relative pulse height of each PMT ($\sum$ PMT#/ ^{60}Co) to the totaled signal ($\sum$ PMT/^{60}Co) for all possible positions (x,y plane) of a scattered gamma ray event in the cell (Figure 2).

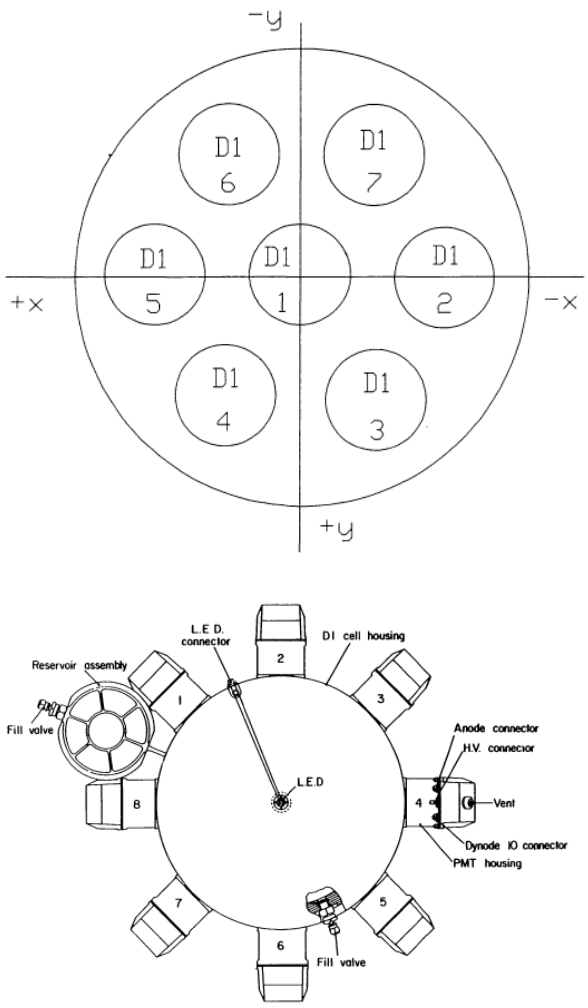

Figure 3.2: The top view of the D1 detector containing seven liquid scintillators distributed in x, y plane (Top). The bottom figure shows the top view of one the D1 detector modules. The liquid scintillator is viewed by eight PMT's to measure the energy deposit and determine the interaction location within the cell [8].

Pulse shape discrimination (PSD) was used in the D1 liquid scintillator to discriminate between the pulses from electron and proton ionization that resulted from scattered γ-ray events and neutron induced events respectively. The thickness of the D1 detectors was chosen to maximize the possibility of a single Compton scatter event (Figure 3).

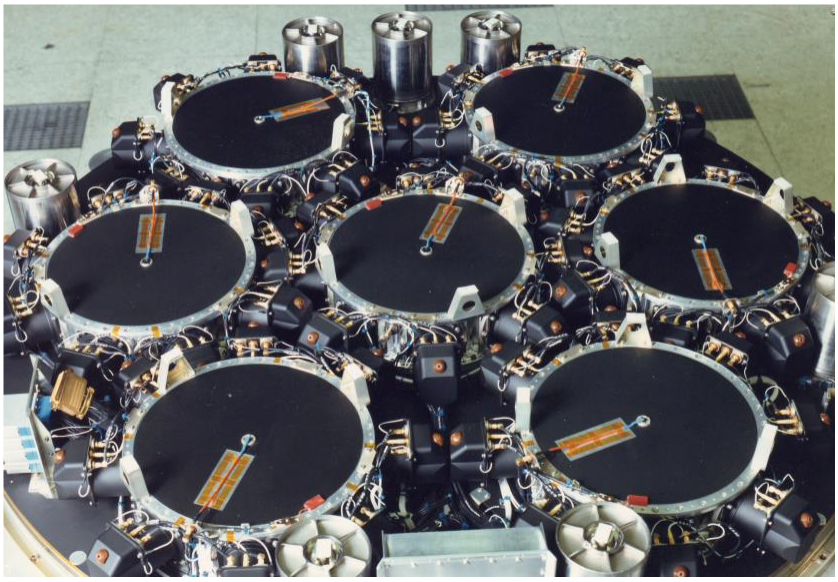

Figure 3.3: The top view of D1 detector layer containing seven liquid scintillator modules. Each scintillator cell was viewed by eight PMT tubes.

The liquid scintillator used in the D1 detector induced fluorescent light emission upon the interaction of the photons with the scintillator material. To accomplish this interaction, the liquid scintillator uses its two basic components, the solvent and solute (usually a phosphor). Initially, the energy was deposited in solvent molecule as excitation energy. Through thermal movement of molecule and diffusion changes, the excited energy was transferred to an adjacent molecule that created a dimer. The interaction of solvent molecules continued until it was contacted by a primary solute molecule to which the energy was fully transferred. An excited solute molecule was liberated within few nanoseconds of its excitation and emitted a fluorescence photon [20]. The visible light interacted with the cathode of the PMT and ejected an electron through the photoelectric effect. The resultant electron strikes the first dynode, which initiates a series of cascades of electrons that amplifies the output signal. The amplified signal generates a current pulse. As a result, the width of the current pulse discriminates the gamma-ray events from neutron events (See figure 4).

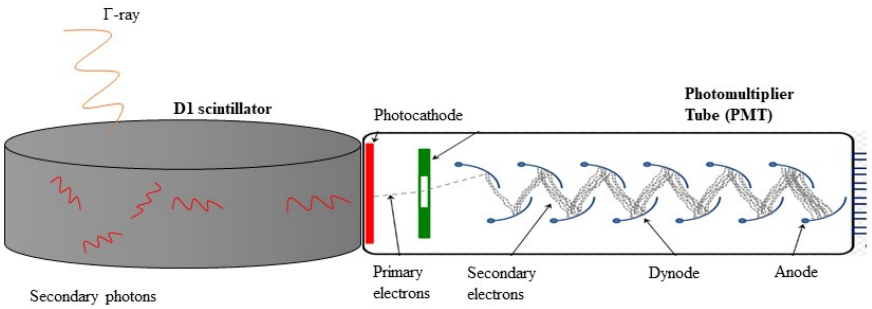

Figure 3.4: One of the D1 scintillators connected to one of the PMT.

The second detector layer (D2) consisted of 14 cells each of which with a diameter of 28.2 cm and thickness of 7.5cm containing high-Z NaI (Tl) scintillation crystals. Each detector was viewed by 7 PMT's that measured the total energy loss of a scattered photon or neutron. The operating energy range of these cells ranges from 650 keV to 30 MeV. The D2 thickness was chosen to provide a significant probability of absorbing a scattered photon in this energy range (See figure 5).

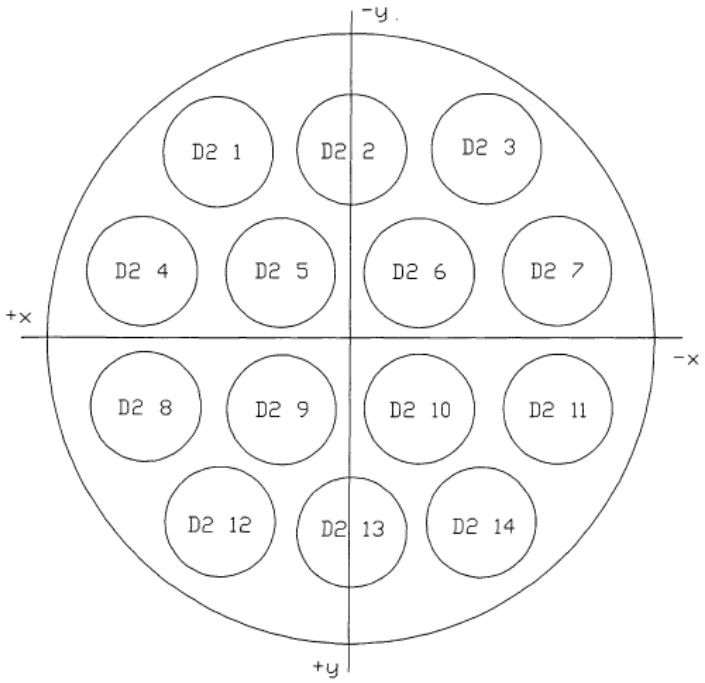

Figure 3.5: The top view of the D2 detector layer, containing 14 NaI scintillators distributed in x, y plane [8].

Upon interaction of gamma-ray with a D2 crystal (NaI), the recoil electron gained enough energy to move electron from valence shell to conduction band. As this happened, a creation of primary electron-hole pairs generated secondary pairs by a cascade effect. As a result, all the electrons occupied the conduction band and left paired holes in the valence band. After picosecond the free electron migrated back to the paired holes and emitted energy in the form of visible light (See figure 6).

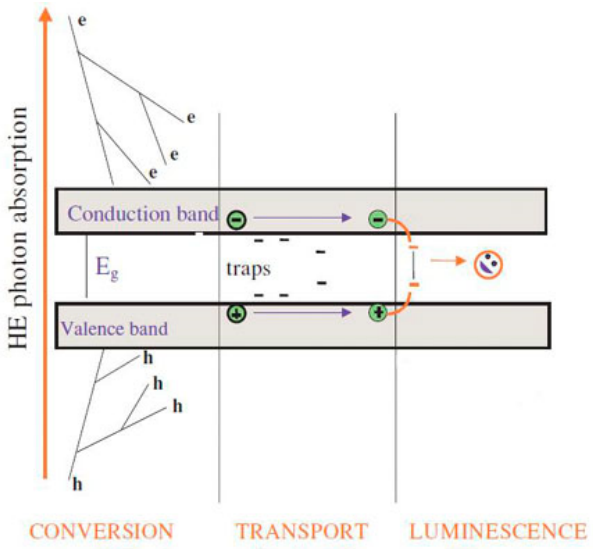

Figure 3.6: The above diagram shows the scintillation process. Initially, the radiation energy is absorbed by the electron in the valence shell. The electron is bumped up to conduction band and eventually de-excites to valence band and emits energy in the form of photon [13].

In an ideal gamma-ray event, a γ-ray was Compton-scattered in the D1 detector layer, and then the scattered γ-ray traversed to the D2 detector layer where it deposited its remaining energy. The sequence of events was confirmed by a Time-of-Flight (TOF) measurement, that measured the time-of-flight from D1 to D2. TOF was primarily used to distinguish forward scattered events (D1 $\rightarrow$ D2) from backward scattered events (D2$\rightarrow$ D1). Together, TOF and PSD measurements were used to reduce background events. To reject events associated with charged particles, two Cassini-shaped veto domes (plastic scintillators) surrounded each D1 and D2 detectors that acted as charged particle detectors. When the charged particle collided with the plastic scintillator, they continuously interact with the electron of the

scintillator material through Coulomb interaction, causing atomic excitation and ionization track. The rate of energy loss (dE/dx) of charged particle is strongly energy dependent. Each of the four veto domes was viewed by 24 PMTs that produced a pulse when a charged particle interacted with the plastic scintillator (Figure 6). As they travel through the plastic scintillator material, they lose their energy and deposit their remaining energy in D1 or D2 module triggering an anti-coincident event. The signal from veto domes provided a pulse that could be used in coincidence with D1 and D2 signals that reduced charged particle events with an efficiency of 99.9

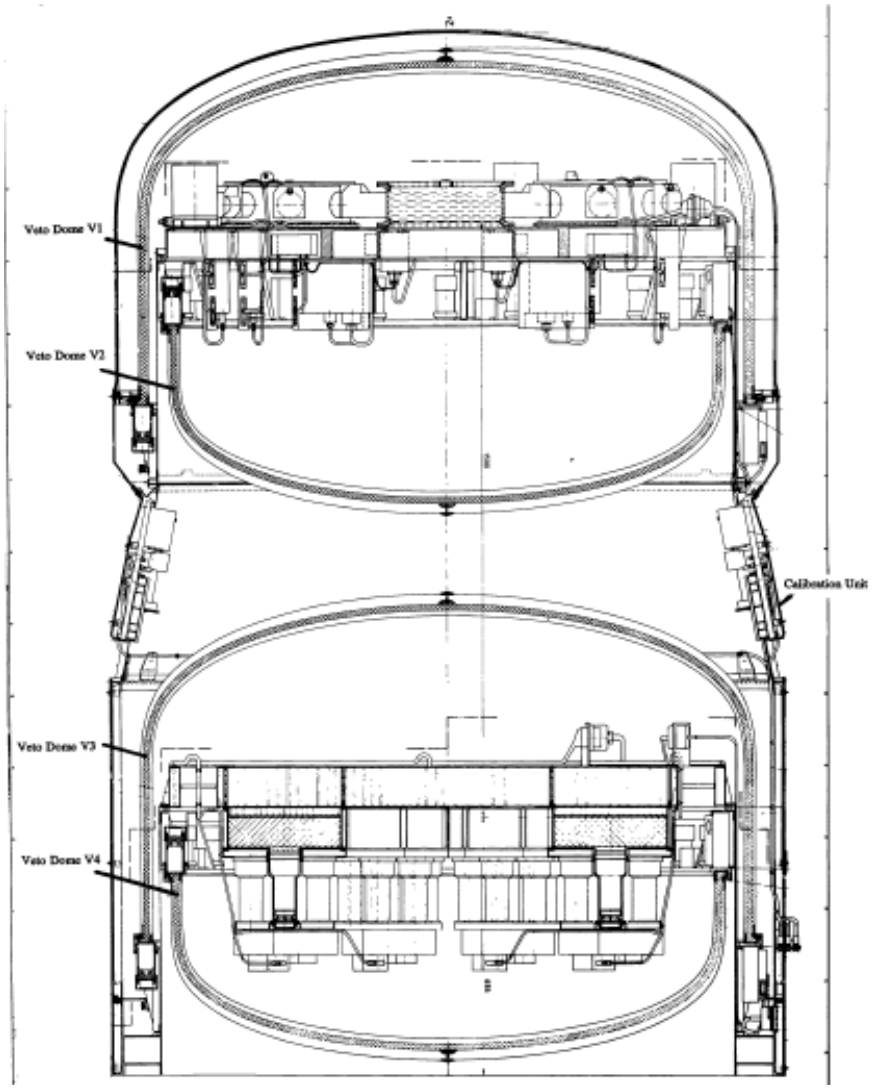

Figure 3.7: The four veto domes are shown that act as a charged particle detector [8].

Also, two ^{60} Co sources doped in plastic scintillators were placed on the sides of COMPTEL, equidistant between the two detector layers (D1 and D2) for an on-orbit calibration of the PMT's. Since each 60Co source emitted two gamma ray photons (with energies 1.17 and 1.33) with an accompanied beta particle, two PMTs surrounded each ^{60}Co source to detect the beta particle with $> 99\%$ efficiency, this providing a coincident signal. A coincidence event between a D1 gamma event and tagging pulse corresponds to CAL-1 event (calibration-1), and an event between D2 gamma event and tagging pulse corresponds to CAL-2 (calibration-2) event. A triple coincidence event is defined by a tagging pulse, CAL-1 event, and CAL-2 event.

3.2 COMPTEL as a Gamma-Ray telescope

In gamma-ray mode, COMPTEL covered the γ ray energy range of 1-30 MeV (Schonfelder et al). As mentioned earlier, an incident γ-ray undergoes Compton scatter in the D1 detector, where photon energy loss is measured in the form of a light pulse using PMTs.

For an ideal event the scattered photon undergoes photoelectric absorption in the D2 layer and deposits its remaining energy (Figure 8). For each measured photon event the recorded parameters include:

1. The photon energy loss (Ee‘) in D1.
2. Photon interaction position in D1 (x,y plane)
3. Pulse shape from the scintillator in D1.
4. Scattered photon energy loss (Ee') in D2
5. Scattered photon interaction location in D2 (x,y plane)
6. TOF of the scattered photon between D1 and D2.
7. The time of the event.

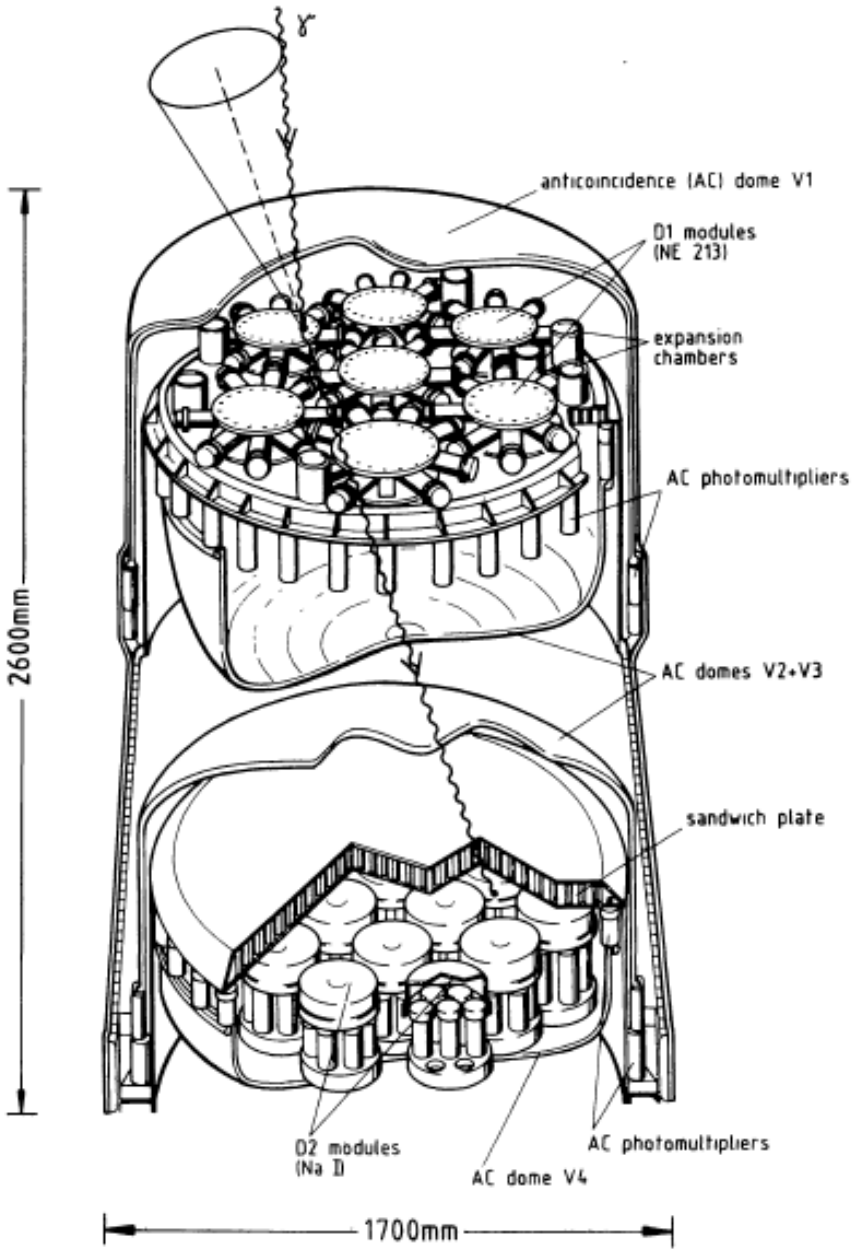

Figure 3.8: The above diagram shows the interaction of incident photon at detector D1 and D2 [8].

The (x,y) coordinates of both interactions (D1 and D2) were measured by using relative pulse height of PMTs. The direction of the incident γ-ray is not uniquely defined. It is constrained to lie on the edge of the cone whose axis is defined by the direction of the scattered γ-ray. The radius of the cone is defined by the edge of the cone and the axis of the

scattered gamma-ray (Figure 8). The measured value is mathematically defined as:

$$cos\bar{\phi} = 1 - \frac{m_e c^2}{E_e\text{‘}} + \frac{m_e c^2}{E_e\text{‘} + E_e\text{“}} \tag{3.1}$$

where $m_e c^2$ is the rest mass energy of the electron (0.511 MeV), and Ee‘ and Ee“ is the photon energy loss measured in the D1 and D2 detectors respectively. If the scattered γ-ray was fully absorbed in the D2 detector, then $\bar{\phi} = \phi$ and $E\bar{\gamma} = E\gamma$. In such case, the locus of the possible directions is an event circle. The location of the celestial source was identified by the superposition of the event circles. If the scattered photon energy was not totally absorbed in D2 detector, then a larger and incorrect event circle was obtained. As a result, the circle would not intersect with the valid event circles at their intersection (Figure 9).

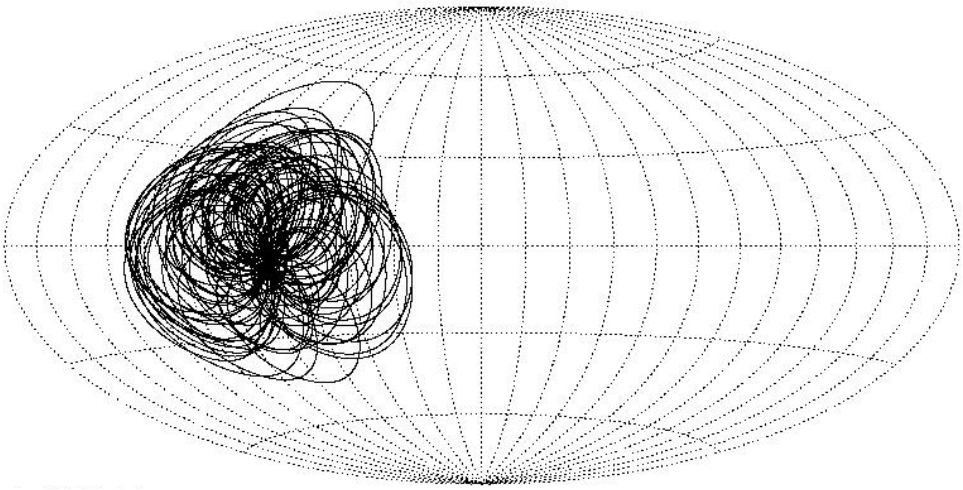

Figure 3.9: The above sketch represented the event circles obtained from the detection of MeV γ-rays from the astrophysical object GRB910503. The intersection of the event circles represented the potential γ-ray source.

3.2.1 COMPTEL as a Neutron telescope

The double scattering process used to detect γ-rays could also measure incident neutrons of energy range 10 – 250 MeV. In an ideal case, an incoming neutron elastically scatters off a proton in a D1 detector and subsequently interacts and deposit its remaining energy in a D2 detector. Much like γ-ray, the energy of the incident neutron could be computed by

summing the recoil energy (E1) of the proton in a D1 detector and the scattered energy (Es) of neutron (deduced from TOF). The pulse shape of recoil protons in the D1 detector was used to eliminate 95% of electron recoil events greater than 1 MeV (neutron energy threshold in D1). The scatter angle for an n-p interaction is given by:

$$tan^2\phi = \frac{E_1}{E_2} \tag{3.2}$$

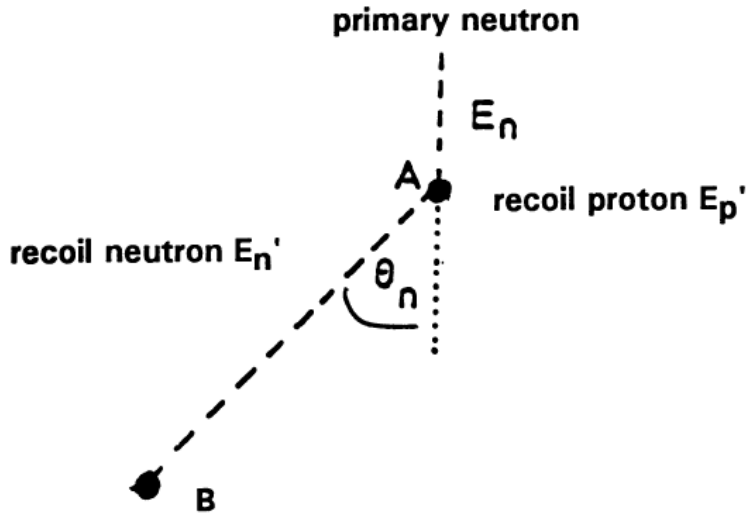

Figure 3.10: The above diagram shows the principle of the neutron measurement in COMPTEL. Point A represents incident neutron collision in D1 module, whereas point B shows recoil neutron collision in D2 module [8].

If a neutron is thermalized in D1, it can be captured by hydrogen nucleus which produces 2D deuterium nucleus with an emission of a single 2.2 MeV photon.

$$n + p \rightarrow np(^2D) + \gamma(2.2MeV) \tag{3.3}$$

The resultant γ-ray undergoes Compton scatter in the D1 detector, and the scattered γ-ray deposits its energy in the D2 detector. This allowed us to use 2.2 MeV γ-ray as a surrogate to albedo neutron flux.

3.2.2 Description of the COMPTEL data

The CGRO average observation time was about 2 weeks per viewing period. During each viewing period the instrument was pointed to a fixed direction in the sky. Also, at each viewing period the COMPTEL lost approximately one-third of the observation time due to occultation of the field of view by the Earth. To study γ-ray events we imposed several event selections that minimized the background events and isolated the γ-ray data from neutron data. Each event is comprised of several event parameters that included position and energy in the D1 detector layer, position, and energy in the D2 detector layer, PSD in D1, TOF and even time. During data analysis we used several event parameters (which also included geophysical and observational parameters) to select specific γ-ray events (See section V). Among all the event parameters TOF plays a vital role to distinguish forward γ-ray events from backward γ-ray events. The typical TOF between D1 and D2 was measured with an accuracy of 0.25 ns. TOF along with PSD could also be used to identify and reject background events from celestial sources. The figure below shows a typical TOF spectrum corresponding to a single D1 and D2 detector module. The forward scattered events (interaction in D1 first) were centered around 120 TOF channel and backward scattered events (interaction in D2 first) were centered around 80. Neutron events (traveling at velocities <c) usually occur above channel 120.

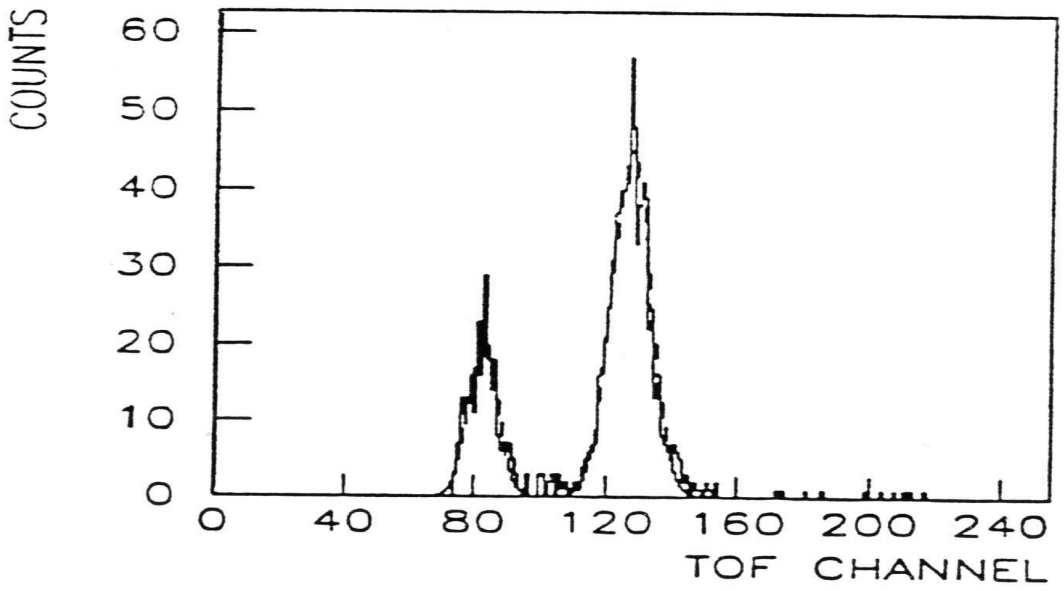

Figure 3.11: Typical TOF spectrum from a COMPTEL flight data. The forward moving photons (D1 $\rightarrow$ D2) typically lies at 120 and backward moving photons (D2 $\rightarrow$ D1) lies at 80. Slow moving neutrons were found at TOF higher than 120. [8].

3.2.3 PSD (Pulse Shape Discrimination)

The pulse shape measurements in the D1 liquid scintillators allowed us to distinguish the γ-ray events from neutron induce events. Figure 12 represents the typical PSD two-dimensional scatter plot. The γ-ray events are found near channel 80, whereas neutron induced events appear in channels above 100.

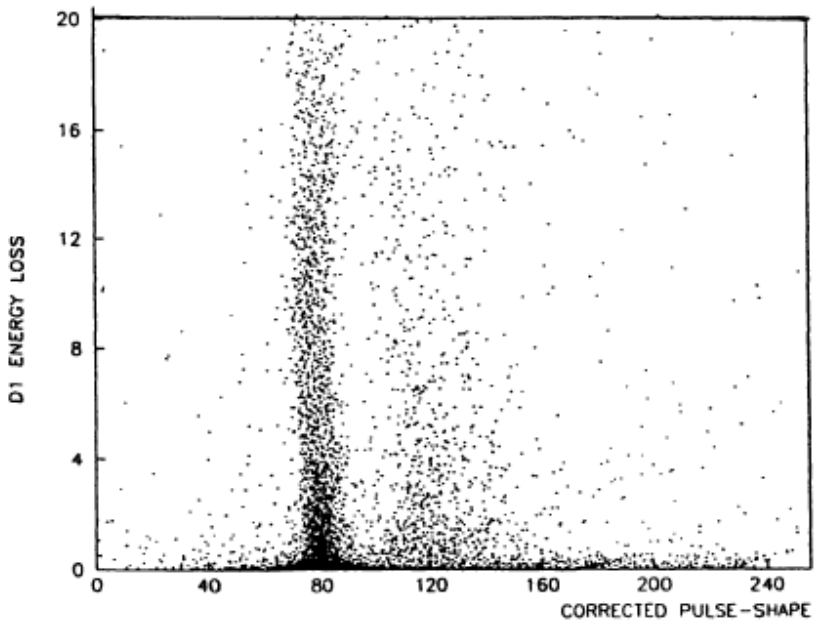

Figure 3.12: The D1 capability of separating γ-ray events from neutron events using pulse shape measurements [8]

3.2.4 Orbital Background

The COMPTEL on-orbit gamma ray spectrum included both astrophysical and background events. Figure 13 below represents the typical γ-ray energy spectrum. The spectrum is dominated by background events with significant line features at 1.46 MeV and 2.2 MeV. The 1.46 MeV line resulted from ^{40}K decay, which was located inside the PMT glass and 2.2 MeV line was caused by incident neutrons being captured by hydrogen atoms in low Z-material of the D1 scintillator. The Data Analysis section (Section IV) explicitly explains other line features occurring due to the instrument activation.

3.2.5 Sources of background

Several background sources like albedo neutrons, albedo gamma-rays, cosmic diffuse gamma ray and GCR interactions constitutes the COMPTEL background energy spectrum. When GCR (protons, electrons, and positrons) interacted with the instrument and surrounding material, it irradiated the instrument and excited the surrounding material. As a result,

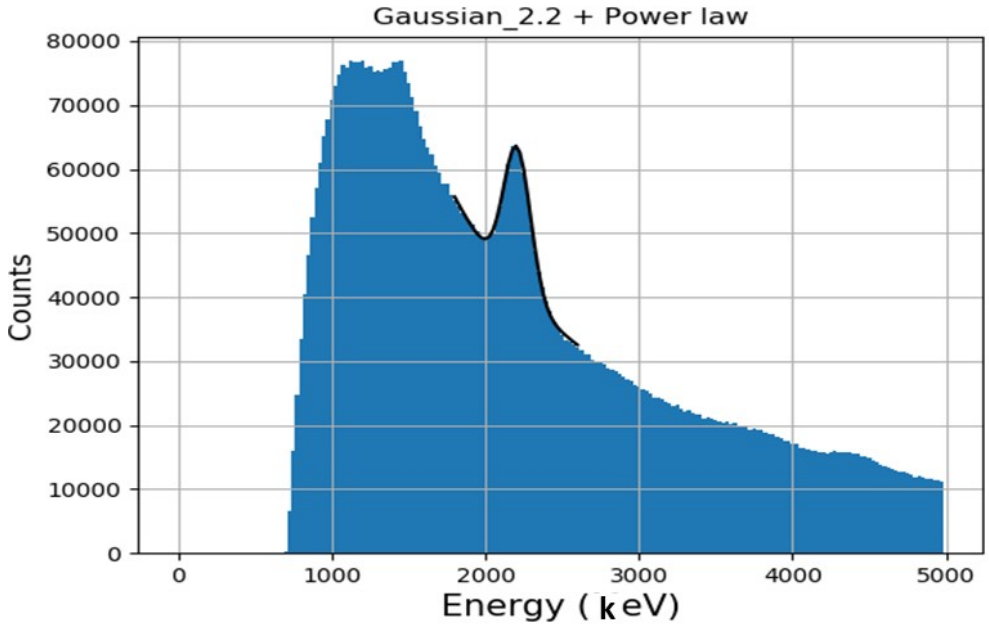

Figure 3.13: Typical COMPTEL γ-ray energy spectrum. The spectrum consists of both astrophysical sources and background events [8].

numerous radioisotopes were formed that induced gamma ray events inside the instrument. These background events populated the COMPTEL energy spectrum at different energies. The Section IV explicitly discusses the activation lines and their respective energies. Another important source of background event is cosmic diffuse gamma ray or DGRB (Diffuse Gamma Ray Background). It is the cumulative emission of astrophysical sources in space. Although, the true composition of the DGRB is still an active area of research, but the well-known astrophysical sources are blazars, misaligned AGNs, star-forming galaxies and millisecond pulsars. They all represent active sources of DGRB [21]. Albedo gamma-ray is another source contributing to the background energy spectrum. These photons primarily result from the interaction of cosmic rays with the Earth's atmosphere. The EGRET satellite provided a suitable dataset for the comprehensive study of albedo gamma rays [18]. Lastly, albedo neutrons play an essential role in constituting the background -ray energy spectrum. As mentioned earlier, they are cosmic-ray induced neutrons of the Earth's atmosphere, which if captured by the hydrogen nucleus produces an internal γ-ray. These γ-rays contribute to

the background and varies as a function of geophysical parameters.

3.2.6 Descriptipn of γ-ray background spectrum

Typical COMPTEL gamma-ray energy spectrum is primarily composed of background and celestial sources. The background sources consist of both internal and external sources. The internal sources are instrument activation lines (interaction of charged particles with the instrument structure), decay of several isotopes (e.g ^{40}K, ^{12}C etc), and neutron capture line (2.2 MeV). Figure 10 below shows several isotopes contributing to background peaks at different energies. The L1 peak corresponds to energy threshold at 70 MeV. The L2 peak corresponds to 40K decay of 1.46 MeV emanating from the PMT tubes, whereas the L3 peak (2.2 MeV) arises due to neutron capture by hydrogen atom in D1 detector. The L4 peak corresponds to neutron capture reaction with ^{27}Al and proton reaction with ^{27}Al giving rise to ^{24}Na, which has a half-life of 14.96 h and undergoes β- decay with 1.37 MeV and 2.75 MeV gamma ray. As mentioned earlier, the external gamma-ray sources are DGRB (Diffuse Gamma Ray Background), SFG (Star Forming Galaxies), and albedo gamma rays to name a few. These external sources also contribute to the background gamma ray energy spectrum. Lastly, L6 (4.4 MeV) is mainly due to de-excitation of excited states in ^{12}C atom found in liquid scintillator.

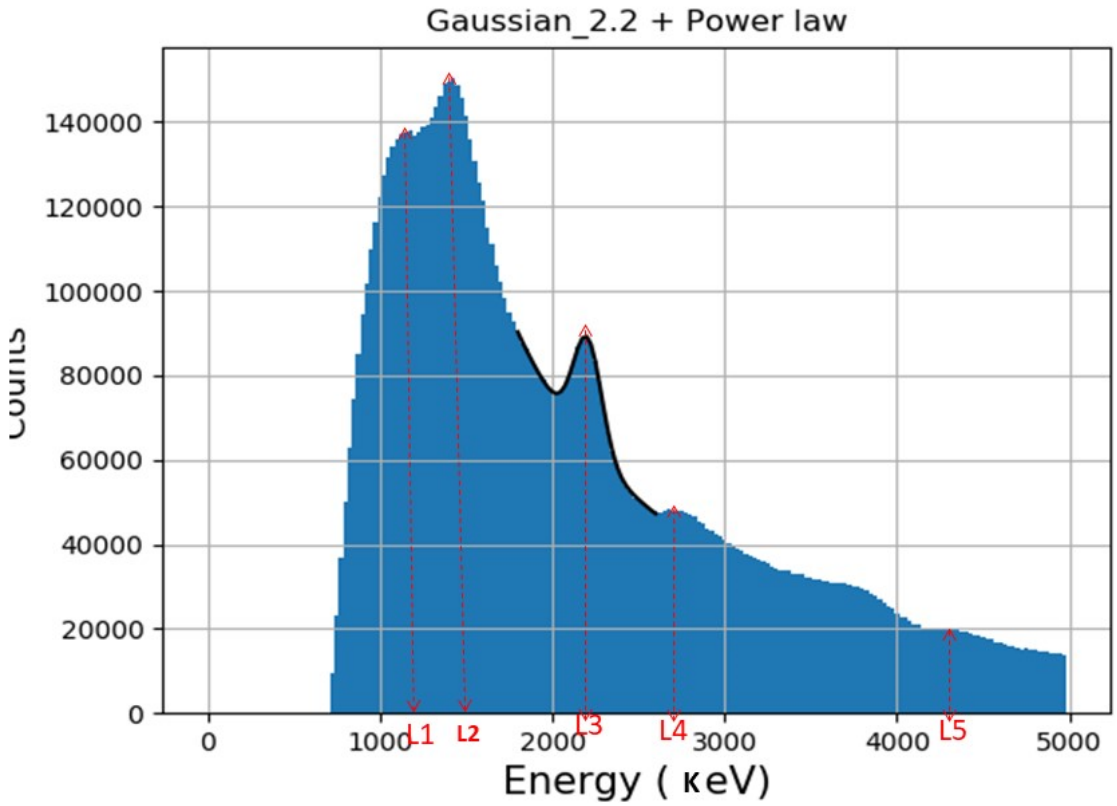

Figure 3.14: Gamma ray spectrum with several highlighted peaks. Each peak corresponds to decay of radioactive isotope. These peaks mainly arise due to instrument activation in response to interaction of cosmic ray particles with the instrument structure.

3.2.7 Simulated COMPTEL (Compton Telescope) Measurements Using MEGAlib.

To characterize the COMPTEL response information to gamma rays, we simulated the COMPTEL D1 detector. Preliminary models were based on Monte Carlo simulations (uses GEANT3 interface) that provided very specific modelling and data analysis tools. This entailed us to use an advanced modelling tool that would allow us to determine detector resolution and energy spectra. The MEGAlib (Medium Energy Gamma-ray Astronomy library) software, is a set of software tools that is specifically designed to model gamma-ray detectors like COMPTEL telescopes. It provides necessary libraries to model detector of different types for example Compton or time of flight based and electron tracking. Using the MEGAlib software, we examined the Compton scattering in the D1 detector.

To obtain simulated measurements of the Compton imaging telescope, we initially generated the mass model data by using one of the MEGAlib software tools called Geomega. It provides an advanced geometry file format that contains necessary detector description for example the volume, density, and composition of detector material. The Geomega library also provided various detector effects (energy position and time resolution) and triggering criteria for detailed response information. The GUI (Graphical User Interface) part is used for visualization of the geometry and its components. The figure below shows the visualization of the COMPTEL instrument along with seven D1 liquid scintillators [22].

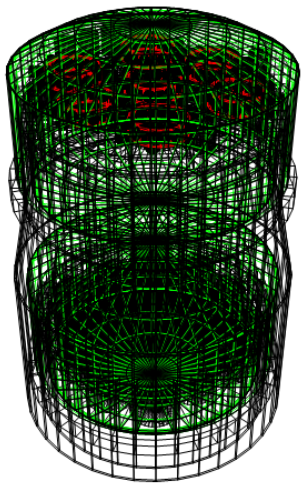

Figure 3.15: The figure above represents the COMPTEL geometry with seven liquid D1 scintillators (red) module using MEGAlib tool Geomega.

The Cosima also known as "cosmic simulator" is another MEGAlib software tool that utilizes the geometry data file from Geomega to perform detail simulations. Using the given source parameters (point source, and energy spectrum), the software outputs a text file that

contained simulated data results. The results are analyzed by using various MEGAlib tools (Mimrec, Sivan and Revan) to display and evaluate the simulated data. Sivan (Simulated Event Analysis) is one of the MEGAlib tool, that utilizes Geomega file and Cosima file (.sim) to interpret ideal interactions. It provides diagnostics for simulation (e.g Compton scatter angles, initial spectra etc.), identify positions of photon interaction with the detector and performed ideal event reconstruction. Figure 2 uses Sivan to simulate photon interaction with the detector in xy coordinate, whereas figure 3 represents spatial hit distribution in xyz.

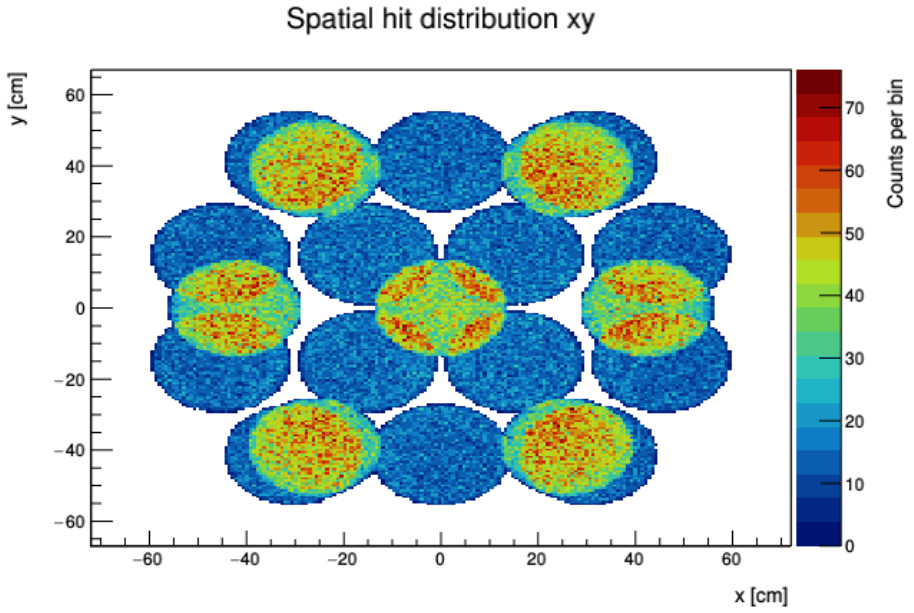

Figure 3.16: The above image represents the spatial hit distribution in x-y plane of 2.2 MeV isotropic gamma ray in D1 and D2 modules.

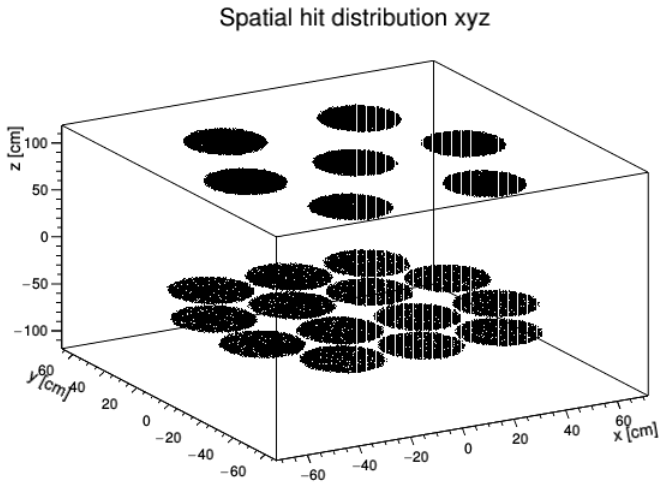

Figure 3.17: This image represents the spatial hit distribution of the 2.2 MeV gamma ray inside the instrument in xyz plane. D1 consists of seven modules and D2 consists of fourteen modules.

3.2.8 Simulated COMPTEL Scatter angle distribution

By utilizing one of the MEGAlib software tools, we simulated COMPTEL scatter angle distribution. The figure 19 below shows simulated Compton scatter angle distribution from 0^o - 180^o for an energy range of 0 to 2.2 MeV. The mean scatter angle is located at 33^o. Figure 20 shows COMPTEL phi-bar distribution with a mean located at 25^o. To optimize the signal to noise ratio, we specifically used phi-bar event selection ranging from 0^o – 50^o. Both simulated and measured plots, show a similar phi-bar distribution pattern, while the simulated plot represents concise distribution up to 180^o.

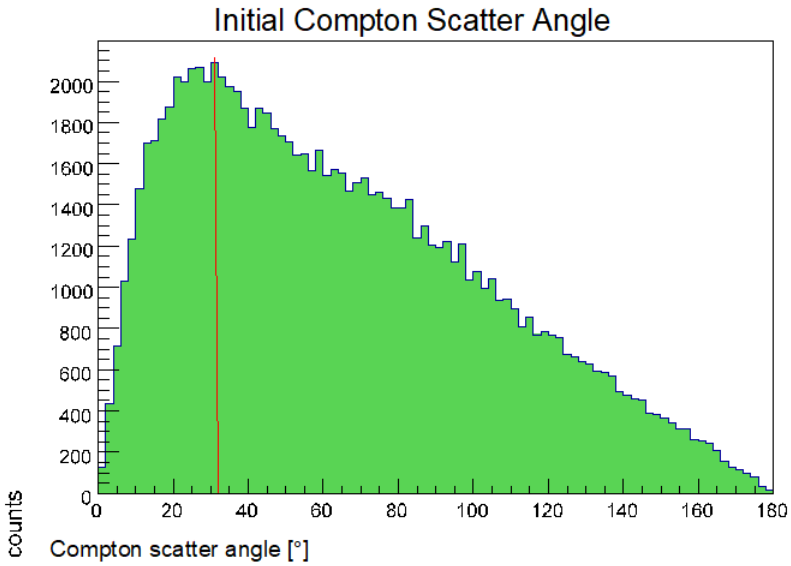

Figure 3.18: MEGAlib simulated Compton scatter angle for energy range 0-2.2 MeV. The simulation scatter angle ranges from 0^o-180^o with a mean located at 33^o

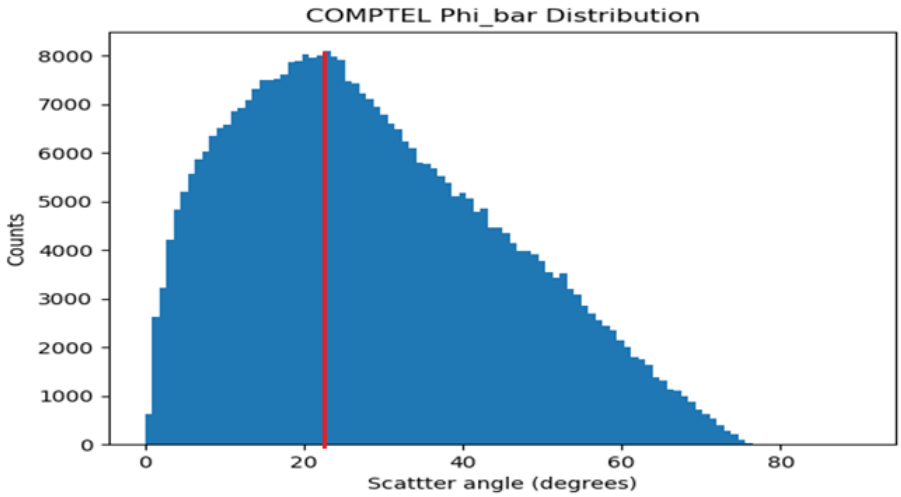

Figure 3.19: The above plot represents measured $\bar{\phi}$ distribution with a mean located at 25^o.

CHAPTER 4

Data Analysis

Albedo neutrons play an essential role in populating the Van Allen radiation belts. A better understanding of the radiation belts requires a detailed analysis of the albedo neutron flux. Thus, it is necessary to study the characteristics of the neutron flux itself as a function of various parameters. The COMPTEL instrument could measure the neutron flux in two ways. Firstly, it could measure the flux directly using its neutron imaging mode. Secondly, it could use the gamma-ray mode to measure the 2.2 MeV neutron capture line as a surrogate for the neutron flux. Since the neutron telescope mode was used sporadically throughout the CGRO mission, we opted to use the 2.2 MeV background line as a surrogate to study the variation of the neutron flux over a wide range of time and orbital parameters.

4.1 Parameters Influencing Local Neutron Flux

Since the COMPTEL 2.2 MeV line is directly related to the local neutron flux, it is expected to vary as a function of time (due to the solar cycle) and as a function of geomagnetic and observational parameters. In this section, we describe the parameters that were used to study the flux.

4.1.1 Altitude

During the CGRO mission, the altitude of COMPTEL varied over a wide range, from about 325 km to 525 km. As a result of orbital decay, the CGRO spacecraft was boosted to higher altitudes on three separate occasions. Figure 4.1 shows the altitude distribution of

the mission, as measured in terms of the number of Orbital Aspect Data (OAD) packets. Each data packet represents 16 to 32 seconds of time. Altitude variations influenced the albedo neutron flux reaching the telescope. For instance, at higher altitudes the spacecraft was further away from the source of neutrons in the atmosphere, and a lower neutron flux is expected to result from the inverse square law. For our analysis, we consider three different altitude intervals: 325-425 km, 425-475 km, and 475-525 km (G. Weidenspointner et al 2001). These are shown in Figure 4.1

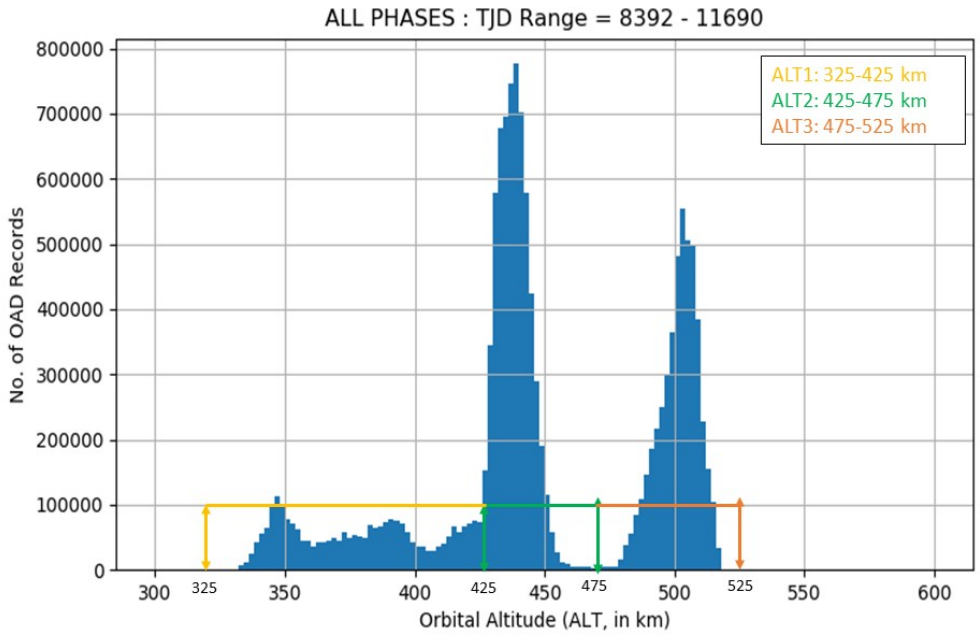

Figure 4.1: Typical flight data of the CGRO instrument shows three different altitude ranges of the instrument.

4.1.2 Geomagnetic Rigidity

The geomagnetic rigidity determines the momentum threshold that a cosmic ray charge particle must possess to reach a given location. This factor modulates the production of ambient neutron flux at the Earth's atmosphere, which affects the 2.2 MeV counting rate inside the spacecraft. A higher rigidity implies lower cosmic ray flux, which leads to a lower neutron flux. Thus, we expect geomagnetic rigidity to have a significant influence on the

neutron flux and the associated 2.2 MeV counting rate. For each altitude ranges given above, the 2.2 MeV rate is estimated at various rigidity, typically ranging from 4-16 GV.

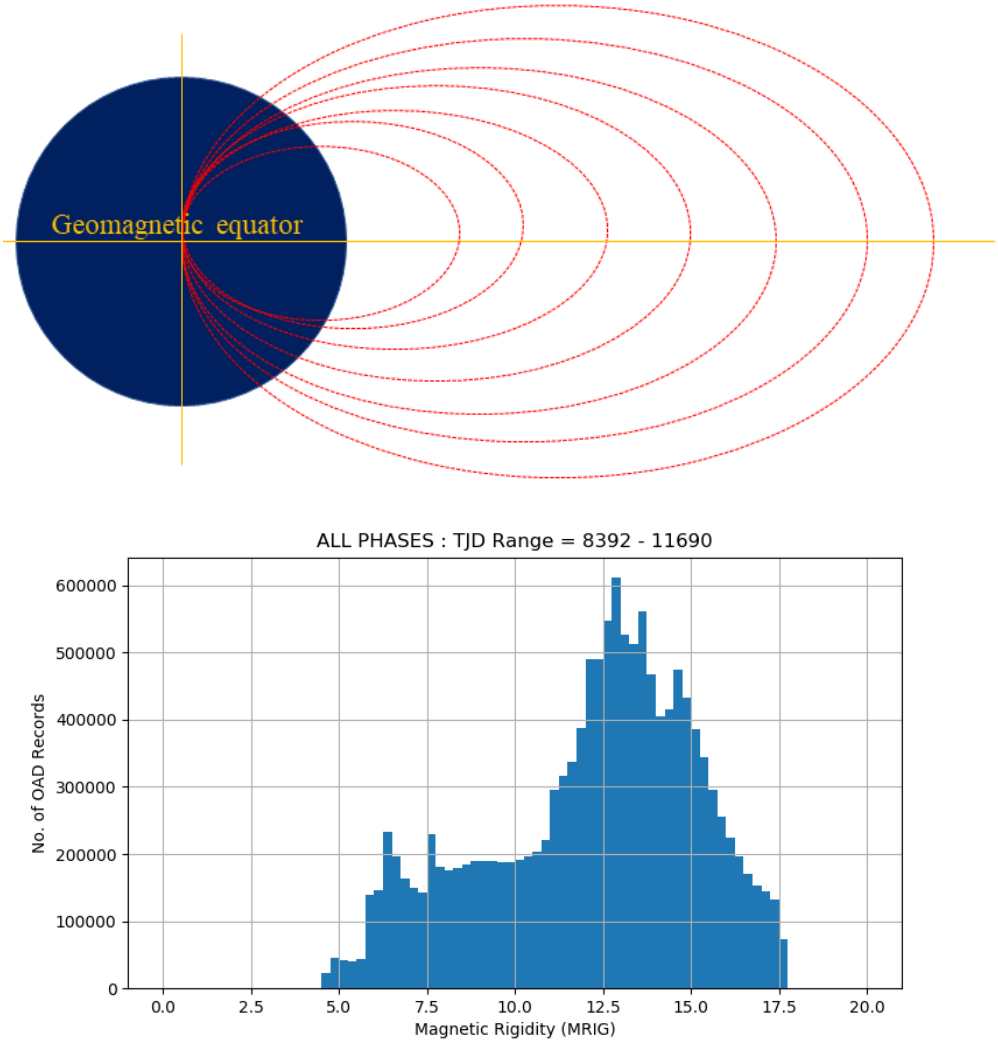

Figure 4.2: The top figure represents the geomagnetic field of the Earth at different latitudes. The field strength is higher near the magnetic equator. The bottom figure represents the magnetic rigidity distribution recorded by the CGRO mission.

4.1.3 Geomagnetic Elevation

The geocentric elevation angle is another attenuating factor that impacts the 2.2 MeV line intensity but imposes less impact than magnetic rigidity. It is an angle between the z-axis (pointing direction) of COMPTEL and the direction to the center of the Earth. Neutrons

entering the Omni-directional D1 detector from all directions will generate 2.2 MeV line radiation. However, the large spacecraft mass underneath COMPTEL attenuates the neutron flux when it is pointed away from the Earth. Therefore, the D1 detectors encounter a higher neutron flux when it is pointing towards the atmosphere. Figure 2 illustrates the geocentric elevation angle towards the Earth.

4.1.4 Phase of the Solar Cycle

The galactic cosmic ray flux reaching the Earth is modulated by the solar magnetic field, which varies throughout the 11-year solar cycle. At solar maximum, the Sun reaches its maximum field strength and tends to exclude galactic cosmic rays from the inner solar system. Since this reduces the cosmic ray flux striking the Earth's atmosphere, we expect that the atmospheric neutron flux will reach its peak at solar minimum. Figure 4.3 shows the variation in sunspot number, which defines the level of magnetic activity on the Sun. Note that the CGRO mission spans a range in time from solar maximum (1991) to a solar minimum (2000).

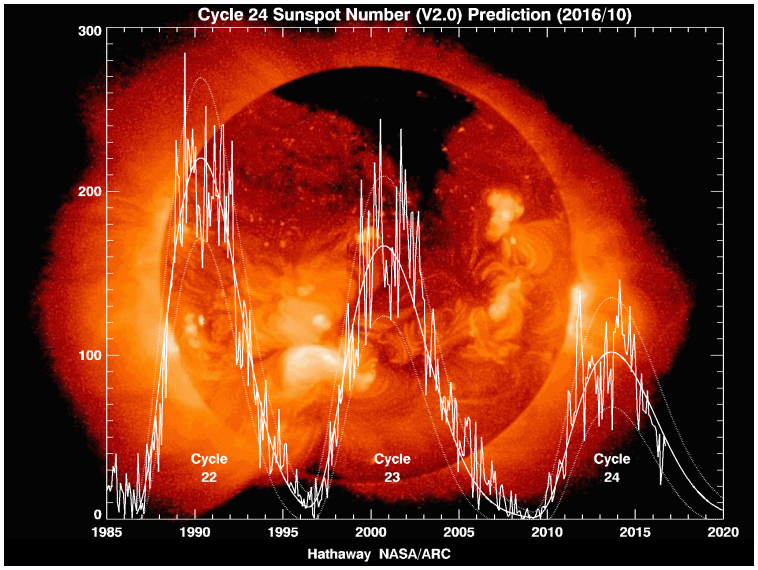

Figure 4.3: The solar cycle is defined by the variation in observed sunspot number.

4.2 COMPTEL Event Selections

During the analysis, selection criteria for COMPTEL events are imposed to select gamma-ray events that are consistent with 2.2 MeV capture line and to reject events that corresponds to other radiation sources, both internal and external. This maximizes the signal-to-noise of the 2.2 MeV measurement. The event selections include: (a) the Compton scatter angle; (b) the Time of Flight (TOF); and (c) the Pulse Shape Discrimination (PSD). Additional selections are made on D1 and D2 energy deposits.

4.2.1 Compton Scatter Angle

The Compton scatter angle ($\bar{\phi}$) distribution, which is determined from the D1 and D2 energy deposits, is heavily influenced by the location of the photon source. For sources external to the instrument (e.g. the Sun), the measured Compton scatter angles tend to be smaller and limited in their distribution due to the detector geometry. An internal source, such as 2.2 MeV photons generated by neutron capture in the D1, will have a very different distribution. In principle, we can define our selection on a scatter angle to distinguish between internal and external radiation sources. In practice, this is difficult to achieve because the distributions cannot be clearly distinguished from one another. In our analysis, we implemented a phi-bar $\bar{\phi}$ selection range of $0^o < \bar{\phi} < 50^o$

4.2.2 TOF (Time of Flight)

The TOF represents a measurement of the time interval between the interaction in D1 and D2. For COMPTEL, the neutron energy range of interest is approximately 10-200 MeV. At these energies, neutrons are non-relativistic and travel slower than the speed of light. The distance photons and neutrons travel between D1 and D2 is significant enough to be measured. Measurements of the TOF can therefore be used to distinguish gamma rays from neutrons. In our analysis, we focus on photon events, therefore we select a TOF range that

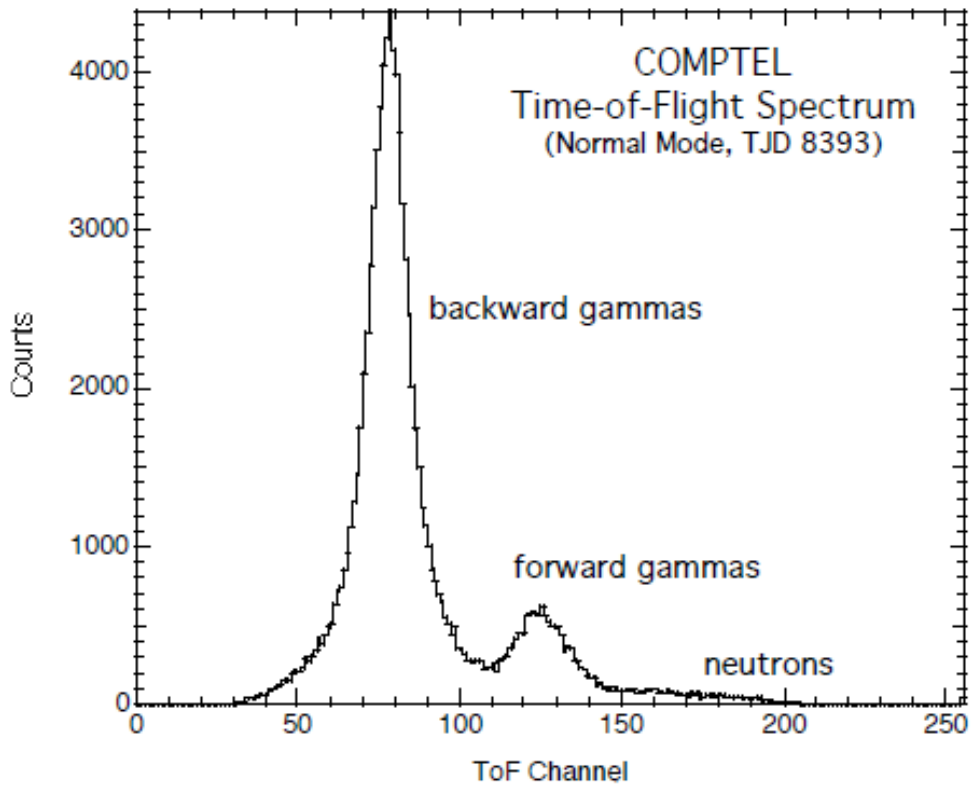

Figure 4.4: The above plot illustrates a typical TOF spectrum. The neutrons lie at higher TOF values due to their slow-moving nature.

is consistent with photons. We used a TOF ranging from channel 115 to channel 130. It corresponds to the time interval between +3.75 ns to + 7.5 ns. Figure 4.5 shows a typical TOF spectrum that includes a backward gamma peak (photons traveling from D2 to D1), a forward gamma peak (photons traveling from D1 to D2), and a neutron distribution (slower-moving particles traveling from D1 to D2).

4.2.3 PSD (Pulse Shape Discrimination)

The PSD is another event parameter that allows us to distinguish between a photon and neutron scatter events. This capability is a feature of the D1 liquid scintillator. Using the PMT (Photo Multiplier Tube) the shape of the scintillation light pulse in the D1 detector is measured to discriminate between two pulses. The light pulse from recoil electrons resulting from Compton scattering and light pulse from recoil protons resulting from neutron scat-

tering are measurably different, allowing us to discriminate between the two types of events (Weidenspointerner et al 1993). Ionization from recoiling protons produces a slower pulse in the D1 electronics. The figure 4.5 show a typical PSD distribution. The PSD distribution is mostly dominated by photon scatter events, relative to neutron scatter events. To obtain photon scatter events, we selected PSD values ranging from channel 0 to channel 110. This specific event selection differentiates between the events caused by photons and neutrons. Taken together the combination of TOF and PSD selections increase our ability to extract the 2.2 MeV line signal from the underlying continuum background.

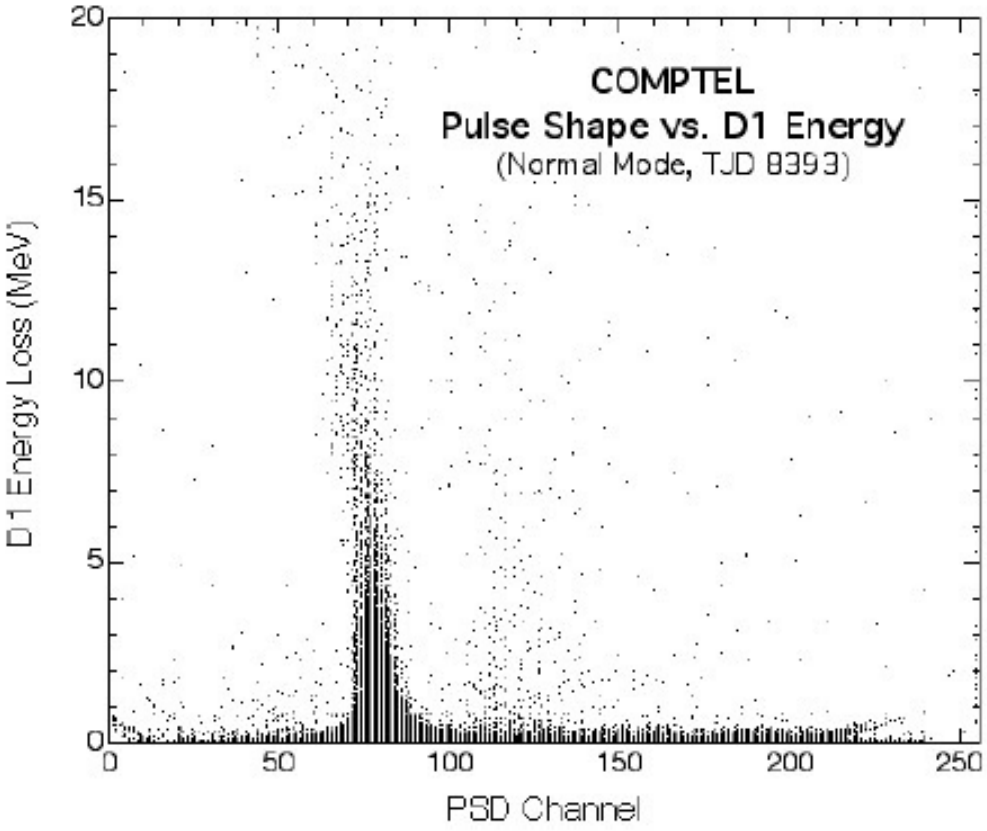

Figure 4.5: The plot shows D1 energy loss versus PSD that could be used to separate neutrons from photons. The electron scatter event from an incident photon centers between PSD values of 50 and 100 and proton scatter event from incident neutron centers between 100 to 150 [Schonfedler et al. 1993].

4.3 2.2/1.46 MeV Line Ratio Studies

COMPTEL was operated in an intense radiation environment. The instrumental background consists of both discrete lines and continuum. By fitting both discrete lines and continuum we can extract the 1.46 MeV and 2.2 MeV line intensities needed to meet the science objectives of the mission. As mentioned earlier, the local radiation environment consists of cosmic diffuse gamma rays, GCR (Galactic Cosmic Rays), atmospheric protons and electrons, and albedo gamma-rays. The photons and neutrons interact with the instrument and surrounding material, whereas the charged particles irradiate the surrounding material only generating secondary photons and neutrons that could contribute to the instrumental line background. Thus, it is prudent to understand the nature of the background. The incident neutrons that are captured on hydrogen in the D1 scintillator produce a deuterium nucleus called deuteron 2D with an emission of a single 2.2 MeV photon. To be captured by a hydrogen nucleus, the neutron must be slowed down to thermal energies. It does so by multiple scattering within the D1 detector, which is then followed by a neutron capture. The average thermalization time of 10-200 MeV neutrons in the D1 detector is around a few microseconds. Once reaching thermal energies the absorption time is about 3x10-4 s, making the 2.2 MeV line a quasi-prompt background line (Weidenspointer et al 2001). To measure the variations of 2.2 MeV line intensity, we initially considered the ratio of the 2.2/1.46 MeV lines. The emission of a 1.46 MeV photon results from an electron capture decay by 40K, which is found in the glass of the photomultiplier tubes (PMTs) (Van Dijk et al. 1996). Usually, the proton-rich nucleus captures an electron from the nearest shell (K-shell), which results in a production of a neutron (proton and electron) accompanied by an emission of a neutrino. As a result, the excited nucleus decays and emits a 1.46 MeV gamma-ray photon.

$$^{40}K_{19} + e^{-} \rightarrow ^{40} Ar_{18} + \gamma(1.46MeV) \tag{4.1}$$

The resultant 1.46 MeV gamma-ray can Compton scatter with an electron in the D1

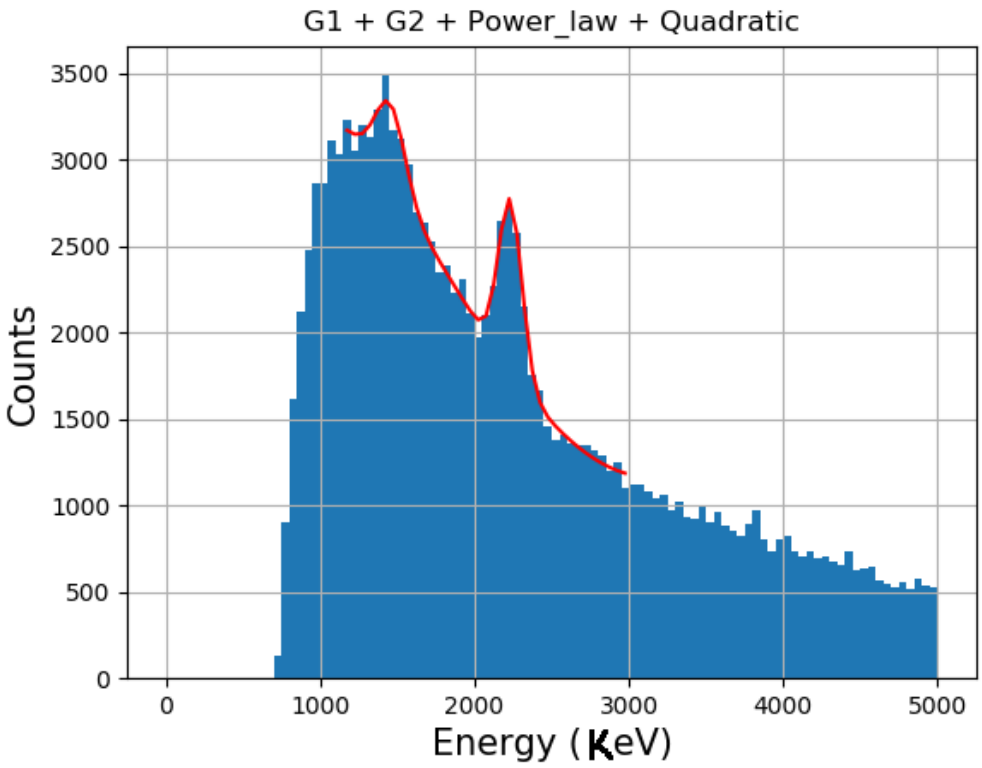

Figure 4.6: The total energy spectrum of COMPTEL. It features the 1.46 MeV and 2.2 MeV lines along with continuum background.

detector and deposit its remaining energy at D2 with similar pulse shape and time of flight as an external gamma-ray. 40K has a half-life of 1.28*109 years. Since it has a long half-life, the production rate of the 1.46 MeV background can be considered constant throughout the CGRO mission. It can therefore be useful as a stable reference in examining the relative intensity variations of the 2.2 MeV line.

Figure 4.6 shows total energy spectrum that is composed of instrumental line background and continuum background. The curve fit (black line) includes the continuum and two instrumental lines to determine the total counts in the 1.46 MeV to 2.2 MeV lines. From previous research (e.g Morris et al 1995) we expect to see an exponential decrease of the 2.2 line ratio as a function of geomagnetic rigidity. Figure 4.7 represents line ratio as a function of geomagnetic rigidity for each phase of the CGRO mission. The data shows the same exponential behavior as seen previously.

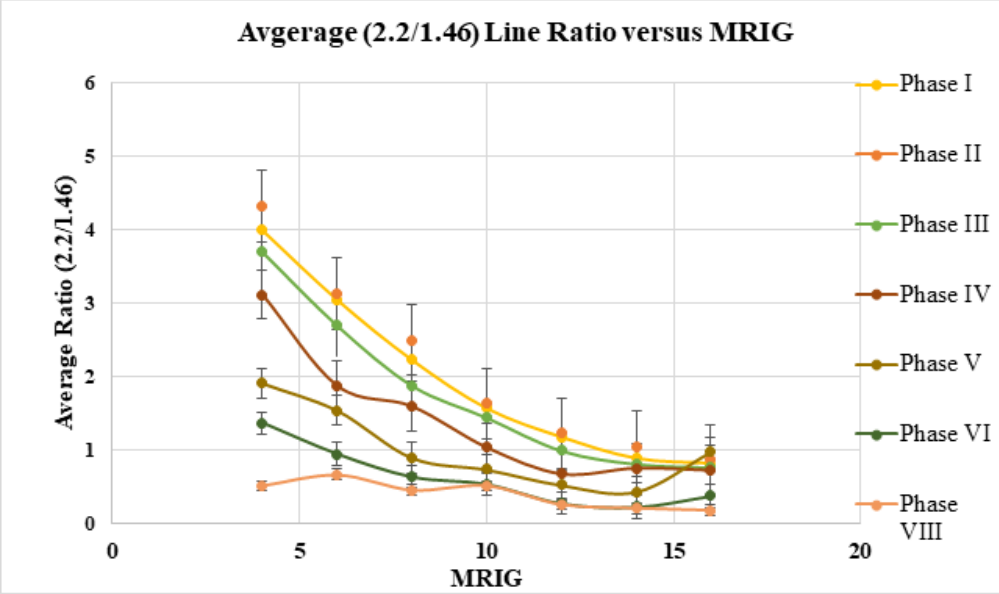

Figure 4.7: The plot illustrates line ratio as a function of rigidity and altitude. At ALT1, the COMPTEL experienced solar maximum and at ALT 2 and ALT 3 it went through solar minimum.

To investigate the relationship of the albedo neutrons with respect to altitude we divided the data into three altitude ranges (See figure 4.1). We expect a higher neutron flux at lower altitudes because we are closer to the source of neutrons. Figure 4.8 depicts the line ratio as a function of rigidity for the three different altitude intervals. The data show similar exponential behavior as a function of rigidity. The plot also shows a decrease in neutron flux with respect to altitude, as we expected.

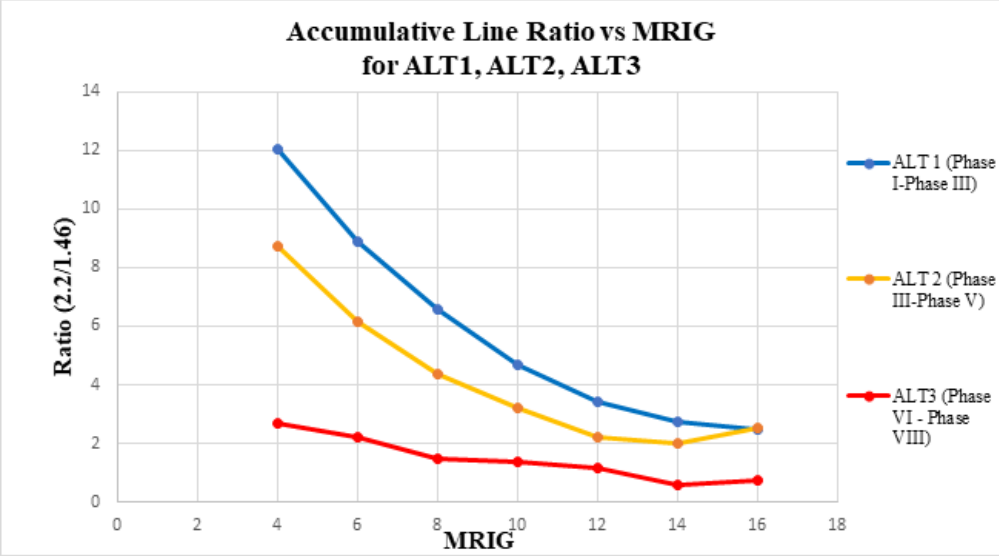

Figure 4.8: The plot illustrates line ratio as a function of rigidity and altitude. At ALT1, the COMPTEL experienced solar maximum and at ALT 2 and ALT 3 it went through solar minimum.

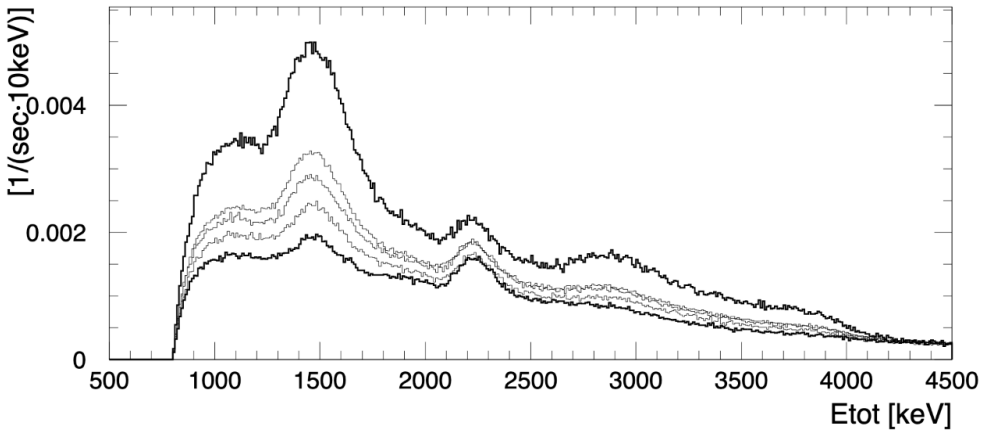

Figure 4.9: The plot shows COMPTEL's total energy spectra of the entire mission. The thick lines represent highest (second re-boost in May 1997) and lowest (first re-boost May 1991 – Nov 1993) contributions from background isotopes. The middle three lines correspond to intermediate mission time [8].

4.3.1 Contamination of the 1.46 MeV background line

Over time the spectral feature attributed to 40K became more intense and appeared to broaden. This can be seen in Fig 4.9. The growth of this feature is attributed to unresolved activation lines in the vicinity of 1.46 MeV. In a research article, Weidenespointner explained

that this growth arises from several activation lines primarily 22Na (1.27 MeV), ^{24}Na (1.37, 2.75), ^{28}Al (1.78 MeV), ^{52}Mn (1.43 MeV) and ^{57}Ni (1.37 MeV), all of which are due to interaction of protons and neutrons with the instrument and surrounding material. The activation and subsequent decay of various isotopes of the COMPTEL instrument onboard the CGRO spacecraft contributed to the total energy spectrum and contaminated the 1.46 MeV line. Since the majority of the D1 structure is composed of 2^7Al, the neutron capture reactions with ^{27}Al produces an unstable 24Na nucleus that decays into $^{23}Mg_{12}$ with an emission of 1.37 MeV and 2.75 MeV gamma-ray. The equation below shows the production and decay of 24Na due to unstable $^{27}Al_{13}$ isotope.

$$^{27}Al_{13} + n \rightarrow^{28} Al_{13}(isotope) \tag{4.2}$$

$$^{28}Al_{13} \rightarrow^{4} He_2 +^{24} Na(\alpha - decay) \tag{4.3}$$

$$^{24}Na \rightarrow^{23} Mg_{12} + \beta^- + \gamma(1.37, 2.75) \tag{4.4}$$

Consequently, the ^{2}4Na line contaminated ^{40}K decay leading to an over-estimate of 1.46 MeV intensity. Similarly, other radioactive isotopes that pronounced the 1.46 MeV feature lines are ^{52}Mn and ^{57}Ni (See figure 4.10). The ^{52}Mn isotope is formed during the CGRO passage over South Atlantic Anomaly (SAA). The SAA radiation consisted of protons that struck Fe, Cr, and Ni found in D1 electronics, producing ^{52}Mn with a half-life of 5.6 days. The ^{52}Mn undergoes Electron Capture (EC) and emits 1.434 MeV line, which blended with a ^{40}K spectral line and ultimately increased the overall intensity of the 1.46 MeV. Similarly, the isotope ^{57}Ni arose due to proton interactions with ^{58}Ni and ^{64}Cu in the D1 structure during the SAA passage. With a half-life of 36 h, the isotope undergoes electron capture and annihilates into β^+ decay emitting 0.511 MeV and 1.37 MeV photons, contributing to ^{40}K emission line. Figure 4.10 shows several prominent peaks that arise due to instrument activation and contaminates the 1.46 MeV line.

Figure 4.10 shows the total energy spectrum. P1 and P2 correspond to the location of

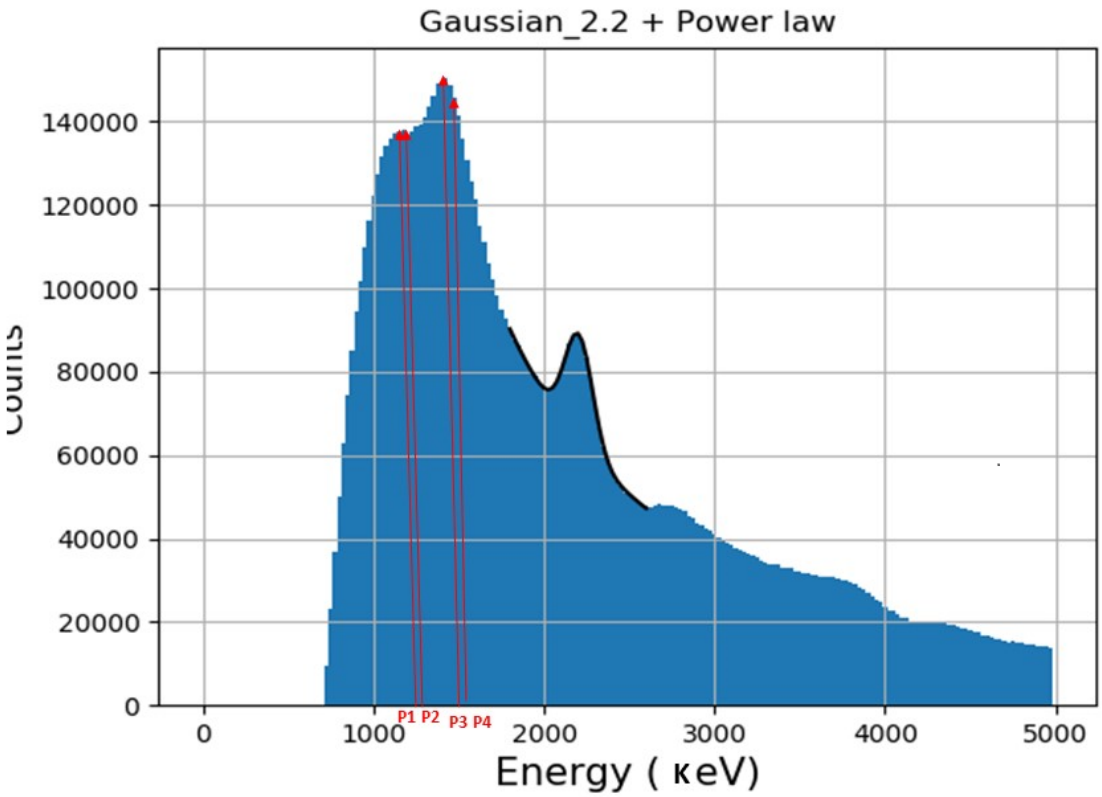

Figure 4.10: The above plot represents several instrumental background lines that are due to activation and or decay of many isotopes inside the instrument.

lines from ^{2}4Na (1.37 MeV) and ^{5}7Ni (1.38 MeV). P3 and P4 correspond to the location of lines from ^{4}0K (1.46 MeV) nucleus, and ^{5}2Mn (1.43 MeV). These lines contributed to 1.46 MeV line feature and consequently the measured line ratio 2.2/1.46, which affected the neutron flux analysis. This required us to seek another approach to measure variation of the neutron flux.

4.3.2 Study of the 2.2 MeV Count Rate

The contamination of 1.46 MeV in the D1 detector undermined the line ratio studies and resultant neutron flux analysis, which entailed us to calculate the 2.2 MeV rates using the absolute live time at three altitudes ranges. For each altitude range, various event selections are implemented (TOF, PSD, Compton scatter angle), including MRIG and ALT, to improve the albedo neutron signal to noise ratio. Figure 4.10 shows the total energy spectrum with

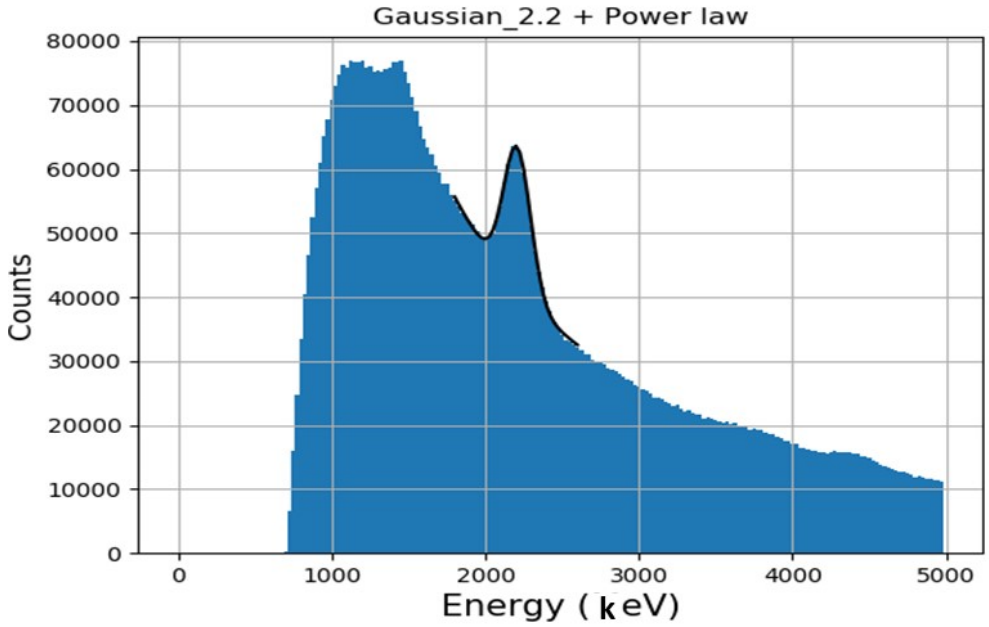

Figure 4.11: The total energy spectrum from COMPTEL's γ-ray mode. The black line represents a 2.2 MeV curve fit.

a curve fit over 2.2 MeV curve.

A new mathematical model is implemented to obtain integrated counts under 2.2 MeV curve fit only. The model consisted of a gaussian function for asymmetric 2.2 MeV peak and a power law to fit the continuum background (equation 4.6).

$$f(x) = G_{2.2}(x) + Pf(x) \tag{4.5}$$

$$G_{2.2}(x) = \frac{A}{\sigma * \sqrt{2\pi}} e^{\frac{-(x-\mu)^2}{2\sigma^2}} \tag{4.6}$$

$$P_f(x) = a * x^b \tag{4.7}$$

We tested the model on various total energy spectra that included data from several viewing periods. The model showed an agreement between our analytical observations and previous researches. We concluded that the spectrum does not depend highly on the geo-

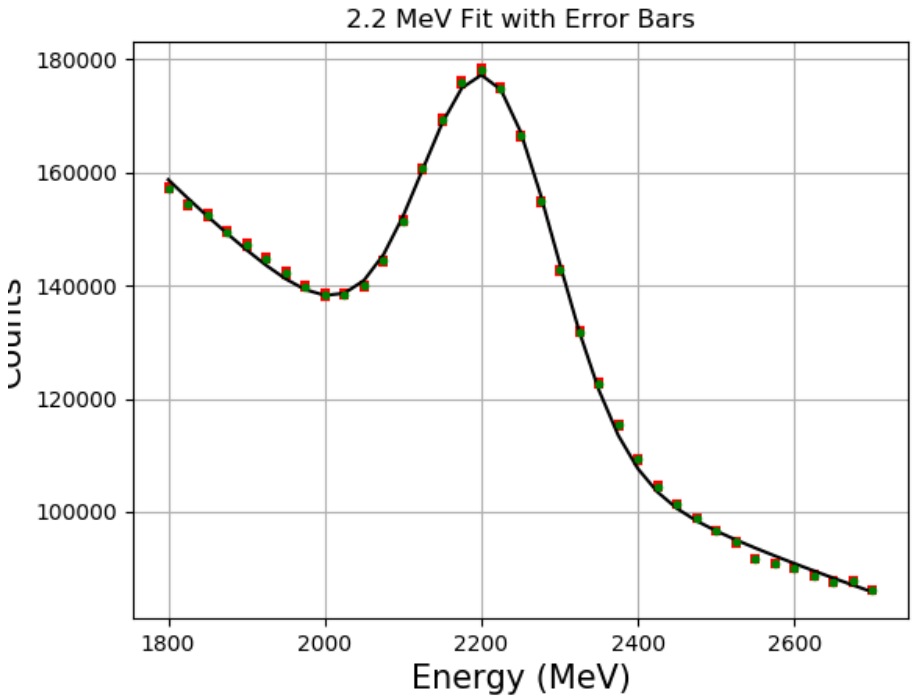

Figure 4.12: Asymmetric Gaussian fit fitted against each data point along with error bars.

centric elevation relative to the magnetic rigidity of the telescope, and the given model is an adequate description of the data. Figure 4.12 above shows a high statistics spectrum fitted against the analytical model. The tiny deviations of the spectrum from the fit were primarily due to various background lines from the instrument itself, which consequently affected the curve fit statistics and reduced X^2 value. Therefore, a high statistical model may not represent a perfect model but provides an essential description of the spectrum.

4.3.3 Error Analysis of the COMPTEL data

As discussed earlier, the COMPTEL in-flight data constitutes both astrophysical and background sources. The background events populate noise in the gamma ray energy spectrum and cause error in the overall data. To perform error analysis on the 2.2MeV rate for all three altitude ranges, we derived the error propagation formula. The δR represents the uncertainty in 2.2 MeV rate which we wish to find. The R represents the count rate, δP is the

error count, t is the absolute time, and P is the integrated count under 2.2 MeV peak.

$$R_{2.2} = \frac{P_{2.2}}{t} \tag{4.8}$$

$$\frac{\delta R}{R} = \sqrt{((\frac{\delta P}{P})^2 + (\frac{\delta t}{t})^2)} \tag{4.9}$$

$$\delta t = 0 \tag{4.10}$$

$$\delta R = R * (\frac{\delta P}{P}) \tag{4.11}$$

The chapter 5 (Results) shows the 2.2 MeV rate and corresponding error bars for each altitude range.

CHAPTER 5

Results

All orbiting spacecraft are exposed to space radiation that can cause permanent damage to its on board instruments and electronics. The high energy neutron flux is one of the potential radiation candidates that poses great threat to spacecraft electronics. These neutral particles can also interact with the spacecraft structure and activate its material (create radioisotopes). The focus of this chapter is to briefly discuss the effects of neutron radiation on the spacecraft and study the 2.2 MeV rates to examine the neutron flux as a function of geophysical parameters.

5.1 Effects of neutron radiation

As mentioned earlier, the Galactic Cosmic Rays (GCR) collide with the Earth's atmosphere and generate electromagnetic air showers that include positrons, neutrons, electrons, and protons. Some of these particles (e.g. neutrons) move upwards and interact directly with the spacecraft. These neutrons penetrate the electronics of the spacecraft and undergo nuclear collision with the Si substrate, creating charged particles that produces electron-hole pairs. Charge generation near the active region (collector-base junction) of the transistor drifts internal voltages that causes Single Event Effects (SEE) in a semi-conductor device. The SEE includes bit flip error, latch-up error, loss of stored data or cause a permanent damage to the memory. Similarly, neutrons striking with the spacecraft structure (primarily ^{27}Al) activate the instrument and may induce background gamma-ray radiation. These radiations generate background noise in the gamma ray instruments and affects the gamma-

ray observation. Thus, we want to better understand the generation of neutrons by GCR and its impact on the background spectrum. Free neutrons undergo beta decay through weak interaction with a half-life of about 15 mins. The weak interaction converts a down quark to a up quark, changing neutron to a proton. As this happens the neutron decays into proton, electron, and antineutrino. When these neutrons decay within the Van Allen belts they undergo Cosmic Ray Albedo Neutron Decay (CRAND). CRAND is the process that feeds (and maintains) the Van Allen radiation belts. Thus, by studying the 2.2 MeV rates, we can investigate the temporal variation of neutron flux that populate at the near-Earth orbit. In this section we will specifically focus on the 2.2 MeV rates that are used as a surrogate to neutron flux measured over the course of the mission.

5.2 2.2 MeV Rates Result

5.2.1 2.2 MeV rates versus magnetic rigidity

To determine the neutron flux, we initially estimated the 2.2 MeV counting rate as a function of various parameters mainly geomagnetic rigidity and altitude of the spacecraft. Figure 5.1 shows the rates as a function of rigidity for three different altitude ranges. It explicitly illustrates the dependence of line intensity on magnetic rigidity. At higher rigidity, the cosmic ray particles require higher momentum to reach the Earth's atmosphere and produce albedo neutrons. Therefore, we expect to see a lower neutron flux at higher rigidity. We find an exponential fit is a good description of our data (See Figure 5.1 - 5.3). This is consistent with previous studies (Morris et al. and Weidenspointer et al.). Also, we separated the data at three different altitude ranges because we expect lower fluxes at higher altitudes (See Section 5.2.2).

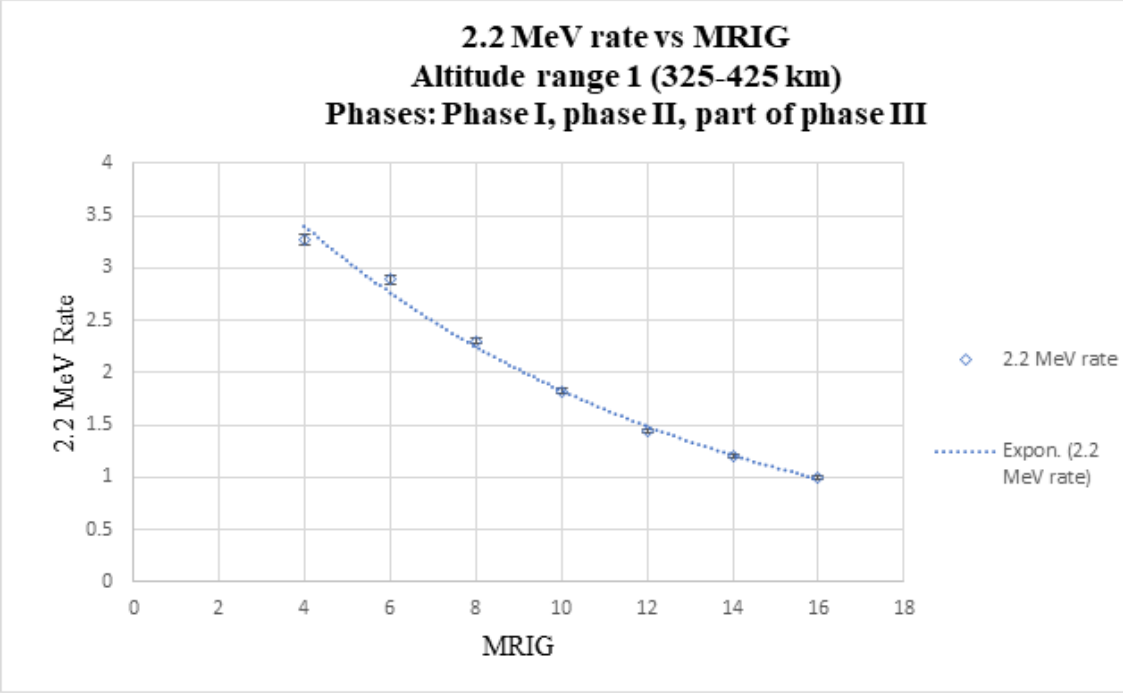

Figure 5.1: The ALT 1 data plotted as a function of rigidity. An exponential fit clearly describes the trend of data.

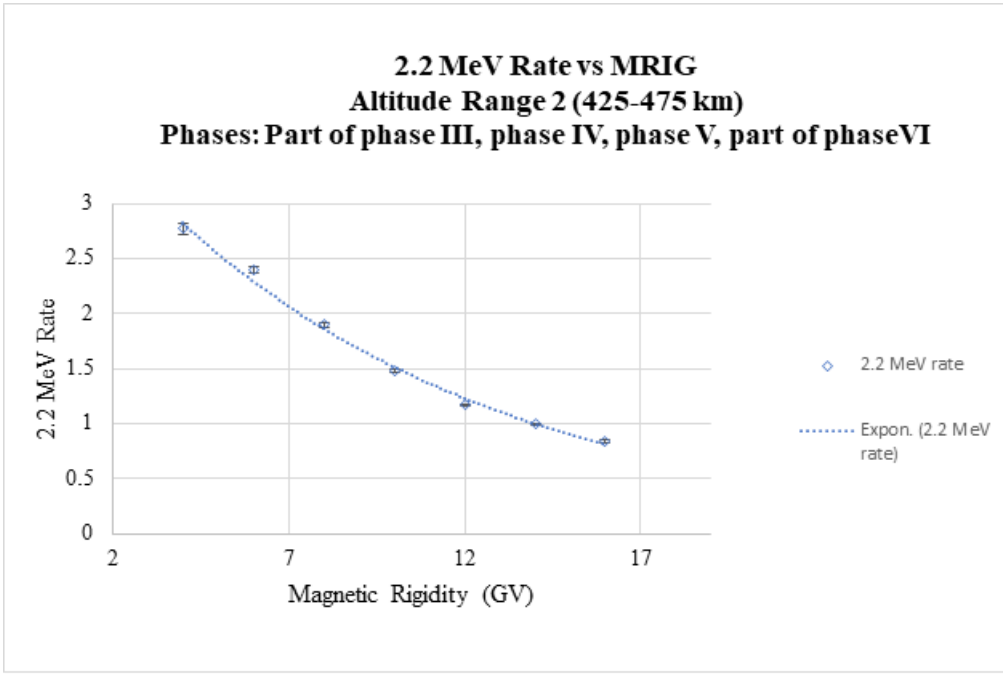

Figure 5.2: The 2D plot show ALT 2 data as a function of rigidity. At higher altitude range we observe a lower neutron flux.

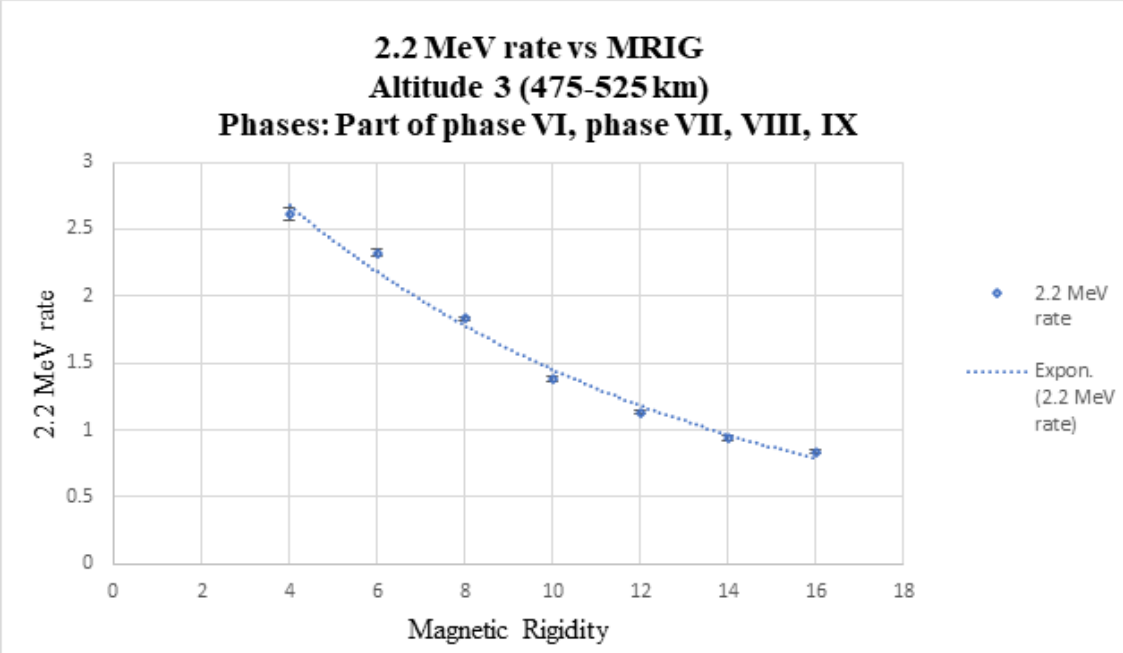

Figure 5.3: The ALT 3 also represents an exponential decrease of 2.2 MeV rate as a function of magnetic rigidity and altitude.

5.2.2 2.2 MeV rates versus altitude

To examine the neutron flux as a function of altitude, we separated the data at three different altitude ranges. At altitude range 1, the spacecraft was closest to the Earth's atmosphere. We expect to see a higher 2.2 MeV rate and consequently an increase in neutron flux. At higher altitude ranges we move away from the neutron source; therefore, the flux should decrease as an inverse square law. Figure 5.4 represents line rates for all three altitude ranges. The plot portrays altitude as a key element impacting the 2.2 MeV rates.

5.2.3 2.2 MeV rates versus Time (phase of the Solar cycle)

To estimate the rates as a function of time, we plotted altitude range 2 as a function of time and rigidity. We expect to see a lower neutron flux at solar maximum. During solar maximum, the Sun has maximum number of sunspots near the equator. The turbulent motions on the Sun tear apart sunspots in the form of CME (Coronal Mass Ejections). The stream of charged particles also called solar wind stretches out the IMF (Interplanetary

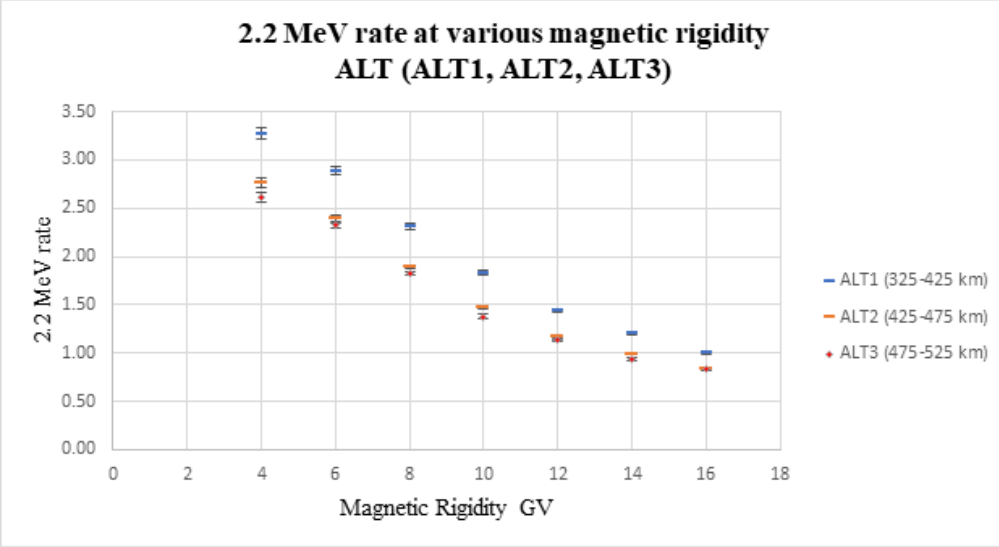

Figure 5.4: The 2.2 MeV rates at three altitude ranges.

Magnetic Field) and fills the solar system. The IMF impacts the penetration threshold of GCR flux that consequently undermines the production of albedo neutrons. Figure 5.5 represents altitude range 2 at three different time intervals. The ALT 4A has lower rates relative to 4B and 4C. From previous observations it has been noted that solar cycle is anti-correlated to the GCR flux. This could be clearly seen in figure 5.5. The ALT 4B and ALT 4C shows an increase in 2.2 MeV rates due to high albedo neutron flux at solar minimum. It shows that solar modulation also plays an essential role in moderating the neutron flux intensity.

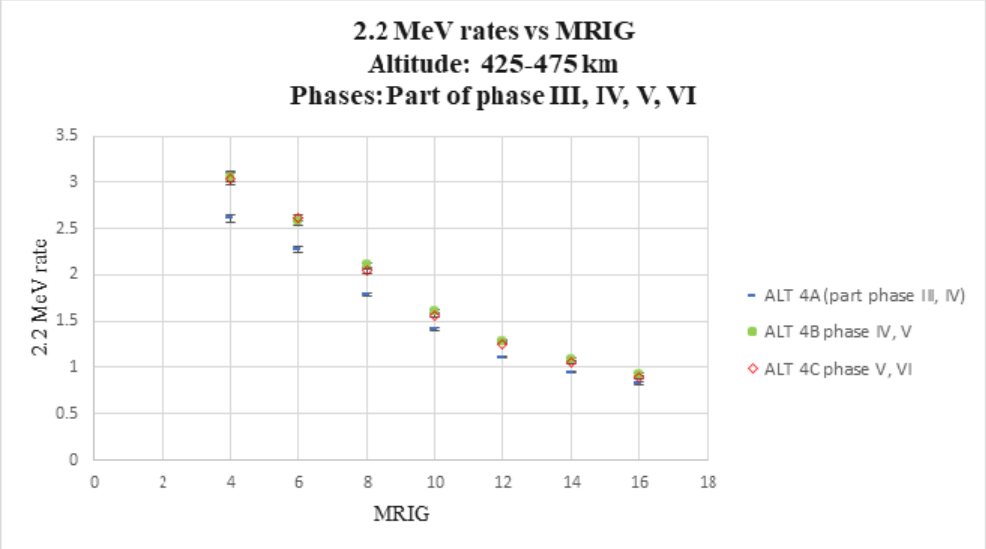

Figure 5.5: The above plot represents the temporal variation of 2.2 MeV rates for altitude range 2 as a function of rigidity.

In addition, we generated heat maps of two different phases to analyze solar modulation. The heat maps were generated at a fixed altitude range $425 < \text{ALT} < 445$ km and magnetic rigidity range 4-19 GV. There is a increase of flux at solar minimum relative to solar maximum (See figure 5.6). The heat maps show an inverse relationship between count rates and magnetic rigidity. The geomagnetic rigidity cutoff act as a momentum analyzer for incoming cosmic rays that impacts the production of albedo neutrons. At higher rigidity we expect to see a lower neutron flux and at lower rigidity (near the Earth's equator) we expect to see a higher neutron flux. In addition, the solar activity is another important factor that modulates the cosmic rays and consequently the production of albedo neutrons. The figure 5.6 shows that both attenuating factors (rigidity, and solar modulation) affect the production of 2.2 MeV rates as expected.

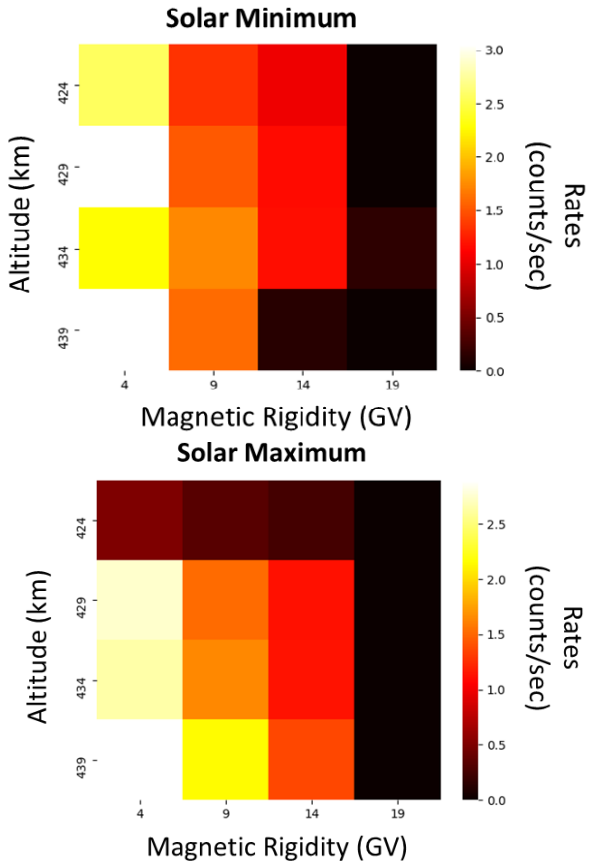

Figure 5.6: The above figure shows heat maps generated at two different phases as a function of altitude and geomagnetic rigidity. The heat maps signify solar modulation at two different phases (phase V and phase VI)

5.3 Neutron Measurements in near-Earth orbit with COMPTEL

In a research paper, Morris et al. (1995) summarized the COMPTEL measurements (1991) of fast neutron flux in a LEO (Low Earth Orbit). By using one of the D1 cells, the measurements cover vertical cutoff rigidity range of 4.8 to 15.5 GV and 3^o to 177^o spacecraft geocentric zenith angle. Using the mathematical formula, Morris et al. fitted the neutron event rate (energy $\geq$ 8 MeVee) as a function of geomagnetic rigidity, zenith angle, solar modulation (neutron monitor rate). To evaluate the COMPTEL neutron fit, Morris et al. compared it with previous balloon experiments like Ait Oumer et al. (1988) Kanbach et al. (1974) and Preszler et al. (1976). The formula used to fit the COMPTEL neutron event is:

$$R_{D1}(P_c, \theta, R_{nm}) = 1.67M(R_{nm}(1 - b\theta)e^{-\alpha P_c}Hz \tag{5.1}$$

where R_{nm} is the rate of ground level neutron monitor.

5.3.1 Estimated Neutron Flux

Using eq (5.1) Morris et al. estimated the neutron flux as a function of rigidity, zenith angle, R_{nm} and neutron energy. Incorporating the two limiting hardness ratios ranging from -1.36 - 1.48 the formula becomes:

$$\phi(P_c, \theta, R_{nm}, E_n) = 0.45M(R_{nm}(1 - b\theta)e^{-\alpha P_c}E_n^{-1.36}cm^{-2}s^{-1}MeV^{-1} \tag{5.2}$$

$$\phi(P_c, \theta, R_{nm}, E_n) = 0.82M(R_{nm}(1 - b\theta)e^{-\alpha P_c}E_n^{-1.48}cm^{-2}s^{-1}MeV^{-1} \tag{5.3}$$

where R_{nm} is normalized to 1.

The two neutron fits were compared with Ait Oumer et al. balloon measurements (See figure 5.6). Both fits were consistent with the data provided by Ait Oumer et al. Note that the neutron flux at the CGRO altitude of 450 km was estimated from the data of Ait Ouamer et al. by integrating over values for altitude 4.1 g/cm^2 (See Ait Ouamer et al Table 3).

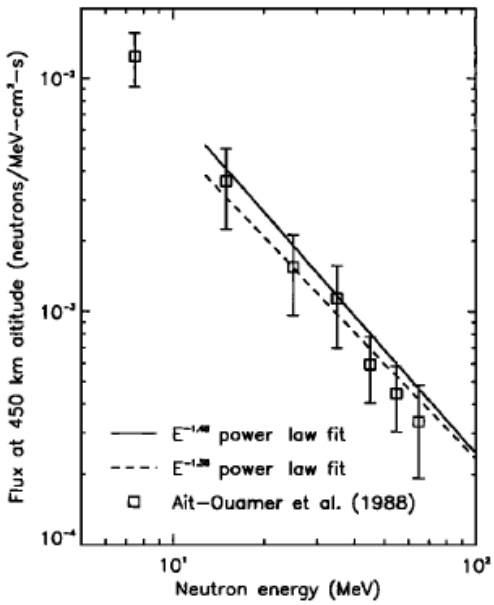

Figure 5.7: The above formula fits the orbital neutron flux for two extreme harness ratios evaluated at 4.5 GV and zenith angle 0^o. For comparison, Ait Ouamer et al. balloon measurements at the same rigidity were superimposed.

To fit the combined neutron measurements of the Kanbach et al. (1974) and Preszler et al. (1976), Morris et al. used the broken power law fit. The combined measurements showed a break at 70 MeV (See figure 5.8). To fix the break at 70 MeV, Morris et al. fitted the COMPTEL neutron data to broken power law fit using the power law index fixed at -1.89 for neutron energy above 70 MeV E_n. It is the same index used by Kanbach et al. for a fit to their neutron current measurements. This gave a free parameter for low-energy (0-70 MeV) spectral index. The two fits below cover neutron energy range from En = 0-70 MeV and En $\geq$ 70 MeV:

$$\phi(P_c, \theta, R_{nm}, E_n) = 8.7M(R_{nm})(1 - b\theta)e^{-\alpha P_c}E_n^{-1.89}cm^{-2}s^{-1}MeV^{-1}E_n > 70MeV \quad (5.4)$$

$$\phi(P_c, \theta, R_{nm}, E_n) = 0.0.36M(R_{nm})(1 - b\theta)e^{-\alpha P_c}E_n^{-0.6}cm^{-2}s^{-1}MeV^{-1}E_n <= 70MeV \quad (5.5)$$

The above expressions, evaluated for cutoff rigidity 4.5 GV, zenith angle 0^o, and solar modulation as a fuction of neutron monitor rate M(Rnm) = 1. Note the upward fluxes were derived from two balloon measurements at the same rigidity. The figure 5.8 shows broken

power law fit to the combined Kanbach et al. and Preszler et al. neutron measurements.

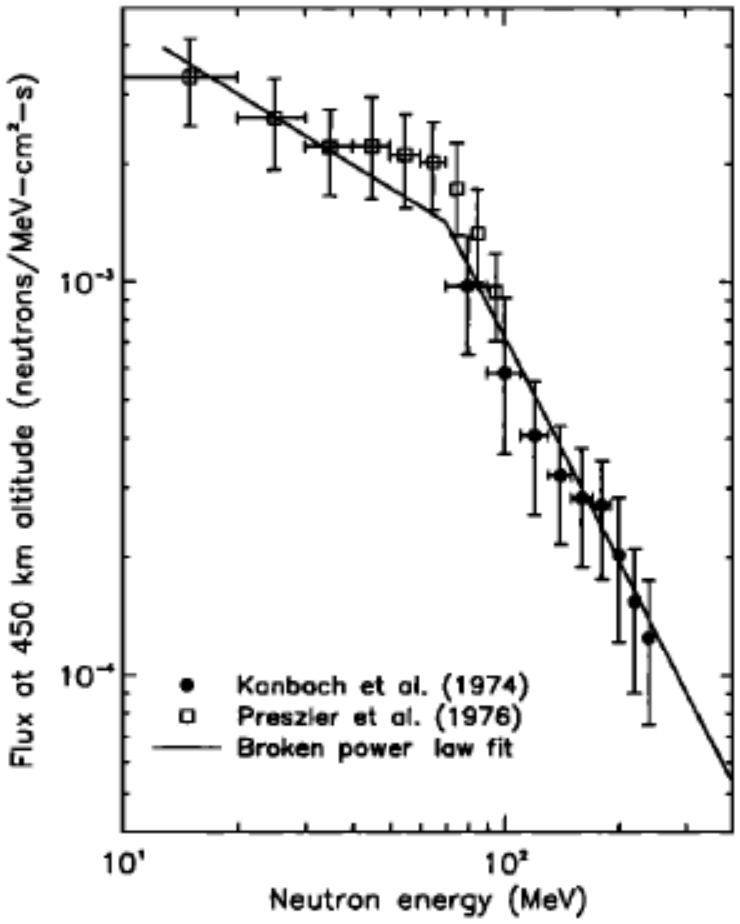

Figure 5.8: Morris et al. used the Broken power law to fit combined neutron measurements of Kanbach et al. at (70-250 MeV) and Preszler et al. (10-100 MeV). The broken power law also fixed the break at 70 MeV, fitting the low energy neutron measurements.

The comparison of the COMPTEL measurements with balloon measurements showed that the source of fast neutron flux in orbit is primarily atmospheric albedo neutrons. In another research article, Morris et al. (1998) used four COMPTEL neutron measurements (twice in 1991, twice in 1994) and Mt. Washington rate. He adjusted the coefficients in broken power fit law and re-drove the fit for two energy ranges E$\leq$ 70 MeV and E$\geq$ 70 MeV.

$E_n \leq$ 70 MeV

$$\phi(P, R_{MtW}) = 0.0308 * \frac{R_{RMtW}}{2000} * \int_0^{140} (1 - b * \theta) d\theta * e^{(-(\alpha + \beta \frac{R_{MtW}}{2000}) * P)} * \int_0^{70} E_n^{-0.56} dE_n \quad (5.6)$$

$E_n \geq$ 70 MeV

$$\phi(P, R_{MtW}) = 22.8 * \frac{R_{RMtW}}{2000} * \int_0^{140} (1 - b * \theta) d\theta * e^{(-(\alpha + \beta \frac{R_{MtW}}{2000}) * P)} * \int_{70}^{110} E_n^{-2.13} dE_n \quad (5.7)$$

where $\alpha = 0.1182$, $\beta = 2.54$ * 10^-3, and P = magnetic rigidity.

Using equations (5.6) and (5.7), we evaluated neutron flux for two energy intervals and plotted it as a function of 2.2 MeV count rates (See figure 5.9).There is a linear relationship between the neutron flux and 2.2 MeV count rates. Also, at higher neutron energy (En $\geq$ 70 MeV) we obtained lower neutron flux and at lower neutron energy (En $\leq$ 70 MeV) we obtained higher neutron flux. Since most of the thermalized neutron measurements were below 70 MeV, we used equation (5.6) to calibrate our 2.2 MeV rates for each altitude ranges.

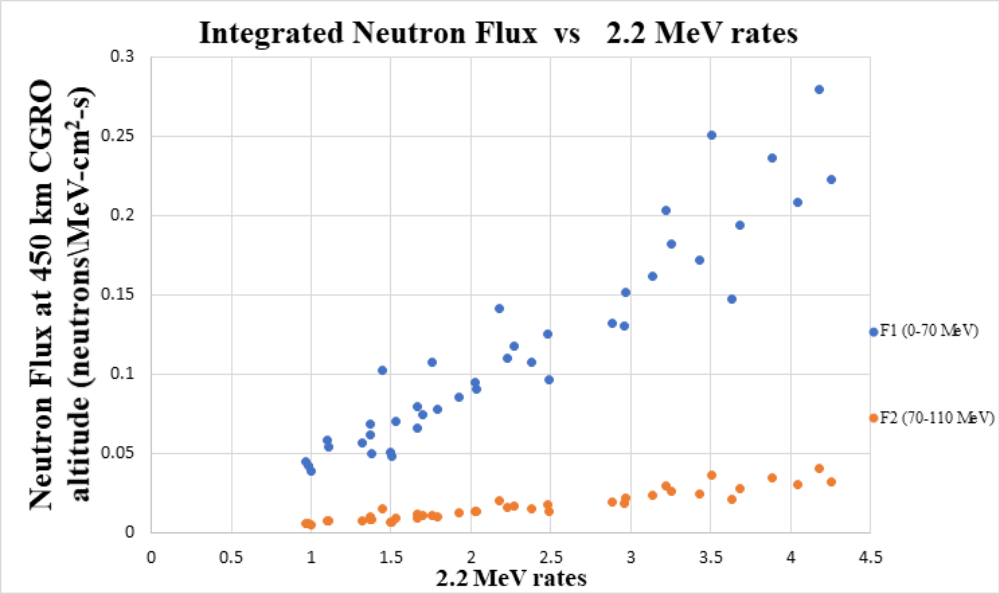

Figure 5.9: The neutron flux evaluated at two energy ranges (0-70 MeV) and (70-110 MeV). Both neutron fluxes are plotted as a function of 2.2 MeV rates.

Using the figure 5.9, we calibrated our neutron rate measurements for all three altitude ranges to obtain the estimated neutron flux. The plots below show estimated neutron flux for each altitude range.

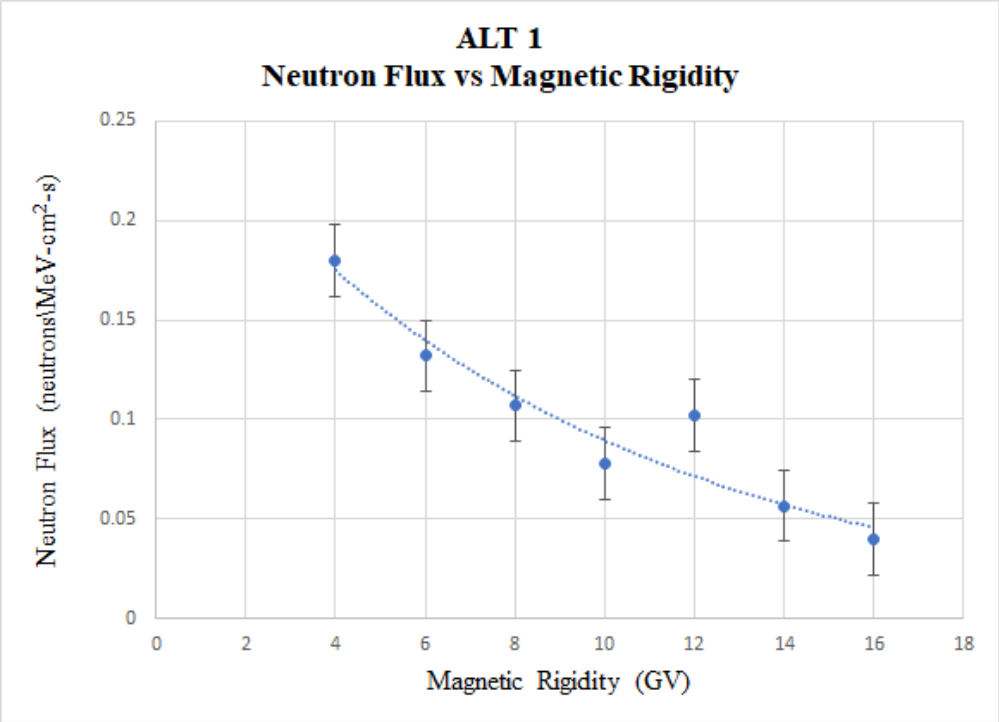

Figure 5.10: The estimated neutron flux as a function of rigidity for altitude range 1

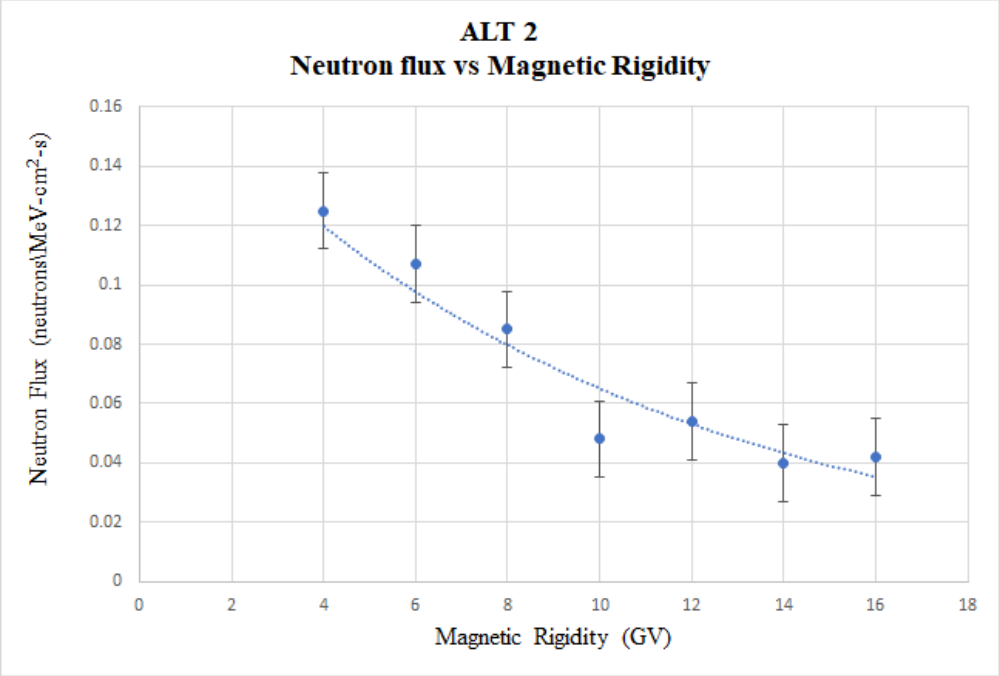

Figure 5.11: Neutron flux as a function of rigidity. The exponential curve fit best describes the data.

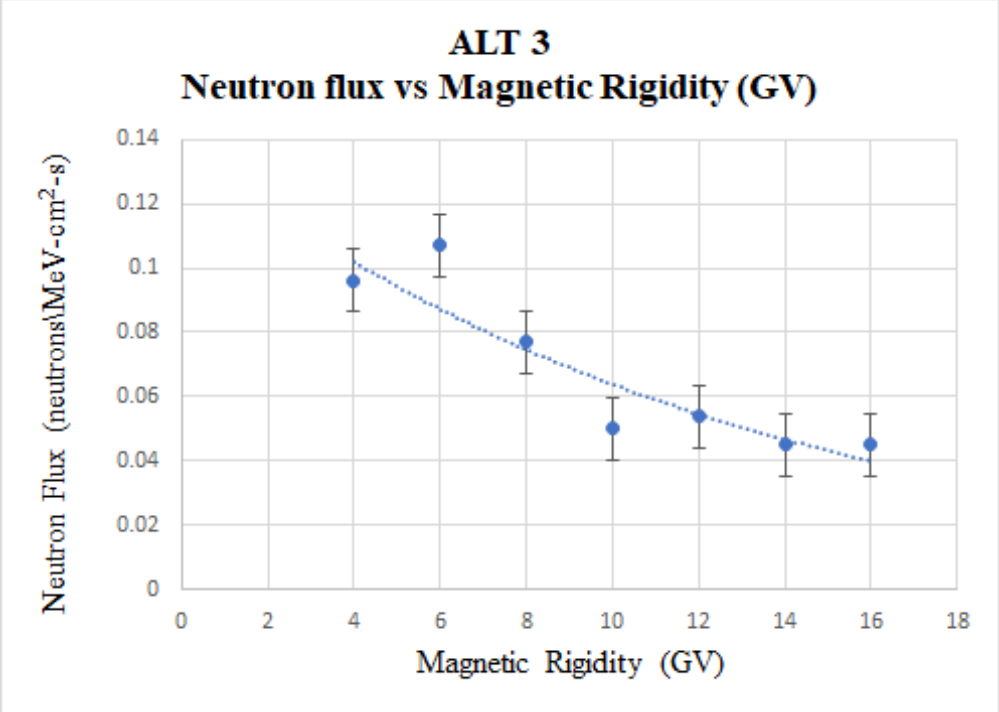

Figure 5.12: The exponential curve fit best describes the data. This trend is also true for 2.2 MeV rates as a function of rigidity.

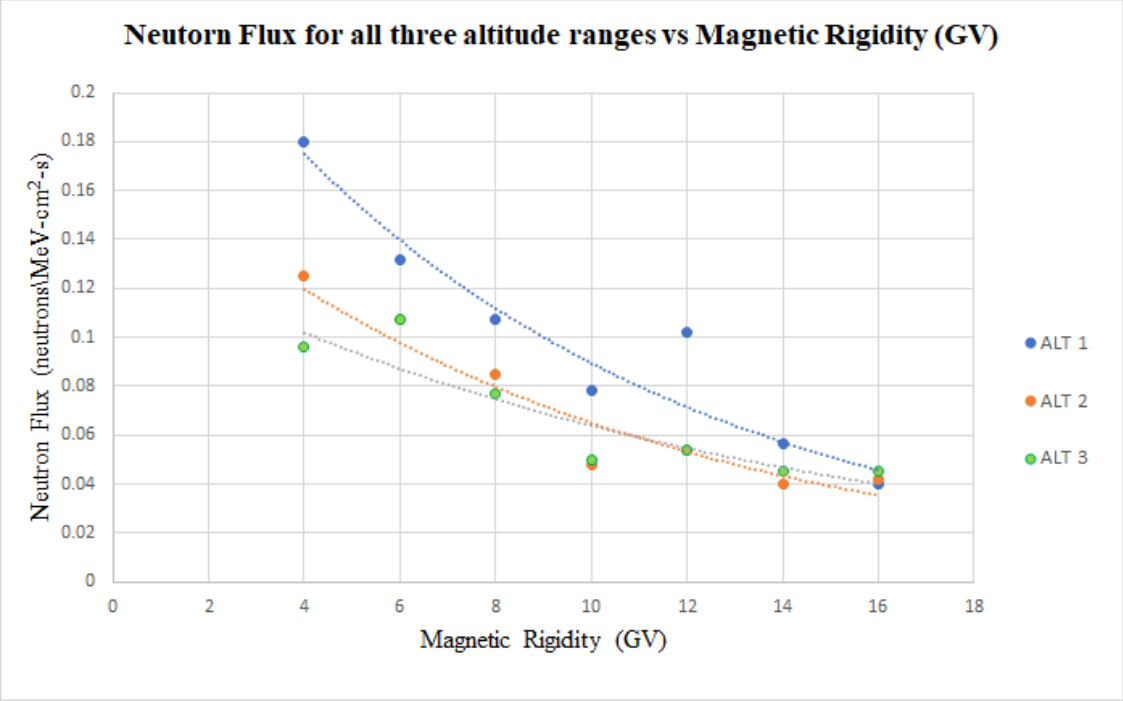

Figure 5.13: The estimated neutron flux for all three altitude ranges as a function of rigidity. To fit the data, exponential curve fits are plotted for each altitude range.

From the above plots we can infer that both estimated neutron flux and 2.2 MeV rate exponentially decreases at higher rigidity values. This exponential trend also confirms the previous studies and models done by Weidenspointner. In the later section (Section VI), we compared our neutron measurements with Claret et al. neutron model. On a logarithmic scale, we expect to see a linear relationship between neutron flux and rigidity.

CHAPTER 6

Conclusion

The focus of this chapter is to compare our measured neutron flux results with the Claret et al. simulated results. We will specifically discuss the neutron flux as a function of temporal variation and other parameters like magnetic rigidity and altitude. Later we will discuss the overall measured neutron flux results and future work.

6.1 Comparing Claret simulated data and estimated neutron flux

To better understand the impact of solar modulation on the neutron flux, we used Claret et al. simulated albedo neutron data. The simulated data integrates two neutron measurements (COMPTEL 1991) at magnetic rigidity 4.5 GV and 8.5 GV to derive the albedo neutron flux at wider energy range (20-100MeV) and magnetic rigidity values (0-17 GV) at altitude 450 km. Furthermore, Claret et al. separated the simulated data with respect to solar min and solar max. Figure 6.1 shows the Claret simulation, along with two neutron measurements from the COMPTEL 1991. In addition, we superimposed measured neutron flux data from altitude range (ALT 2). Since the Claret model simulated the neutron flux at 450 km altitude, we specifically chose the ALT 2 data to cover the simulation altitude.

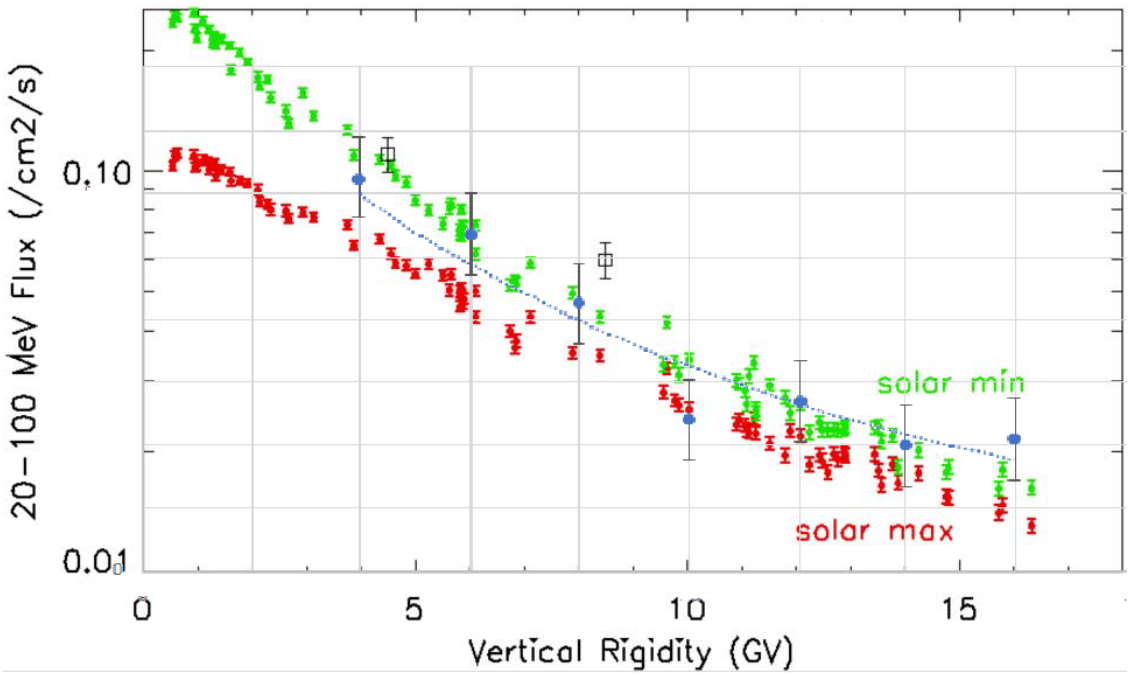

Figure 6.1: : Claret simulation data of neutron flux (E: 20-100 MeV) at solar min (green) and solar max (red) as a function of rigidity. The COMPTEL estimated neutron flux data for altitude range 2 (ALT 2) (blue) is superimposed on the figure for comparison.

From figure 6.1 one can infer that the measured neutron flux data follows the same trend as the simulated data. The ALT 2 is composed of several phases (phase IV-VI), which covers a transition period from solar maximum to solar minimum. Thus, we expect to see a higher neutron flux relative to Claret model at solar maximum. Also, COMPTEL measured secondary neutrons from cosmic rays and other astrophysical events like Crab nebula, XRB (X-Ray Binaries) that could also increase the total neutron flux. Although COMPTEL provided limited neutron flux measurements, the Claret model still represents an adequate description of the estimated neutron flux at an altitude of 450 km. This confirms our initial assumptions about the neutron data and previous studies by Morris et al.

6.2 Future Work

The 2.2 MeV line emission rate played an essential role to study the albedo neutron flux at various observational and event parameters, however additional work can be done on this

project to maximize the neutron flux study. For example, using COMPTEL neutron mode data, to measure neutron spectrum directly. Ideally, the spectral shape of neutrons should correspond to Morris data and that it doesn't change in time.

LIST OF REFERENCES

[1] Aarts H. Bennett K. Lockwood J.A. McConnell M.L. Ryan J.M Schonfelder V. Steinle H. Weidenspointner G. Morris, D.J. Comptel measurements of the omnidirectional high-energy neutron flux in near-earth orbit. *Advances in Space Research*, 21(12):1789–1792, 1998.

[2] Brugger M. Combier N. Ferrari A. Laurent P. Claret, A. Support for crand theory from measurements of earth albedo neutrons between 70 and 250 mev. *IEEE Transactions on Nuclear Science,*, 61(6):3363–3370, 2014.

[3]

[4] Friesen L. Lin A. Mabry D. Katz N. Dotan Y. George J. Blake J. B. Looper M. Redding M. O'Brien T. P. Cha J. Birkitt A. Carranza P. Lalic M. Fuentes F. Galvan R. McNab M. Mazur, J. The relativistic proton spectrometer (rps) for the radiation belt storm probes mission. *Space Science Reviews*, 179(1-4):221–261, 2012.

[5] Jaynes.A.N Li.X Kanekal.S.G Hudson.M.K Kress.B.T Selesnick R.S, Baker.D.N. Observations of the inner radiation belt: Crand and trapped solar protons. *Geophysical Research: Space Physics*, 2000.

[6] Brugger M. Combier N. Ferrari A. Laurent P. Claret, A. Fluka calculation of the neutron albedo encountered at low earth orbits. *IEEE Transactions on Nuclear Science,*, 61(6):3363–3370, 2014.

[7] Looper M. D. Selesnick, R. S. A theoretical model of the inner proton radiation belt. *Journal of Geophysical Research: Space Weather*, 5(4), 2007.

[8] K Bennett H deBoer J. Clear W Collmar A Connors A. Deerenberg R Diehl A.von Dordrecht J W. den Herder W Hermsen R M. Kippen L Kuiper G G. Lichti J Lockwood John R.Macri Mark L. McConnell D Morris R Much James M. Ryan G. Simpson M. Snelling G Stacy H Steinle A W. Strong B Swanenburg B G. Taylor C de Vries V. Schonfelder, H. Aarts and C Winkler. Instrument description and performance of the imaging gamma-ray telescope comptel aboard the compton gamma-ray observatory. *The Astrophysical Journal Supplement Series*, 86(12):657, 1993.

[9] Hudson M. K. Kress B. T. Selesnick, R. S. Direct observation of the crand proton radiation belt source. *Journal of Geophysical Research: Space Physics*, 118(12):7532–7537, 2013.

[10] Varendorff M. Oberlack U. Morris D. Plüschke S. Diehl R. Kappadath S. C. McConnell M. Ryan J. Schönfelder V. Steinle H. Weidenspointner, G. The comptel instrumental line background. *Astronomy Astrophysics*, 368(1):347–368, 2001.

[11] Reppin.C Kanbach, G. Support for crand theory from measurements of earth albedo neutrons between 70 and 250 mev. *Journal of Geophysical Research,*, 79(34):5159–5165, 1974.

[12] Moon S. White R. S. Preszler, A. M. Atmospheric neutrons. *Journal of Geophysical Research*, 81(25):4715–4722, 1976.

[13] G.F Knoll. *Radiation Detection and Measurement*. Wiley, 2010.

[14] C.T Russell. The solar wind interaction with the earth's magnetosphere: a tutorial. *IEEE Transactions on Plasma Science*, 28(6):1818–1830, 2000.

[15] Shea M.A. Fluckiger E O. Smart, D.F. Magnetospheric models and trajectory computations. *Journal of Geophysical Research: Space Weather*, 93:305–333, 2000.

[16] Russell C. Kivelson, M. *Introduction to Space Physics*. Cambridge University Press, 1995.

[17] Jan Gieseler. Understanding galactic cosmic ray modulation: Observation and theory. *Department of Mathematics and Natural Science,University of Kiel.*, 2018.

[18] Dirk Petry. The earth's gamma-ray albedo as observed by egret. *AIP Conference Proceedings*, 2005.

[19] Murphy Ronald J. Share, Gerald H. Gamma ray spectroscopy in the pre-hessi era. *High Energy Solar Physics*, 2000.

[20] E. Work Work, T.S. *Laboratory Techniques in Biochemistry and Molecular Biology: Immunochemical techniques for the identification and estimation of macromolecules.*, volume 3. Elsevier, 1970.

[21] M. Fornasa and M. Sanchez-conde. The nature of the diffuse gamma-ray background. *Cosmology and Nongalactic Astrophysics*, 2015.

[22] Andritschke R. Schopper F. Zoglauer, A. Megalib the medium energy gamma-ray astronomy library. *Thesis*, 2005.